Durham E-Theses

Treatment of quark masses in b-associated production at the LHC

NAPOLETANO, DAVIDE

Treatment of quark masses in b-associated production at the LHC

Davide Napoletano

A Thesis presented for the degree of
Doctor of Philosophy

Department of Physics
Institute for Particle Physics Phenomenology
University of Durham
United Kingdom

16th August 2017

Treatment of quark masses in b-associated production at the LHC

Davide Napoletano

Submitted for the degree of Doctor of Philosophy
16th August 2017

Abstract

With the discovery of the Higgs boson at the Large Hadron Collider (LHC), and no signs of new physics to current date, precise theoretical predictions are of increasing importance. It is now essential to study in details the properties of the newly found boson, in particular its coupling to other particles and itself, as this unveils further the mechanism of symmetry breaking.

In this thesis, we extend the currently used methods to deal with heavy quarks in hadron collision processes, the *four-flavour* and the *five-flavour* scheme, to consistently include mass effects as well as resummation of collinear logarithms. This is done using two complementary approaches. At the inclusive level, we extend a method used to include mass effects in parton densities evolution, known as FONLL. At the differential level, we devise a *five-flavour* scheme that includes mass effects consistently and systematically up to MC@NLO accuracy.

We study the impact of such schemes on two phenomenologically relevant processes at the LHC: the production of a heavy boson, a Z or a Higgs, in association with heavy quarks. For these processes, in fact, the two standard schemes, have been known to largely disagree. In both new schemes, mass effects are found to have a few percent effect, with the bulk of the difference between a completely massless and a completely massive picture, residing in the resummation of collinear logarithms.

Declaration

This thesis is based collaborative research and the corresponding publications, preprints, and proceedings contributions are listed below. No part of this thesis has been submitted elsewhere for any other degree or qualification.

Chapter 3 is based on joint research conducted with Prof. Dr. Stefano Forte and Dr. Maria Ubiali. The content of this chapter appears in reference [1], reference [2] and section IV.2.2 of reference [3].

Chapter 4 is based on joint research conducted with Prof. Dr. Frank Krauss and Jun. Prof. Dr. Steffen Schumann. The content of this chapter appears in reference [4], section IV.2.3 of reference [3] and section IV.6 of reference [5].

Chapter 5 is based on joint research conducted with Prof. Dr. Frank Krauss, Dr. Marek Schönherr and Dr. Stefan Höche. The content of this chapter is, as of today, in preparation for publication.

Acknowledgements

I wish to thank my supervisor, Frank Krauss, for his guidance and support, and especially for his help in starting many successful collaborations I have been part of. I am also grateful for the chance he has given me to develop as a researcher, giving me the chance to carry on my own projects and interests, still helping me when in need.

I would also like to thank Stefano Forte and Maria Ubiali, for the work done together.

I am grateful to my colleagues from the SHERPA Collaboration whom have provide invaluable help time and time again. In particular I wish to thank Marek Schönherr, Steffen Schumann and Stefan Höche for their hospitality in Zürich, Göttingen and SLAC, as well as for their help with many problems I have encountered.

A very special thanks goes to the whole of the "HiggsTools" network, and, in particular the ESRs.

Finally I would like to thank Alessia, without whom I would not probably even be here writing this thesis. I am really grateful for everything you have done, and continuously, do.

Contents

List of Figures

List of Tables

Chapter 1

Motivation and outline

In order to study the fundamental laws of nature, particles are smashed together at a speed very marginally lower than that of light with an incredible amount of energy. Nowadays this happens at the Large Hadron Collider, LHC, at CERN, where a record energy of 6.5 TeV per beam particle is given to protons, which are made colliding inside the four detectors ATLAS, CMS, LHCB and ALICE. Thanks to these collider experiments we have discovered the Higgs boson, which was the most important missing piece of the Standard Model of interactions [6, 7], as its properties determine how particles have acquired their mass through electroweak symmetry breaking.

The need for experiments, especially in the process of discovering new particles, is clear, but a fundamental part of information in understanding experimental results comes from theoretical predictions. These theory inputs are, in fact, extensively used in experiments for many reasons. For example they are used to predict how we expect a certain collection of events to look like, and are thus used to extract the *background*, that we now how to model, from what we expect to highlight, or *signal*. As the precision of experimental results increases, thus theoretical predictions' precision and accuracy must be increased accordingly. For many years the main way this has been achieved is through the inclusion of higher-order corrections. The calculation of higher orders alone, however, has not proved to be enough.

The way the proton momentum is distributed amongst its partons, parametrised by parton distribution functions (PDFs), the way particles produced at the hard

scale of the core process then evolve and emit other particles, as well as how they then combine to produce the observable hadrons, all concur to the final precision of the theory prediction. Monte Carlo event generators are tools that allow to predict this whole chain, thus giving results that can be directly compared with experimental measurements. It is clear that each of the previous pieces must come as precise and accurate as possible. For this reason, aspects of calculations that were always considered to be negligible are now becoming increasingly important.

For historical and practical reasons, for example, a parton, that is a particle that is allowed to be found inside a proton and thus participate in a reaction, has always been considered to be massless. This is clearly a good a approximation for those quarks whose mass is so small that we are never able to resolve at hadron colliders, or have a mass so large that they are extremely unlikely to be found inside a proton. The reason behind this idea is that we are only able to define, in a universal way, the partonic content of the proton up to power corrections of the mass of the given quark over the characteristic scale of *Quantum Chromodynamics*, m_Q/Λ_{QCD}. For quarks that have a very small mass, like the *up*, *down* or *strange* quarks, or an extremely large mass, like the *top*, this description is clearly enough.

There is, however, a class of quarks, the *charm* and the *bottom*, whose masses are small enough to be negligible for some of the energy scales at hadron colliders, but still much larger than Λ_{QCD}. As such, the proper inclusion of mass corrections for these quarks can have important effects in regions of phase space, where their suppression is not so large. In this work, we study how to extend the standard massless parton description to include systematically quark masses and retain full mass effects.

In the context of this thesis we focus on *b*-quarks, and in particular, we focus on the associated production of such heavy quarks with a heavy boson (a *Z* or a Higgs boson). These processes are interesting for a variety of reasons, and as such demand a good theoretical control. Firstly, processes like $bg \rightarrow Zb$, which are a subprocesses of the ones considered here, are used to determine the bottom content of the proton. The precise determination of the bottom quark density, in turn, can be used to make precise predictions for processes like Higgs production in bottom

quark fusion. This latter process is then used to precisely determine the bottom Yukawa coupling to the Higgs boson. The reason why the precise determination of this coupling is important is that it can help discriminating between various beyond the Standard Model scenarios. Many of these models, in fact, allow for Higgs boson multiplets and the mixing among these Higgs bosons can modify the coupling to heavy quarks with respect to that the Standard Models.

In addition, from the experimental point of view, the difference between a scheme, in which b-quarks are treated as massive, decoupled particles, and one, in which they are treated on the same footing as the other partons, is often taken as a theory uncertainty inputs. It is thus necessary to understand the origin of this difference in order to be able to provide with reliable simulations of processes involving heavy flavours. This case is of particular relevance for observables like the p_T spectrum of a Z boson in Drell-Yan, where the partonic channel $b\bar{b} \to Z$ play an important role. This process is in fact measured with outstanding precision, and is used as input to measure the W boson mass. It thus require theoretical predictions at the sub-percent accuracy level. At this level of accuracy mass effects must be taken into account, in particular in the low p_T region.

Lastly, contrary to the charm quarks that has a mass close to that of the proton, and is in general safe to consider massless, the mass of the bottom quark lies within the region of interest at hadron colliders. Its inclusion is thus thought to yield larger effects than that of the charm quark in general, and in particular in the case of Higgs boson production, where the Yukawa coupling is proportional to the mass of the interacting particles. Furthermore, events with identified b-jets and a significant missing transverse momentum constitute a possible signature of Dark Matter production. For this signal invisibly decaying Z-bosons associated with b-jets pose a severe irreducible background.

The outline of this work is the following. We start by reviewing some fundamental methods by which it is possible to obtain theoretical predictions. This serves to introduce the notation we use throughout. As this project is carried out in the context of the SHERPA Monte Carlo collaboration, we focus only on those methods that are implemented there, when discussing event generation, unless otherwise

stated.

We discuss how the two schemes generally used to obtain prediction for processes involving bottom quarks, the *four* and the *five flavour scheme*, can lead to substantial differences in predictions for the inclusive production of a Higgs boson. We then show how to match these two predictions to obtain a reliable estimate of the importance of mass effects for this process.

Further, we study how these two different approaches describe experimental data for the associated production of a Z boson. We use the conclusions in this case to understand differential predictions for the similar case of the associated production of a Higgs boson.

Lastly we introduce the ingredients that are needed to promote the standard *five flavour scheme* to a scheme in which full mass effects are systematically retained. This requires to extend some of the standard techniques presented in this first chapter to accommodate for the introduction of massive quarks in the initial state. We conclude this part by presenting an explicit example of this scheme in Higgs production in bottom quark fusion.

Chapter 2

Theoretical tools

2.1 Factorisation of QCD cross sections

Every *Quantum Chromodynamics* (QCD) calculation at the LHC is based on a collinear factorisation theorem which states that the low-energy (long-distance) and the high-energy (short-distance or partonic) part of an observable factorise. Additionally, the long-distance part is process independent and encodes how the longitudinal momentum of the proton is shared among its partons and is commonly known as Parton Distribution Function (PDF). However, this factorisation theorem can only be exactly derived in Deeply Inelastic Scattering processes using an Operator Product Expansion. In this expansion, only the leading term is really believed to be universal and thus put in the definition of PDF, while power-suppressed (higher-twist) terms are neglected [8, 9].

Although a formal theorem/proof does not exist for general LHC processes, it is widely believed that a factorisation theorem holds for the most important production modes, in non-pathological observables, with higher-twist contributions being suppressed by powers of Λ_{QCD}/Q, where Q is some energy scale in the hard process, while Λ_{QCD} represents the energy at which the $\alpha_s(\Lambda_{QCD}) \sim 1$, $\Lambda_{QCD} \sim 0.3$ GeV.

Including such power suppressed contributions would require to calculate higher-twist corrections to the parton densities, which, as we said, are non-universal. For this reason the common practice is to consider massless, or *active*, all the quarks for which corrections of the type m_q/Λ_{QCD} are small, while all massive quarks, for

which m_q/Λ_{QCD} is not small are treated as *decoupled* from QCD evolution.

This picture, however, is extremely simplistic for two reasons. First, it really only works if there is only one scale in the process. As soon as another energy scale, t, appears, ratios of m_Q/t follow and the hierarchy is no longer straightforward. Second, when we perform a factorisation we need to define what is regarded as high- or low-energy. We thus need to introduce an energy reference scale for factorisation, commonly called *factorisation scale*, or μ_F. In practice, PDFs and partonic cross-sections are a function of this scale. As this scales runs, collinear logarithms like $\log \mu_F/m_Q$ appear and might dominate over power-suppressed terms.

In formulae, the factorised differential cross section can be written as

$$d\sigma(Q^2) = \sum_{a,b\in(q,g)} \int_0^1 dx_1 \int_0^1 dx_2\, f_a(x_1,\mu_F^2)\, f_b(x_2,\mu_F^2) d\hat{\sigma}_{ab}\left(x_1, x_2, \frac{\mu_F^2}{Q^2}\right)$$

$$+ \mathcal{O}\left(\frac{\Lambda_{QCD}^2}{Q^2}\right). \quad (2.1)$$

Here and in the following, unless differently stated, hatted letters represent the partonic version of that object, such that $d\hat{\sigma}_{ab}$ stands for the partonic differential cross section for incoming partons (a,b). At *leading order*, for example,

$$d\hat{\sigma} = d\Phi_N(p_1,\ldots,p_N)\mathcal{B}(p_a,p_b;p_1,\ldots,p_N)$$

$$= \frac{1}{\phi(p_a,p_b)}|\mathcal{M}(p_a,p_b;p_1,\ldots,p_N)|^2\,(2\,\pi)^4\delta^{(4)}(p_a+p_b-\sum_{i=1}^N p_i)\prod_{i=1}^N \frac{d^3p_i}{(2\,\pi)^3 2\,E_i}, \quad (2.2)$$

where we denote by $\mathcal{B}$ the born matrix element squared, and ϕ, the initial state flux, is usually included in the definition of $d\Phi_N$ unless otherwise explicitated.

We indicate with $f_a(x_1,\mu_F^2)$ the PDF for parton a with momentum fraction x_1 at the *factorisation scale* μ_F. These functions are subject to the DGLAP equations [10–12]:

$$\frac{df_a(x,\mu_F^2)}{d\log\mu_F} = \frac{\alpha_s(\mu_F^2)}{2\,\pi} \sum_{b\in(q,g)} \int_x^1 \frac{dz}{z}\, P_{ab}(z)\, f_b\left(\frac{x}{z},\mu_F^2\right) + \mathcal{O}(\alpha_s^2) \quad (2.3)$$

The functions $P_{ab}(z)$ are the Altarelli-Parisi splitting function and they are reported in Appendix A for reference. Further the partonic cross section can be written as an expansion in α_s, with μ_R being the *renormalisation scale*

$$d\hat{\sigma}_{ab}\left(x_1, x_2, \frac{\mu_F^2}{Q^2}\right) = \sum_k \alpha_s^k(\mu_R)\, d\hat{\sigma}_{ab}^{(k)}\left(x_1, x_2, \frac{\mu_F^2}{Q^2}, \frac{\mu_R^2}{Q^2}\right), \quad (2.4)$$

with

$$\frac{\mathrm{d}\alpha_s(\mu_R^2)}{\mathrm{d}\log\mu_R} = -b_0\alpha_s^2 - b_1\alpha_s^3 + \mathcal{O}(\alpha_s^4) \tag{2.5}$$

and

$$b_0 = \frac{11\,C_A - 4\,n_f\,T_R}{12\,\pi}\;;\quad b_1 = \frac{34\,C_A^2 - 20\,n_f\,T_R\,C_A - 12\,n_f\,T_R\,C_f}{48\,\pi^2}\;. \tag{2.6}$$

Equations of the form of Eq. (2.3) and Eq. (2.5) are generically referred to as *evolution equations*. In particular Eq. (2.3) describes how parton distribution functions evolve with energy. The idea is that a parton a has a given differential probability to split into a parton b, which is proportional to the Altarelli-Parisi splitting function P_{ab}. As these splittings happen, the distributions of both parton a and b inside the proton, change consequently.

Note that the introduction of scales like $\mu_{R,F}$ is an artifact of the theory, and, as such, physical observables are independent of those scales. Although theoretical predictions are instead dependent on those scales at any given order, Eq. (2.3) and Eq. (2.5) make sure that the structure of any additional order cancel the dependence on those scales at each order. Thus, higher-order predictions depend less on the additional scales $\mu_{R,F}$, the variation of which is commonly used as an estimate of missing higher order contributions.

It is important to notice at this point that both the running of the coupling constant, and the evolution of the parton densities, as they depend on b_0, depend on how many flavour are active (= massless) at the a given energy scale flavour through n_f. There are, traditionally, two approaches in deciding how many flavours are active. One approach, consists in taking Λ_{QCD} as a reference scale. In this way, every quark that has a mass greater than Λ_{QCD}, is considered a massive, or heavy, quark, while every other parton is considered massless and, as a consequence, contributes to n_f. This approach is generally called Fixed Flavour Number Scheme (FFNS). In this case, in fact, n_f remains a fixed number at all energy scales. In the FFNS, heavy quarks do not contribute to either the running of the coupling constant or the evolution of PDFs. In this way, heavy quarks can never appear as initial state particles in the calculation of hard scattering matrix elements, but they can only be produced in them. Thus the partonic cross section can retain the exact

mass dependence.

In an opposed approach, one could argue that some other scales, like μ_R or μ_F, is taken as the reference scale, as in practice one gets logarithms of $\mu_{R,F}/m_Q$ and not of Λ_{QCD}/m_Q, when solving Eqs. (2.3,2.5). Then the heavy quark will start contributing to both the running of the coupling constant and the evolution of PDFs, only when $\mu_{R,F} \gtrsim m_Q$. This is called a Variable Flavour Number Scheme (VFNS) [1]. In a VFNS, the mass of the heavy quark mass parametrise whether the particle is a heavy quark or an active parton, thus acting like a threshold. Threshold effects that appear through terms like $\log \mu_{R,F}/m_Q$ are resummed to all orders by Eqs. (2.3,2.5), and all mass effects are consistently neglected in the calculation of hard matrix elements.

2.2 Monte Carlo methods in brief

The goal of phenomenology studies, like this one, is to ultimately compare against experimental data. There are a very limited set of cases in which this can be done by means of analytical calculations alone. The problem is that experiments have to deal many more particles and many more phase space constraints than we can handle with a simple enough description. To this end, Monte Carlo event generators, like PYTHIA, HERWIG, or SHERPA, play an important role in providing a theory prediction that is the closest possible to what experiments measure.

To get a general idea of how such programs work, imagine an experiment has measured some physical observable, O. In general, we can identify an observable as a function of all final state particles, f, and their momenta $\{p_i\}_{i \leq n_f}$,

$$O \equiv O(f; p_1, \ldots, p_{n_f}). \tag{2.7}$$

Having to deal with quantum mechanical processes, however, means that we cannot determine exactly the final state for any one specific collision. We can, however,

---

[1]There are various ways of defining a VFNS. In particular the choice of threshold and the inclusion of some mass suppressed terms play a role. All different choices, however, are equal up to mass, power-suppressed terms.

predict the differential probability, which in turn is proportional to the differential cross section for producing a specific final state configuration,

$$d\mathcal{P}(f; p_1, \ldots, p_{n_f}) \propto \frac{d\sigma(f; p_1, \ldots, p_{n_f})}{d^3 p_1 \ldots d^3 p_{n_f}}. \tag{2.8}$$

Repeating the experiment over many times gives us access to the expectation value of O,

$$\langle O \rangle = \mathcal{L} \sum_f \int \frac{d\sigma(f; p_1, \ldots, p_{n_f})}{d^3 p_1 \ldots d^3 p_{n_f}} O(f; p_1, \ldots, p_{n_f}) \, d^3 p_1 \ldots d^3 p_{n_f}. \tag{2.9}$$

The quantity $\mathcal{L}$ is called *integrated luminosity*, and is a measure of the number of particles expected to collide over the time of the experiment.

There are two main complications. Firstly, the larger the number of final state particles, the more complicated the integrals. To deal with this issue the Monte Carlo integration method is used. The idea is to generate a very large number, N, of randomly distributed copies of the final state momenta, we label each copy with superscript j. Calling the total volume of integration V, we have that

$$\langle O \rangle = \lim_{N \to \infty} \mathcal{L} \frac{V}{N} \sum_{j=0}^{N} \sum_f \frac{d\sigma(f; p_1^j, \ldots, p_{n_f}^j)}{d^3 p_1^j \ldots d^3 p_{n_f}^j} O(f; p_1^j, \ldots, p_{n_f}^j), \tag{2.10}$$

which follows from the fundamental theorem of calculus and the central value theorem. The main advantage of such an approach is that we can compute the differential cross section for a given configuration and treat that as a weight, w_f^j. We can then just store these weights and attach them to any observable we wish to compute. In contrast, an analytical calculation would only be valid for the specific observable we performed the calculation for.

The second problem comes from the theoretical prediction of $d\sigma$. To make meaningful comparison to experimental data, we need to predict the differential probability with the highest possible accuracy. The main way to achieve such accuracy is to calculate higher orders in the series expansion in Eq. (2.4), in what is called a *fixed order expansion*.

2.3   Fixed order expansion

In a fixed-order expansion, one keeps all matrix elements that contribute to a specific order in the expansion. As the parameter of the expansion is a coupling constant, α_s in the case of QCD, we can view calculating an extra order in the expansion parameter as adding an extra vertex, and thus an extra particle, in all allowed ways. In practice, we can classify such particle only in two ways. We can either resolve this particle, which case is called a real correction, or $\mathcal{R}$, or this particle is virtual and thus is not resolved, which case is called a virtual correction, or $\mathcal{V}$.

In principle this idea can be iterated as many times as one wishes, giving rise to a factorial growth of matrix elements to be considered at each extra order. In practice there is a complication arising when one adds one extra particle. When considering higher order corrections to Eq. (2.2), as we said, we can either have the extra particle being unresolved, in which case the phase space integral is the same as the born cross section, and the integral over internal momenta is carried over in the calculation of the matrix elements, or the extra particle is resolved, thus the phase over which the integration is performed is different.

Each of these two integrals can give singular contributions in the case in which the extra particle, resolved or not, becomes either soft, or collinear to one of the other particle in process. These divergences get canceled when every contribution is added up together [13, 14]. The problem is that these contributions live in different phase-spaces, and Monte Carlo integrators can only deal with one phase-space at a time. We need then to subtract divergences at the integrand level to have finite integral, these methods are generally called *subtraction methods*.

Subtraction methods are now completely automated in Monte Carlo generators for *next-to-leading order* calculations, that is calculations that only involve one extra particle in the final state with respect to the leading order. Efforts are being made to promote such methods for *next-to-next-to-leading order* corrections, although so far this has only been possible for selected processes and in no automatised way. The most widely used of such methods are the Catani-Seymour dipole formalism [15, 16] and the Frixione-Kunszt-Signer subtraction [17]. In the context of this study we focus on the former method. This algorithm was first developed for massless-

particles (including QCD partons) [15], extended to massive fermions [18] in QED, and to massive final state QCD partons [16].

These methods make use of two important properties of QCD radiation. First, the divergent structure of QCD amplitudes factorises, in both the soft and the collinear limit, in a well-know universal structure. Second, the $N+1$ particles phase space factorises into a N and 1 particle phase space, when one of the particles becomes soft, or collinear to any other particle in the event [19, 20]. We can thus make use of these facts to construct subtraction terms that mimic the infrared and collinear behaviour of next-to-leading order QCD amplitudes to render next-to-leading order observables not only finite at an integral level, but also at an integrand level. In this way integration over the full phase-space by means of any Monte Carlo method can be performed. We briefly report in the following section, the main ingredients needed to construct Catani-Seymour subtraction.

2.3.1 Catani-Seymour subtraction in brief

Consider some hard scattering process involving N particles in the final state at its leading order. The NLO cross section is given by

$$\sigma_N^{\mathrm{NLO}} = \int \mathrm{d}\Phi_N \left[\mathcal{B} + \mathcal{V} \right] + \int \mathrm{d}\Phi_{N+1} \mathcal{R}, \qquad (2.11)$$

where $\mathcal{B}$ corresponds to the born contribution, $\mathcal{V}$ is the one-loop, or virtual contribution, and $\mathcal{R}$ is the real emission contribution term.

As denoted by the $N + 1$, in the real emission process, one additional particle is emitted. As this particle can get infinitively soft or collinear to any of the other N final state particles, or the beam direction, $\mathcal{R}$ becomes divergent. The main idea behind the Catani-Seymour method is to make use of universal properties of QCD amplitudes in these limits, to construct subtraction terms $\mathcal{S}$. To better define, we want to perform the integral of $|\mathcal{M}_{N+1}|^2 \equiv \mathcal{R}(\Phi_{N+1})$ over the $N + 1$ particle phase space, Φ_{N+1}, which is both soft and collinear divergent. We thus need to construct

a set of functions $\mathcal{S}(\Phi_N \otimes \Phi_1)$, such that in

$$\int \mathrm{d}\Phi_{N+1} \mathcal{R}(\Phi_{N+1}) = \int \mathrm{d}\Phi_{N+1} \left[\mathcal{R}(\Phi_{N+1}) - \mathcal{S}(\Phi_N \otimes \Phi_1) \right]$$
$$+ \int \mathrm{d}\Phi_N \otimes \int \mathrm{d}\Phi_1 \mathcal{S}(\Phi_N \otimes \Phi_1) \qquad (2.12)$$

the first term of the right hand side is finite. The functions $\mathcal{S}(\Phi_N \otimes \Phi_1)$ depend on the additional property that phase space factorises in the soft and collinear limits.

We require in particular that the subtraction terms $\mathcal{S}(\Phi_N \otimes \Phi_1)$ respect some properties. First, in the limit in which a particle k, of momentum p_k becomes soft, or collinear to a particle i of momentum p_i, if we parametrise the degree of divergence with λ, by having p_k, $p_i \cdot p_k \sim \lambda$ for $\lambda \to 0$, we have to have:

$$\lim_{p_k, p_i \cdot p_k \to 0} \left[\mathcal{R}(\Phi_{N+1}) - \mathcal{S}(\Phi_N \otimes \Phi_1) \right] = \mathcal{O}(\lambda^0). \qquad (2.13)$$

Second, the functions $\mathcal{S}(\Phi_N \otimes \Phi_1)$ are constructed in such a way that their integral over the extra emission phase space can be calculated analytically. Note that these integrals are soft and collinear divergent. However, their divergent part can be computed and extracted and used to subtract $1/\varepsilon^2$ and $1/\varepsilon$ divergences that appear in the one loop contributions to the next to leading order cross section.

If we make use of Eq. (2.12) we then get

$$\sigma_N^{\mathrm{NLO}} = \int \mathrm{d}\Phi_N \left[\mathcal{B} + \mathcal{V} + \int \mathrm{d}\Phi_1 \, \mathcal{S} \right] + \int \mathrm{d}\Phi_{N+1} \left[\mathcal{R} - \mathcal{S} \right], \qquad (2.14)$$

which is now completely free of divergences.

2.3.2 The dipole factorisation formula

The form of the functions $\mathcal{S}$, can be extracted from matrix elements, where divergences appear as poles in the denominator of propagators of intermediate particles. We can thus partial fraction all denominators, which separates all contributions that are divergent only in a specific configuration. When doing this partial fractioning one realises that QCD radiation terms have the form of colour dipoles, $\mathcal{D}$, that can be identified with an emitter particle and a spectator. It turns out that only four configurations are possible:

FF : the particle going soft or collinear is emitted from a final state particle, and the spectator is also in the final state,

FI : the particle going soft or collinear is emitted from a final state particle, and the spectator is in the final state,

IF : the particle going soft or collinear is emitted from an initial state particle, and the spectator is in the final state,

II : the particle going soft or collinear is emitted from an initial state particle, and the spectator is also in the initial state.

As a consequence, we can write the real emission matrix element as a sum of all dipoles, plus terms that are non divergent. The former part equals the function $\mathcal{S}$, such that:

$$\mathcal{S} \equiv \sum_{i=\text{FF,FI,IF,II}} \mathcal{D}_i. \tag{2.15}$$

Further, each dipole contribution is given by the sum of all possible emitter-spectator pair in a given state,

$$\mathcal{D}_{FF} = \sum_{(i,j)\neq k} \mathcal{D}_{ij,k}\,; \quad \mathcal{D}_{FI} = \sum_{(i,j)\neq k} \mathcal{D}_{ij,k} + \mathcal{D}_{ij}^a \tag{2.16}$$

$$\mathcal{D}_{IF} = \sum_{i\neq k} \mathcal{D}_k^{ai}\,; \quad \mathcal{D}_{II} = \mathcal{D}^{ak;b} + \mathcal{D}^{bk;a} \tag{2.17}$$

$$\tag{2.18}$$

In the context of this study we primarily focus on II configurations, so that in practice we only have

$$\mathcal{S} = \mathcal{D}^{ak;b}(p_1, \ldots, p_k, \ldots, p_{N+1}; p_a, p_b) + \mathcal{D}^{bk;a}(p_1, \ldots, p_k, \ldots, p_{N+1}; p_a, p_b)\,. \tag{2.19}$$

The term $\mathcal{D}^{ak;b}$ represents a dipole contribution where the emitter is an initial state particle, a and the spectator is another initial state particle b, and can be further express as

$$\mathcal{D}^{ak;b}(p_1, \ldots, p_k, \ldots, p_{N+1}; p_a, p_b) = -\frac{1}{2\,x_{ab}\,p_a \cdot p_k}\frac{\mathbf{T}_a \cdot \mathbf{T}_b}{\mathbf{T}_a^2}\,\mathbf{V}^{ak,b}(p_a, p_b, p_k)$$
$$\otimes \left|\widetilde{\mathcal{M}}_N\left(\widetilde{p}_1, \ldots, \widetilde{p}_{N+1}; \widetilde{p}_a, p_b\right)\right|^2 \tag{2.20}$$
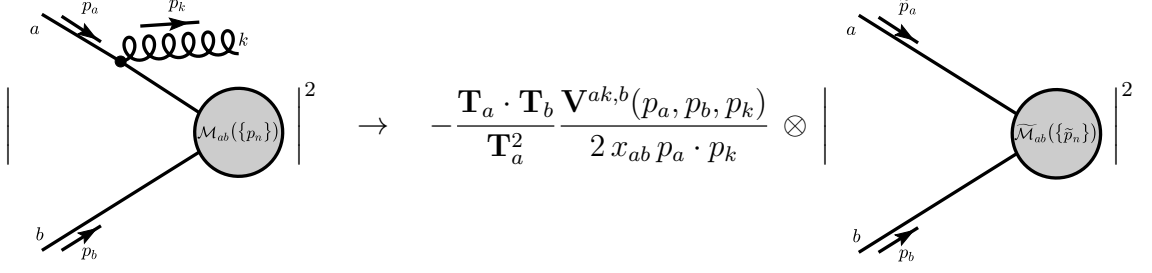
Figure 2.1: Diagrammatic representation of Eq. (2.20) for an initial state emission with an initial state spectator.

where by $\widetilde{p}_i$ we mean a momentum p_i that has been transformed such to re-establish momentum conservation in the projected matrix element. Note also that the symbol $\otimes$ in this context simply hides possible summation in color and helicity space. The functions $\frac{1}{2\,p_i \cdot p_j} \mathbf{V}^{ij,k}(p_i, p_k, p_j)$ are generically called splitting kernels, or dipole splitting functions. The sum of all these functions is referred to as K in the remainder of this work[2].

2.3.3 Dipole terms construction

The construction of the dipole subtraction terms comes from the universal structure of soft and collinear singularities. To see how this work in practice, take for example the matrix element for the production of a Higgs in bottom-quark fusion, with massless b. The matrix element for the emission of an additional gluon can be written as

$$|\overline{\mathcal{M}}_{b\bar{b}\to Hg}|^2 = 8\,\pi\,C_F\,\alpha_s\,\left(\frac{1}{2\,p_a \cdot p_k} + \frac{1}{2\,p_b \cdot p_k}\right) \frac{1+x^2}{1-x}\,|\overline{\mathcal{M}}_{b\bar{b}\to H}|^2\,, \qquad (2.21)$$

if we make the replacement in $|\overline{\mathcal{M}}_{b\bar{b}\to H}|^2$ that

$$s = 2p_a \cdot p_b \to x\,s = 2\,x\,p_a \cdot p_b\,. \qquad (2.22)$$

---

[2]A special case of splitting kernels is given by the Altarelli-Parisi splitting functions, P_{ij}.

This, in turn, can be achieved by the variable transformation

$$\widetilde{p}_a = x\, p_a\,; \quad \widetilde{p}_b = p_b\,. \tag{2.23}$$

Making use of Eq. (2.20) we can easily isolate the splitting function,

$$\mathbf{V}^{ak,b} = 8\,\pi\, C_F\, \alpha_s\, \frac{1+x^2}{1-x}\,, \tag{2.24}$$

and the corresponding dipole term

$$\mathcal{D}^{ak;b} = \frac{1}{2\, p_a \cdot p_k}\, \mathbf{V}^{ak,b}\, |\overline{\mathcal{M}}_{b\bar{b}\to H}|^2\,. \tag{2.25}$$

We can play the same exercise in the case of $e^+e^- \to q\bar{q}$. The next-to-leading order real emission process in this case, can be written as

$$|\overline{\mathcal{M}}_{e^+e^-\to q\bar{q}g}|^2 = 8\,\pi\, C_F\, \alpha_s\, \frac{1}{s}\, \frac{x_1^2 + x_2^2}{(1-x_1)(1-x_2)}\, |\overline{\mathcal{M}}_{e^+e^-\to q\bar{q}}|^2\,, \tag{2.26}$$

with $x_{1,2} = 2\, E_{1,2}/\sqrt{s}$ are the energy fraction of the final state quarks. Performing a partial fractioning on

$$\frac{x_1^2 + x_2^2}{(1-x_1)(1-x_2)} = \frac{1}{1-x_2}\left(\frac{2}{2-x_1-x_2} - (1+x_1)\right) + (x_1 \leftrightarrow x_2)\,, \tag{2.27}$$

we get

$$\mathbf{V}_{ij,k} = 8\,\pi\, C_F\, \alpha_s\, \left(\frac{2}{2-x_i-x_k} - (1+x_i)\right)\,, \tag{2.28}$$

with

$$\mathcal{D}_{ij;k} = \frac{1}{2\, p_i \cdot p_j}\, \mathbf{V}_{ij,k}\, |\overline{\mathcal{M}}_{e^+e^-\to q\bar{q}}|^2\,. \tag{2.29}$$

Note that now we have employed a different phase space mapping

$$\widetilde{p}_k = \frac{1}{x_k}\, p_k\,; \quad \widetilde{p}_{ij} = Q - \widetilde{p}_k\,, \tag{2.30}$$

where Q is the total momentum minus that of the gluon.

The exact form for the dipole functions, as well as for the corresponding phase-space mappings in the general case, are reported in [15]. It is important to notice that, when considering massive quarks [16], mass effects appear, in the construction of the dipole functions, only as power suppressed modifications of $\mathbf{V}_{ij,k}$, as well as of the phase space mappings.

2.4 Parton Shower

Another way of increasing the accuracy of a calculation can be achieved by including part of the leading contributions that appear at each extra order. This can be done using the knowledge of the singular structure of matrix elements, in the same fashion as the PDF factorisation works. Each extra emission, in fact, in the soft or collinear limit factorises off of the born matrix element, in the way described in Eq. (2.20). The m-th emission gives a contribution proportional to

$$\frac{1}{m!}\left(\alpha_s(t)\,\log\frac{t'}{t}\,\mathrm{K}\right)^m,\tag{2.31}$$

with K being splitting kernels. Neglecting color correlations, this series can be summed to all orders in $\alpha_s(t)\log\frac{t'}{t}$. The result of this operation is called *Sudakov form factor* [21–23],

$$\Delta_N(t_0,t)=\exp\left[-\int \mathrm{d}\Phi_1\,\mathrm{K}_N(\Phi_1)\right]\tag{2.32}$$

where $\mathrm{K}_N(\Phi_1)$ represents a generalised splitting kernel that depends on the phase space of the extra emission,

$$\mathrm{d}\Phi_1=\mathrm{d}t\,\mathrm{d}z\,\mathrm{d}\varphi\,\mathcal{J}(t,z,\varphi)\,,\tag{2.33}$$

with $\mathcal{J}$ being the Jacobian transformation coming from the relevant phase-space mappings. The Sudakov form factor, $\Delta_N(t_0,t)$, represents the unconditional differential probability that parton a has not undergone a branching between t_0 and t. Further, the evolution of the Sudakov form factor is, in the same way of PDFs, determined by DGLAP equations.

A reasonable approximation is to identify the splitting kernels with the Altarelli-Parisi splitting function appearing in Eq. (2.3). Another possibility, is to use instead Catani-Seymour dipoles, such that

$$\mathrm{K}_N(\Phi_1)=\frac{\alpha_s}{2\,\pi}\sum_{(i,j)\neq k}\frac{\mathcal{D}_{ij,k}}{\mathcal{B}_N}=\frac{\alpha_s}{2\,\pi}\frac{\mathcal{S}}{\mathcal{B}_N}.\tag{2.34}$$

Particles emitted from the fixed order matrix element with an initial scale μ_Q undergo a backward evolution towards a lower cutoff scale $t_0\sim 1$ GeV. At each stage an extra branching occurs, or not, depending on the relative probability, or weight,

of the Sudakov at that given scale. As the splitting kernels are derived in the soft and collinear limit of matrix elements, this procedure then retains and resum, the leading logarithmic term of each branching.

At the leading order, the showered differential cross section Eq. (2.2) becomes

$$
\begin{aligned}
\mathrm{d}\sigma^{\mathrm{LO}\otimes\mathrm{PS}} &\equiv \mathrm{d}\Phi_N\,\mathcal{B}_N(\Phi_N) \,\otimes\, \Pi^{\mathrm{PS}} \\
&= \mathrm{d}\Phi_N\,\mathcal{B}_N(\Phi_N) \left[\Delta_N(t_0,\mu_Q^2) + \int_{t\in[t_0,\mu_Q^2]} \mathrm{d}\Phi_1\,\mathrm{K}_N(\Phi_1)\,\Delta_N(t(\Phi_1),\mu_Q^2) \right].
\end{aligned} \tag{2.35}
$$

An important feature of the parton shower, that comes from its probabilistic interpretation, is that it is unitary. That means that

$$
\int \mathrm{d}\sigma^{\mathrm{LO}\otimes\mathrm{PS}} = \int \mathrm{d}\sigma^{\mathrm{LO}} \tag{2.36}
$$

2.4.1 Mc@Nlo

Having used Catani-Seymour dipole as splitting kernels, we can extend the picture presented to next-to-leading order matrix elements. For convenience, we define

$$
\int \mathrm{d}\Phi_1\,\mathcal{S}(\Phi_{N+1}) = \mathcal{I}(\Phi_N)\,. \tag{2.37}
$$

The Mc@Nlo matching, is most conveniently expressed in terms of a NLO-weighted Born cross section,

$$
\overline{\mathcal{B}}(\Phi_N) = \mathcal{B}(\Phi_N) + \mathcal{V}(\Phi_N) + \mathcal{I}(\Phi_N) - \int \mathrm{d}\Phi_1\mathcal{S}(\Phi_{N+1})\,\Theta(t-\mu_Q^2)\,, \tag{2.38}
$$

and a hard remainder,

$$
\mathcal{H}(\Phi_{N+1}) = \mathcal{R}_N(\Phi_{N+1}) - \mathcal{S}(\Phi_{N+1})\,\Theta(\mu_Q^2 - t)\,. \tag{2.39}
$$

Note that the ordering variable t is defined differently for each dipole as it depends on the various phase space mappings. Using the same definition of the Sudakov form factor given in Eq. (2.34), we have that

$$
\begin{aligned}
\mathrm{d}\sigma^{\mathrm{Mc@Nlo}} &\equiv \mathrm{d}\Phi_N\,\overline{\mathcal{B}}(\Phi_N) \,\otimes\, \Pi^{\mathrm{PS}} + \mathrm{d}\Phi_{N+1}\,\mathcal{H}(\Phi_{N+1}) \\
&= \mathrm{d}\Phi_N\,\overline{\mathcal{B}}(\Phi_N) \left[\Delta_N(t_0,\mu_Q^2) + \int_{t\in[t_0,\mu_Q^2]} \mathrm{d}\Phi_1\,\mathrm{K}_N(\Phi_1)\,\Delta_N(t(\Phi_1),\mu_Q^2) \right] \\
&\qquad\qquad\qquad\qquad\qquad\qquad\qquad\qquad\qquad + \mathrm{d}\Phi_{N+1}\,\mathcal{H}(\Phi_{N+1})\,. \tag{2.40}
\end{aligned}
$$

As in the leading order case, it can be shown that

$$\int d\sigma^{\text{MC@NLO}} = \int d\sigma^{\text{NLO}}. \tag{2.41}$$

Note that this last relation implies that a MC@NLO observable has the same fixed order accuracy as a NLO one.

2.5 Merging

Parton showers are, broadly speaking, very precise in regions of phase space where soft and collinear radiation dominates. On the other hand, they are not reliable in describing hard radiation, for which the calculation of hard matrix elements is needed. As described in the previous section we can match these two description. In doing so we retain the fixed order accuracy of the matrix element for the first N emission, while any additional emission has the parton shower accuracy.

Merging techniques are used to extend the accuracy of fixed order matrix element to higher multiplicity, $N+1\ldots$, in case any of this emission is hard, and to retain the parton shower picture when these extra emission are soft or collinear. The method we will focus here is the CKKW [24], as implemented in SHERPA [25].

To see how this works, consider one extra emission. We start by defining a parameter, Q_{cut}, that separates between a regime in which a parton is hard, which we call *jet production*, and a regime in which the parton is soft and collinear, called *jet evolution*. In the former we wish to retain the matrix element description, while in the latter we leave the production of the extra parton to the parton shower. In formulae, assigning a scale Q_{N+1} to the extra emission phase space, in the same way as Q_{cut},

$$d\sigma^{\text{MEPS@LO}} \equiv \int d\sigma_N^{\text{LO}\otimes\text{PS}} \oplus \int d\sigma_{N+1}^{\text{LO}\otimes\text{PS}}$$

$$d\Phi_N \, \mathcal{B}_N(\Phi_N) \left[\Delta_N(t_0, \mu_Q^2) + \int_{t\in[t_0,\mu_Q^2]} d\Phi_1 \, \mathrm{K}_N(\Phi_1) \, \Delta_N(t_{N+1}, \mu_Q^2) \, \Theta(Q_{\text{cut}} - Q_{N+1}) \right]$$

$$+ \, d\Phi_{N+1} \, \mathcal{B}_{N+1}(\Phi_{N+1}) \, \Delta_N(t_0, \mu_Q^2) \, \Theta(Q_{N+1} - Q_{\text{cut}}). \tag{2.42}$$

This method can be extended to as high a multiplicity as desired.

2.6 Higher order merging

As well as to higher multiplicity, the method outlined above can be extend to higher accuracy [26]. In particular, using the same techniques, we can merge MC@NLO accurate calculations together, and together with leading order calculation for very high multiplicity where a NLO calculation becomes too expensive. This method is called MEPS@NLO and is developed in [27]. Schematically for one extra emission,

$$
\mathrm{d}\sigma^{\text{MEPS@NLO}} = \mathrm{d}\sigma_N^{\text{MC@NLO}} \oplus \mathrm{d}\sigma_{N+1}^{\text{MC@NLO}}
$$

$$
= \mathrm{d}\Phi_N \, \overline{\mathcal{B}}_N(\Phi_N) \left[\Delta_N(t_0, \mu_Q^2) + \int_{t\in[t_0,\mu_Q^2]} \mathrm{d}\Phi_1 \, \mathrm{K}_N(\Phi_1) \, \Delta_N(t_{N+1}, \mu_Q^2) \, \Theta(Q_{\text{cut}} - Q_{N+1}) \right]
$$

$$
+ \mathrm{d}\Phi_{N+1} \, \mathcal{H}_N(\Phi_{N+1}) \, \Delta_N(t_{N+1}, \mu_Q^2) \, \Theta(Q_{\text{cut}} - Q_{N+1})
$$

$$
+ \mathrm{d}\Phi_{N+1} \, \overline{\mathcal{B}}_{N+1}(\Phi_{N+1}) \left(1 + \frac{\mathcal{B}_{N+1}(\Phi_{N+1})}{\overline{\mathcal{B}}_{N+1}(\Phi_{N+1})} \int_{t\in[t_{N+1},\mu_Q^2]} \mathrm{d}\Phi_1 \, \mathrm{K}_N(\Phi_1) \right) \Theta(Q_{N+1} - Q_{\text{cut}})
$$

$$
\times \left[\Delta_{N+1}(t_0, t_{N+1}) + \int_{t\in[t_0,t_{N+1}]} \mathrm{d}\Phi_1 \, \mathrm{K}_{N+1}(\Phi_1) \, \Delta_{N+1}(t_{N+2}, t_{N+1}) \right]
$$

$$
+ \mathrm{d}\Phi_{N+2} \, \mathcal{H}_{N+1}(\Phi_{N+2}) \, \Delta_N(t_{N+1}, \mu_Q^2) \, \Delta_{N+1}(t_{N+2}, t_{N+1}) \, \Theta(Q_{N+1} - Q_{\text{cut}}) \,. \quad (2.43)
$$

The meaning of this equation can be summarised as follows. For $Q_{\text{cut}} < Q_{N+1}$ Eq. (2.43) reduces to Eq. (5.50). The case of $Q_{\text{cut}} > Q_{N+1}$, on the other hand, is structurally more complicated. The last three lines of Eq. (2.43) have, in fact, two parts. The first one, corresponds to Eq. (5.50) for a $N+1$-particle process. The second one have to account for the second additional radiation either coming from showered $N + 1$ differential cross section or from the hard reminder, without double counting.

Chapter 3

Matching the 4F and the 5F schemes

3.1 Need for a matched calculation

This chapter is devoted on how to obtain predictions in a matched scheme, namely the FONLL [28, 29] scheme. In particular, we focus on the production of a Higgs boson in bottom quark fusion [1, 2].

Higgs production in bottom fusion, like any process involving bottom quarks at the matrix-element level, may be computed using two different factorisation schemes. In the four-flavour scheme, the bottom quark is treated as a massive object, which is not endowed with a parton distribution (PDF). It decouples from QCD perturbative evolution, which is performed only including the four lightest flavours and the gluon in the DGLAP equations, and likewise it decouples from the running of α_s so that $n_f = 4$ in the computation of the QCD β function. In the five-flavour scheme (5FS), instead, the bottom quark is treated on the same footing as other quark flavours, there is a b PDF, and $n_f = 5$ in both the DGLAP and renormalisation-group equations.

As the total inclusive cross section for a Drell-Yan-like process depends only on one hard scale, the virtuality of the produced boson Q, we can predict what the role of mass effects is. For high enough scales, $Q^2 \gg m_b^2$, mass effects become negligible, collinear logarithms related to b-quark radiation are large and must be resummed, and the 5FS is always more accurate. On the other hand, very close to the production threshold, $Q^2 \sim m_b^2$, mass effects are important while collinear logs

are not large, and the 4FS is more accurate. In principle, a computation performed at high enough perturbative order in the 4FS will reproduce the 5FS result, while this is not the case for a 5FS computation, in which b-mass effects are never included.

In practice, however, for Higgs production in bottom fusion the leading-order production diagram, which is $\mathcal{O}(\alpha_s^0)$ (parton model) in the 5FS, is $\mathcal{O}(\alpha_s^2)$ in the 4FS, so one must go to very high order indeed in the 5FS computation in order to reproduce 4FS results. In fact, in the 5FS, the cross section is known up to NNLO [30] and in the 4FS up to NLO [31, 32]. Furthermore, the characteristic scale for this process is necessarily higher than the b production threshold, but perhaps rather lower than the Higgs mass itself [33, 34]. In a wide range the 4FS and 5FS computations at the highest available accuracy disagree by a sizeable amount, with the 5FS result being significantly larger than the 4FS one, though they can be brought to a better agreement with a very low factorisation scale choices, $\mu_F \lesssim m_H/4$. All this suggests that a reliable computation of this process requires the use of a matched scheme which combines the accuracy of the 4FS and 5FS results.

Historically, a matching scheme was devised to interpolate phenomenologically between these the two schemes, the so-called Santander matching [35]. In this scheme, the 4FS and 5FS results are interpolated using a weighted average of the two. The idea is to define the weight as a function of the Higgs boson mass, m_H such that

$$w = \log\left(\frac{m_H}{m_b}\right) - 2\,;\tag{3.1}$$

the combined cross section is then given by

$$\sigma^{\text{Santander-Matched}}(m_H^2) = \frac{\sigma^{(4F)} + w\,\sigma^{(5F)}}{1+w}\,.\tag{3.2}$$

An extensive discussion on how this type of matched prediction compares with theoretically motivated ones, like the one presented in this work can be found in [3]. In the next sections we work out the necessary formulae to construct such a matched scheme, focusing on the bottom quark fusion process.

3.2   The FONLL scheme

The basic idea of the FONLL method is to expand out the 5FS computation, in which logarithms of Q^2/m_b^2 are resummed to all orders, in powers of the strong coupling α_s, and replace them with their massive-scheme counterparts, up to the same order at which the massive-scheme result is known. The combination then retains the logarithmic accuracy of the 5FS result one starts from (with the b quark treated as massless), but now also has the fixed-order accuracy of the massive result, up to the order which has been included. Henceforth, we consistently use the notation $N^k LL$ to refer to the resummed accuracy of the 5FS computation (i.e. by LL we mean a computation in which $\left(\alpha_s \ln \frac{m_b^2}{Q^2}\right)$ is treated as order one), and by $N^k LO$ to the fixed order at which the massive 4FS is performed. These two calculations can thus be matched at any preferred order, in practice however we concentrate on two possible orders. The FONLL-A [1] scheme which is NNLL+LO accurate, and the FONLL-B [2] combination which is NNLL+NLO accurate.

The only technical complication of the FONLL method is that the two computations, which are being combined, are performed in different renormalisation and factorisation schemes. This difficulty is overcome by re-expressing α_s and PDFs in the 4FS computation in terms of their 5FS counterparts, so that one single α_s and set of PDFs is used everywhere. Once this is done, the 4FS and 5FS computations can be simply added, with overlapping terms subtracted in order to avoid double counting: the result has the structure

$$\sigma^{\text{FONLL}} = \sigma^{(4)} + \sigma^{(5)} - \sigma^{(4),(0)}, \tag{3.3}$$

in which $\sigma^{(4)}$ and $\sigma^{(5)}$ are respectively the 4FS and 5FS results, and $\sigma^{(4),(0)}$ is their overlap. The contributions to $\sigma^{(4),(0)}$ can be viewed and obtained either from expansion of the 5FS computation up to finite order or as the massless limit of the massive computation - with the caveat that the 4FS result in the massive limit acquires collinear singularities which in the 5FS are factorized in the PDFs.

We must now work out the necessary ingredients to construct Eq. (3.3). In the following we make extensive use of Eqs. (2.1),(2.3),(2.5). We name objects by adding a $^{(n_f)}$ whenever neccessary to avoid confusion.

3.2.1 The 4F scheme cross section

In order to compute a total cross section in the four flavour scheme we need to use Eq. (2.1) with 4F scheme ingredients. Namely,

$$\sigma^{(4)} = \int_{\tau_H}^{1} \frac{\mathrm{d}x}{x} \int_{\frac{\tau_H}{x}}^{1} \frac{\mathrm{d}y}{y^2} \sum_{ij=q,g} f_i^{(4)}(x, Q^2) f_j^{(4)}\left(\frac{\tau_H}{xy}, Q^2\right) \hat{\sigma}_{ij}\left(y, \alpha_s^{(4)}(Q^2), \frac{Q^2}{m_b^2}\right), \quad (3.4)$$

with

$$\hat{\sigma}_{ij}\left(y, \alpha_s^{(4)}(Q^2), \frac{Q^2}{m_b^2}\right) = \sum_{p=2}^{N} \left(\alpha_s(Q^2)\right)^p \hat{\sigma}_{ij}^{(p)}\left(y, \frac{Q^2}{m_b^2}\right). \quad (3.5)$$

Note that here and in the following discussion on the 4FS, $\hat{\sigma}_{ij}^{(p)}$ refer to the partonic cross sections computed in the 4FS, as highlighted by their explicit dependence on the ratio Q^2/m_b^2.

In practice, we can transform Eq. (3.4) by expressing PDFs and α_s in the 4F scheme to those calculated in the 5F scheme. In this way, we obtain

$$\sigma^{(4)} = \int_{\tau_H}^{1} \frac{\mathrm{d}x}{x} \int_{\frac{\tau_H}{x}}^{1} \frac{\mathrm{d}y}{y^2} \sum_{ij=q,g} f_i^{(5)}(x, Q^2) f_j^{(5)}\left(\frac{\tau_H}{xy}, Q^2\right) B_{ij}\left(y, \alpha_s^{(5)}(Q^2), \frac{Q^2}{m_b^2}\right), \quad (3.6)$$

where $f_i^{(5)}$ and $\alpha_s^{(5)}$ are 5FS PDFs and α_s, and the coefficients

$$B_{ij}\left(y, \alpha_s^{(5)}(Q^2), \frac{Q^2}{m_b^2}\right) = \sum_{p=2}^{N} \left(\alpha_s^{(5)}(Q^2)\right)^p B_{ij}^{(p)}\left(y, \frac{Q^2}{m_b^2}\right) \quad (3.7)$$

are such that if $f_i^{(5)}$ and $\alpha_s^{(5)}$ are re-expressed in terms of $f_i^{(4)}$ and $\alpha_s^{(4)}$, then the expression of $\sigma^{(4)}$ in the 4FS, Eq. (3.4), is recovered.

In order to obtain the coefficients B_{ij}, we thus need to match Eq. (3.6) onto Eq. (3.4) at the order in α_s we wish to perform the matching at. The coupling constant and the PDFs are related in the two schemes by equations of the form

$$\alpha_s^{(5)}(Q^2) = \alpha_s^{(4)}(Q^2) + \sum_{i=2}^{\infty} c_i \left(\log \frac{Q^2}{m_b^2}\right) \times \left(\alpha_s^{(4)}(m_b^2)\right)^i, \quad (3.8)$$

$$f_i^{(5)}(x, Q^2) = \int_x^1 \frac{\mathrm{d}y}{y} \sum_j K_{ij}\left(y, \log \frac{Q^2}{m_b^2}, \alpha_s^{(4)}(Q^2)\right) f_j^{(4)}\left(\frac{x}{y}, Q^2\right), \quad (3.9)$$

where the sum runs over the eight lightest flavours, antiflavours, and the gluon, while the index i takes value over all ten quarks and antiquarks and the gluon. The coefficients $c_i(L)$ are polynomials in $L \equiv \log \frac{Q^2}{m_b^2}$, and the functions K_{ij} can be

expressed as an expansion in powers of α_s, with coefficients that are polynomials in L.

The first nine equations, Eq. (3.9), relate the eight lightest quarks and the gluon in the two schemes and can be inverted to express the four-flavour-scheme PDFs in terms of the five-flavour-scheme ones. The last two equations, assuming that the bottom quark is generated by radiation from the gluon (i.e. no *intrinsic* [36] bottom component) express the bottom and anti-bottom PDFs in terms of the other ones. In particular, this assumption implies that the b quark and antiquark PDFs are equal to each other, $f_b^{(5)} = f_{\bar{b}}^{(5)} + \mathcal{O}(\alpha_s^2)$. Inverting Eqs. (3.8-3.9) and substituting in Eq. (3.4) one can obtain an expression of $\sigma^{(4)}$ in terms of B_{ij} and 5FS objects.

The solution of Eq. (3.8) are explicitly reported in Appendix B up to order α_s^2. Making use of Eqs. (3.8),(3.9) expression we get the non-vanishing $B_{ij}^{(k)}$ coefficients at $\mathcal{O}(\alpha_s^2)$

$$B_{gg}^{(2)}\left(y, \frac{Q^2}{m_b^2}\right) = \hat{\sigma}_{gg}^{(2)}\left(y, \frac{Q^2}{m_b^2}\right),$$
(3.10)

$$B_{q\bar{q}}^{(2)}\left(y, \frac{Q^2}{m_b^2}\right) = \hat{\sigma}_{q\bar{q}}^{(2)}\left(y, \frac{Q^2}{m_b^2}\right);$$
(3.11)

while at $\mathcal{O}(\alpha_s^3)$ we get:

$$B_{gg}^{(3)}\left(y, \frac{Q^2}{m_b^2}, \frac{\mu_R^2}{m_b^2}, \frac{\mu_F^2}{m_b^2}\right) = \hat{\sigma}_{gg}^{(3)}\left(y, \frac{Q^2}{m_b^2}\right) - \frac{2T_R}{3\pi}\ln\frac{\mu_R^2}{\mu_F^2}\hat{\sigma}_{gg}^{(2)}\left(y, \frac{Q^2}{m_b^2}\right),$$
(3.12)

$$B_{q\bar{q}}^{(3)}\left(y, \frac{Q^2}{m_b^2}, \frac{\mu_R^2}{m_b^2}, \frac{\mu_F^2}{m_b^2}\right) = \hat{\sigma}_{q\bar{q}}^{(3)}\left(y, \frac{Q^2}{m_b^2}\right) - \frac{2T_R}{3\pi}\ln\frac{\mu_R^2}{m_b^2}\hat{\sigma}_{q\bar{q}}^{(2)}\left(y, \frac{Q^2}{m_b^2}\right),$$
(3.13)

$$B_{gq}^{(3)}\left(y, \frac{Q^2}{m_b^2}\right) = \hat{\sigma}_{gq}^{(3)}\left(y, \frac{Q^2}{m_b^2}\right),$$
(3.14)

$$B_{qg}^{(3)}\left(y, \frac{Q^2}{m_b^2}\right) = \hat{\sigma}_{qg}^{(3)}\left(y, \frac{Q^2}{m_b^2}\right).$$
(3.15)

Note that we suppress the obvious $\mu_{R,F}$ dependence in $\hat{\sigma}_{ij}^{(p)}$.

3.2.2 The massless limit of the massive cross section

As we said, the overlap term corresponds to the massless limit of the massive cross section. This contribution is equivalent to a 4FS calculation where all logarithms and constant terms retained, and all terms suppressed by powers of m_b/Q are dropped.

This can be written as

$$\sigma^{(4F),(0)}\left(\alpha_s(Q^2),L\right)=\int_{\tau_H}^1\frac{\mathrm{d}x}{x}\int_{\frac{\tau_H}{x}}^1\frac{\mathrm{d}y}{y^2}\sum_{ij=q,g}f_i(x,Q^2)f_j\left(\frac{\tau_H}{xy},Q^2\right)B_{ij}^{(0)}\left(y,L,\alpha_s(Q^2)\right),$$

(3.16)

where

$$B_{ij}^{(0)}\left(y,L,\alpha_s(Q^2)\right)=\sum_{p=2}^N\left(\alpha_s(Q^2)\right)^pB_{ij}^{(0),(p)}\left(y,L\right),$$

(3.17)

and the coefficients $B_{ij}^{(0),(p)}$ satisfy

$$\lim_{m_b\to0}\left[B_{ij}^{(p)}\left(y,\frac{Q^2}{m_b^2}\right)-B_{ij}^{(0),(p)}\left(y,\frac{Q^2}{m_b^2}\right)\right]=0\,.$$

(3.18)

Extracting the coefficients $B_{ij}^{(0),(p)}$ from the massive limit can only be done in cases
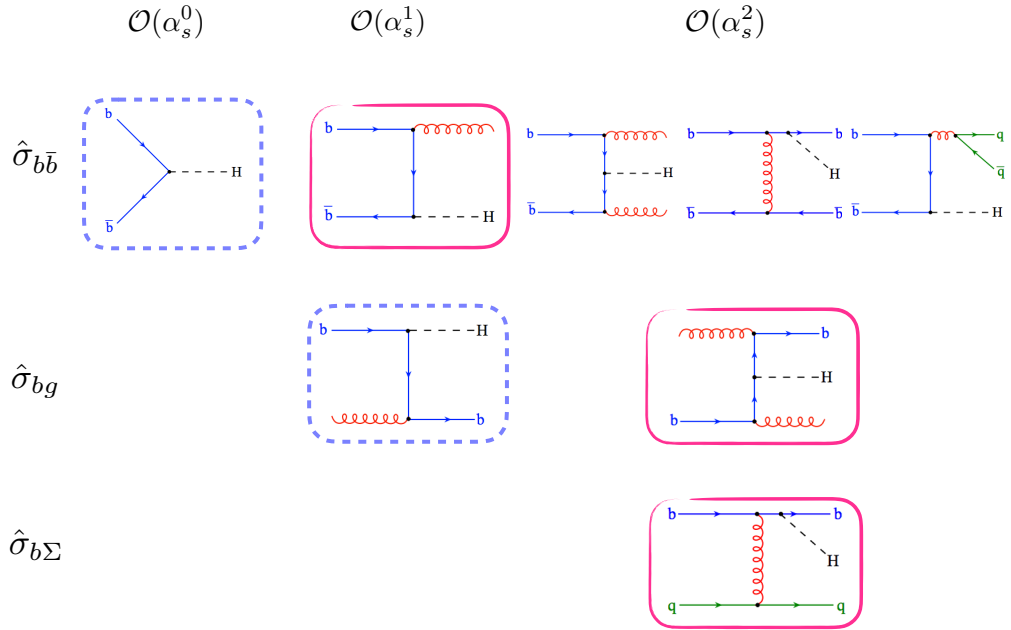
Figure 3.1: Representative examples of contributions to the 5FS computation which are subtracted and get replaced by massive 4FS contributions. The diagrams circled with a dashed line become massive in FONLL-A, while those circled with a solid pink line are those that must be additionally subtracted in the FONLL-B scheme.

in which there exist a simple closed-form expression for the massive coefficients

$B_{ij}^{(p)}$. In most cases, however, this is not doable. All $B_{ij}^{(0),(p)}$ terms in Eq. (3.16) may be equivalently viewed as contributions to the 5FS computation, as schematically summarized in Fig. 3.1 (for real emission terms). This must clearly be true as they account for double counting contributions. To obtain these terms from the 5FS expression we need to express the b-PDF in terms of light quarks and gluon PDFs, Eq. (3.9). At order α_s^2, the result has the following structure:

$$f_b^{(5)}(x, Q^2) = \alpha_s^{(5)}(Q^2) \int_x^1 \frac{\mathrm{d}z}{z} \left\{ \mathcal{A}_{gb}^{(1)}(z, L) f_g^{(5)}\left(\frac{x}{z}, Q^2\right) \right.$$
$$\left. + \alpha_s(Q^2) \left[\mathcal{A}_{gb}^{(2)}(z, L) f_g^{(5)}\left(\frac{x}{z}, Q^2\right) + \mathcal{A}_{\Sigma b}^{(2)}(z, L) f_\Sigma^{(5)}\left(\frac{x}{z}, Q^2\right) \right] \right\}, \quad (3.19)$$

where $f_b^{(5)}$, $f_\Sigma^{(5)}$ and $f_g^{(5)}$ are respectively the 5FS b quark, singlet, and gluon PDFs, and

$$\begin{aligned} \mathcal{A}_{gb}^{(1)} &= a_{gb}^{(1,1)}(z)\, L, \\ \mathcal{A}_{gb}^{(2)} &= a_{gb}^{(2,2)}(z)L^2 + a_{gb}^{(2,1)}(z)L + a_{gb}^{(2,0)}(z), \\ \mathcal{A}_{\Sigma b}^{(2)} &= a_{\Sigma b}^{(2,2)}(z)L^2 + a_{\Sigma b}^{(2,1)}(z)L + a_{\Sigma b}^{(2,0)}(z) \end{aligned} \quad (3.20)$$

Note that, as well known, to $\mathcal{O}(\alpha_s^2)$ the expression of the 5FS $f_b^{(5)}$ in terms of the light quarks and gluon receives constant (i.e. non-logarithmic) contributions $a_{gb}^{(2,0)}(z)$ and $a_{\Sigma b}^{(2,0)}(z)$, and thus it is discontinuous at threshold $Q^2 = m_b^2$ in the massless scheme, as a consequence of it being continuous in the fully massive calculation. The explicit expressions of the coefficients Eq. (3.20) are given in Appendix B for completeness.

We can now collect all contributions to $\sigma^{(4),(0)}$. The $\mathcal{O}(\alpha_s^2)$ terms, already given in Ref. [1], are

$$B_{gg}^{(0)(2)}(y, L) = y \int_y^1 \frac{\mathrm{d}z}{z} \left[2\mathcal{A}_{gb}^{(1)}(z, L)\, \mathcal{A}_{gb}^{(1)}\left(\frac{y}{z}, L\right) \hat{\sigma}_{b\bar{b}}^{(0)}(z) + 4\mathcal{A}_{gb}^{(1)}\left(\frac{y}{z}, L\right) \hat{\sigma}_{gb}^{(1)}(z) \right]$$
$$+ \hat{\sigma}_{gg}^{(2)}(y), \quad (3.21)$$

$$B_{q\bar{q}}^{(0)(2)}(y, L) = \hat{\sigma}_{q\bar{q}}^{(2)}(y); \quad (3.22)$$

while the $\mathcal{O}(\alpha_s^3)$ are [2]

$$
B_{gg}^{(0)(3)}(y,L) = y \int_y^1 \frac{\mathrm{d}z}{z} \left[4\mathcal{A}_{gb}^{(2)}(z,L)\, \mathcal{A}_{gb}^{(1)}\left(\frac{y}{z},L\right) \hat{\sigma}_{b\bar{b}}^{(0)}(z) \right.
$$

$$
\left. + 2\mathcal{A}_{gb}^{(1)}(z,L)\, \mathcal{A}_{gb}^{(1)}\left(\frac{y}{z},L\right) \hat{\sigma}_{b\bar{b}}^{(1)}(z) + 4\mathcal{A}_{gb}^{(2)}\left(\frac{y}{z},L\right) \hat{\sigma}_{gb}^{(1)}(z) + 4\mathcal{A}_{gb}^{(1)}\left(\frac{y}{z},L\right) \hat{\sigma}_{gb}^{(2)}(z) \right],
$$

$$(3.23)$$

$$
B_{gq}^{(0)(3)}(y,L) = y \int_y^1 \frac{\mathrm{d}z}{z} \left[2\mathcal{A}_{\Sigma b}^{(2)}(z,L)\, \mathcal{A}_{gb}^{(1)}\left(\frac{y}{z},L\right) \hat{\sigma}_{b\bar{b}}^{(0)}(z) + 2\mathcal{A}_{\Sigma b}^{(2)}\left(\frac{y}{z},L\right) \hat{\sigma}_{gb}^{(1)}(z) \right.
$$

$$
\left. + 2\mathcal{A}_{gb}^{(1)}\left(\frac{y}{z},L\right) \hat{\sigma}_{qb}^{(2)}(z) \right], \quad (3.24)
$$

which completes our result. Note that in Eqs. (3.21)-(3.24) $\hat{\sigma}_{ij}^{(p)}(x)$ denotes the partonic cross-section in the 5FS, as indicated by the fact that it only depends on the momentum fraction and does not have any dependence on m_b[1].

3.3 Properties of the matched cross section

Using Eqs. (3.19,3.20) we can express the five flavour scheme cross section in terms of only light quarks and gluons. If we do, we see that the five flavour scheme cross section can be written as

$$
\sigma^{(5)} = \int_{\tau_H}^1 \frac{\mathrm{d}x}{x} \int_{\frac{\tau_H}{x}}^1 \frac{\mathrm{d}y}{y^2} \sum_{ij=q,g} f_i^{(5)}(x,Q^2) f_j^{(5)}\left(\frac{\tau_H}{xy},Q^2\right) \sum_{p=0}^N \alpha_s^p \sum_{k=0}^\infty a_{ij}^{(p,k)}(y)\, (\alpha_s\, L)^k .
$$

$$(3.25)$$

In the same spirit, the massless limit of the massive cross section, Eq. (3.16) is given by

$$
\sigma^{(4F),(0)} = \int_{\tau_H}^1 \frac{\mathrm{d}x}{x} \int_{\frac{\tau_H}{x}}^1 \frac{\mathrm{d}y}{y^2} \sum_{ij=q,g} f_i^{(5)}(x,Q^2) f_j^{(5)}\left(\frac{\tau_H}{xy},Q^2\right) \sum_{p=0}^N \alpha_s^p \sum_{k=0}^p a_{ij}^{(p-k,k)}(y)\, L^k .
$$

$$(3.26)$$

Let us now define $\sigma^{(d)}$, called difference term,

$$
\sigma^{(d)} = \sigma^{(5)} - \sigma^{(4F),(0)} ,
$$

$$(3.27)$$

---

[1]unlike the 4FS partonic cross sections $\hat{\sigma}_{ij}^{(p)}\left(x,\frac{Q^2}{m_b^2}\right)$ of Eq. (3.5)

such that

$$\sigma^{\text{FONLL}} = \sigma^{(4)} + \sigma^{(d)} \,. \tag{3.28}$$

This term is then expressed as:

$$\sigma^{(d)} = \int_{\tau_H}^1 \frac{\mathrm{d}x}{x} \int_{\frac{\tau_H}{x}}^1 \frac{\mathrm{d}y}{y^2} \sum_{ij=q,g} f_i^{(5)}(x,Q^2) f_j^{(5)}\left(\frac{\tau_H}{xy}, Q^2\right) \sum_{p=0}^N \alpha_s^p$$
$$\times \left\{ \sum_{k=0}^\infty a_{ij}^{(p,k)}(y)\,(\alpha_s\,L)^k - \sum_{k=0}^p a_{ij}^{(p-k,k)}(y)\,L^k \right\}. \tag{3.29}$$

In the region in which $m_b \sim Q$, we have that $L \sim 0$. In this limit, mass effects dominates over resummation effects and we thus expect the FONLL prediction to match the four flavour one. As a confirmation we see the the two terms in the second line of Eq. (3.29) have the same asymptotic behaviour in this limit, making $\sigma^{(d)}$ vanish.

On the other hand, in the limit in which $m_b \ll Q^2$, by definition of the massless limit of the massive calculation, we have that the four flavour scheme calculation and the massless limit cancel. This leaves the FONLL prediction equal to the five flavour one in this limit, as expected. In any intermediate regime, the first p terms present in the second line of Eq. (3.29) coming from the massless limit, cancel the first p terms coming from the massless calculation, leaving the remaining $\infty - p$ tower of logs resummed in the five flavour scheme. The first p terms, on the other hand are then added back in the four flavour scheme, and thus include mass effects exactly up the p-th order.

3.4 The $b\bar{b} \to H$ FONLL cross section

We now have all the ingredients to construct the matched result. As everything in Eq. (3.3) is now expressed in terms of the same perturbative objects we can perform an α_s expansion on the final result,

$$\sigma^{\text{FONLL}} = \alpha_s^2(Q^2)\sigma^{(2)} + \alpha_s^3(Q^2)\,\sigma^{(3)} + \mathcal{O}(\alpha_s^4)\,. \tag{3.30}$$

In the rest of this work, following the notation set in [29], we identify with FONLL-A the order α_s^2 [1] term of Eq. (3.30), while we call FONLL-B the contribution to order

α_s^3 [2]. The accuracy of these two schemes is given by the two matched calculations. In the FONLL-A matching, the 5F NNLL cross section (which is order α_s^2) to the 4FS LO ($\mathcal{O}(\alpha_s^2)$) cross section thus having NNLL+LO accuracy. In the FONLL-B matching, mass effects are included up to NLO ($\mathcal{O}(\alpha_s^3)$) which then corresponds to a NNLL+NLO matched scheme.

We have implemented our final FONLL-B expression by combining, according to Eq. (3.3) 4FS predictions up to NLO obtained using MG5_aMC@NLO [37,38], 5FS computations up to NNLL obtained using the `bbh@nnlo` code [30], and our own implementation of the subtraction term Eq. (3.16).

In Figs. 3.2-3.4 we compare the 4FS, 5FS and matched FONLL results. Specifically, in Figs. 3.2-3.3 we show for the physical Higgs mass value $m_H = 125$ GeV, varying the renormalisation and factorisation scale both the LO and NLO 4FS predictions, and the FONLL-A and FONLL-B matched results in which they are respectively combined with the NNLL 5FS result, also shown. In Fig. 3.4 we show the most accurate results obtained in the 4FS (NLO), 5FS (NNLO) and matched (FONLL-B) schemes, as a function of the Higgs mass, with $\mu_R = \mu_F = \frac{m_H + 4m_B}{4}$, and the uncertainty band obtained by taking the envelope of the variations of the renormalisation and factorisation scales by a factor two about the central value with the two outer points $\mu_R = 4\mu_F$ and $\mu_F = 4\mu_R$ omitted. Note that for the lowest (unphysical) Higgs mass values this uncertainty blows up because the lower edge of the scale variation range extends in the nonperturbative region.

The 4FS results shown are those which enter the FONLL combination, namely, the form Eq. (3.6) of the 4FS result is used, in which this is expressed in terms of 5FS PDFs and α_s. All results are computed using a PDF set presented and discussed in [39]. This PDF set is based on the PDF4LHC15 combined sets [40–46], with which it is taken to coincide below the b mass, but from which it is then evolved up in the 5FS from $Q = m_b$, with the results below and above threshold matched exactly as in Eq. (3.19). This is not quite the same as the original PDF4LHC15 combination, which is obtained by combining sets which adopt different values of m_b, and also incorporate subleading differences in the way the 4FS and 5FS are matched at threshold: it thus has the advantage of being fully consistent. We use pole-mass
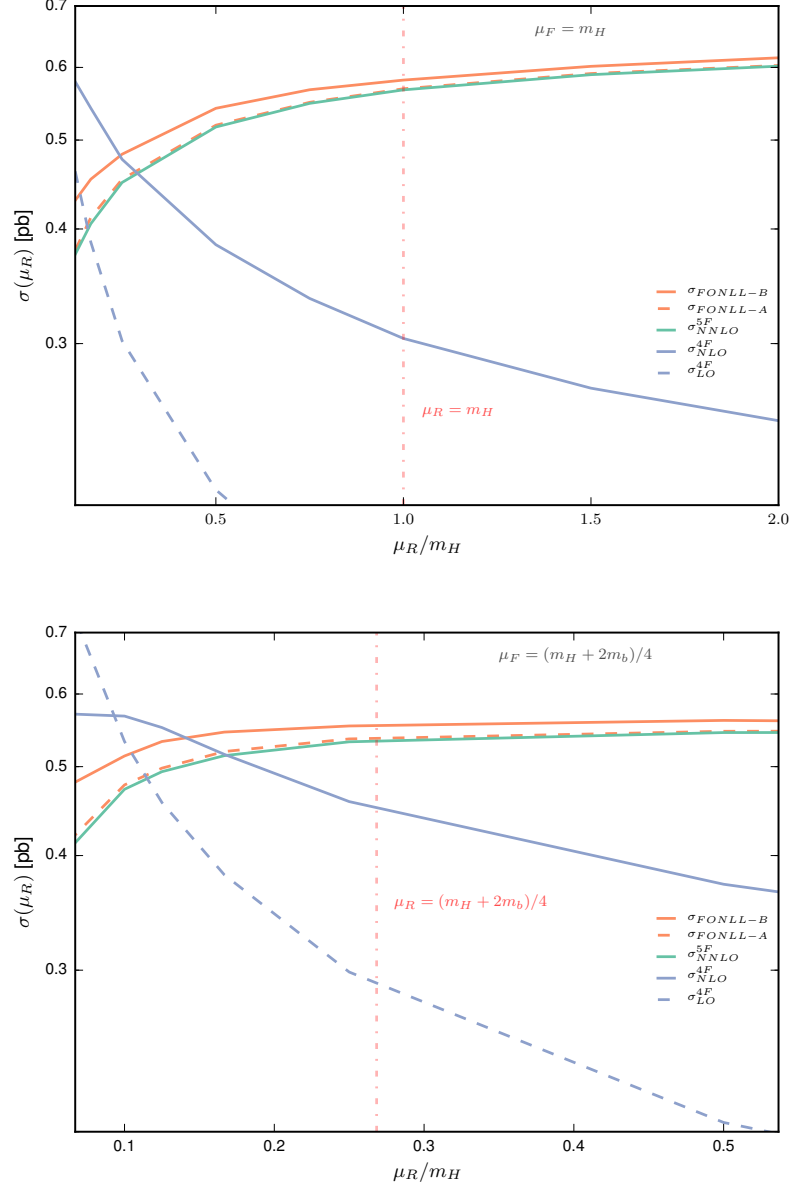
Figure 3.2: Comparison of the FONLL matched result and its 4FS and 5FS components, Eq. (3.3). Results are shown as a function of the renormalisation scale, with the factorisation scale fixed at a high value $\mu_F = m_H$ (top) or a low value $\mu_F = \frac{(m_H + 2m_b)}{4}$ (bottom).
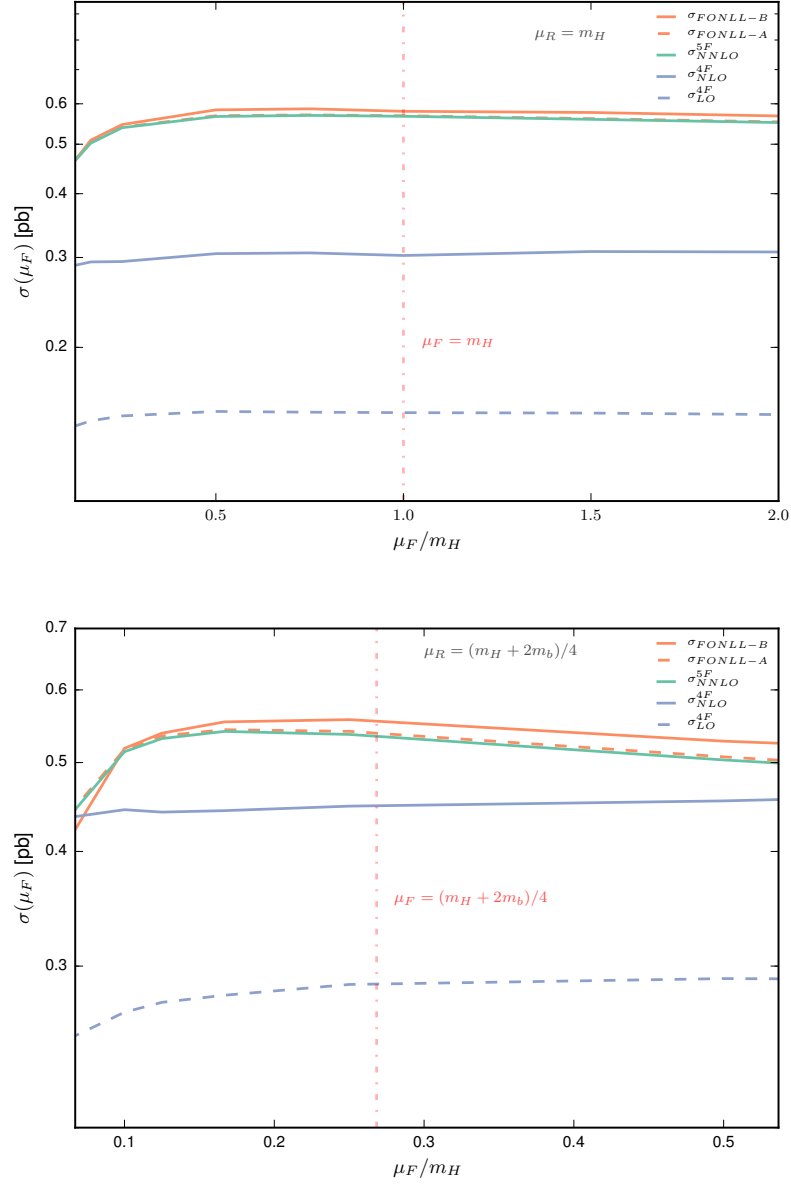
Figure 3.3: Same as Fig. 3.2, but now with the factorisation scale varied with the renormalisation scale kept fixed at a high value $\mu_R = m_H$ (top) or a low value $\mu_R = \frac{(m_H + 2m_b)}{4}$ (bottom) .

expressions and take a b pole-mass value $m_b = 4.58$ GeV; the strong coupling is $\alpha_s(m_Z) = 0.118$.

From Fig. 3.2 we see that the strong renormalisation scale dependence of the LO 4FS result is reduced at NLO, and also, that at NLO the big gap between the 4FS and 5FS results gets compensated for by the inclusion of higher order terms in the 4FS. This, together with the fact that the 5FS shows very little scale dependence, and that differences are significantly smaller for smaller values of μ_F, strongly suggests that the bulk of the difference between the 4FS and the 5FS is due to large logs of μ_F^2/m_b^2 which are resummed into the PDF in the latter case. This is in agreement with the conclusion of [34], in which it was shown that resummation increases the cross section in most cases by up to 30% at the LHC, leading to a better precision. On the other hand, the 4FS predictions at NLO also displays a consistent perturbative behaviour only when evaluated at a suitably low scale.

The massive corrections which the 4FS result contains turn out to be much smaller, though not entirely negligible. Indeed, whereas the FONLL-A result essentially coincides with the 5FS, the FONLL-B, which only differs from it because of the inclusion of massive terms at one extra perturbative order, departs somewhat from it. The factorisation scheme dependence shown in Fig. 3.3 is very mild in all schemes when μ_R is high, but for low μ_R, where the perturbative expansion of the 4FS result is more reliable, both the 5FS and the FONLL-A results show a contained scale dependence, comparable in size to the mass effects, which is reduced in the FONLL-B result.

These results suggest that the main difference between the FONLL-A and the FONLL-B schemes is the inclusion of a higher order contribution from the 4FS computation which reduces the the scale dependence of the FONLL-A result; because the latter is essentially the same as that of the 5FS computation this contribution is likely to be dominated by a constant, i.e., mass-independent term. This conclusion is supported by Fig. 3.4, in which results are shown as a function of the Higgs mass: the difference between the FONLL-B and 5FS results decreases slightly as the mass grows until $m_H \sim 200$ GeV, but then remains constant up to the highest values of the Higgs mass.
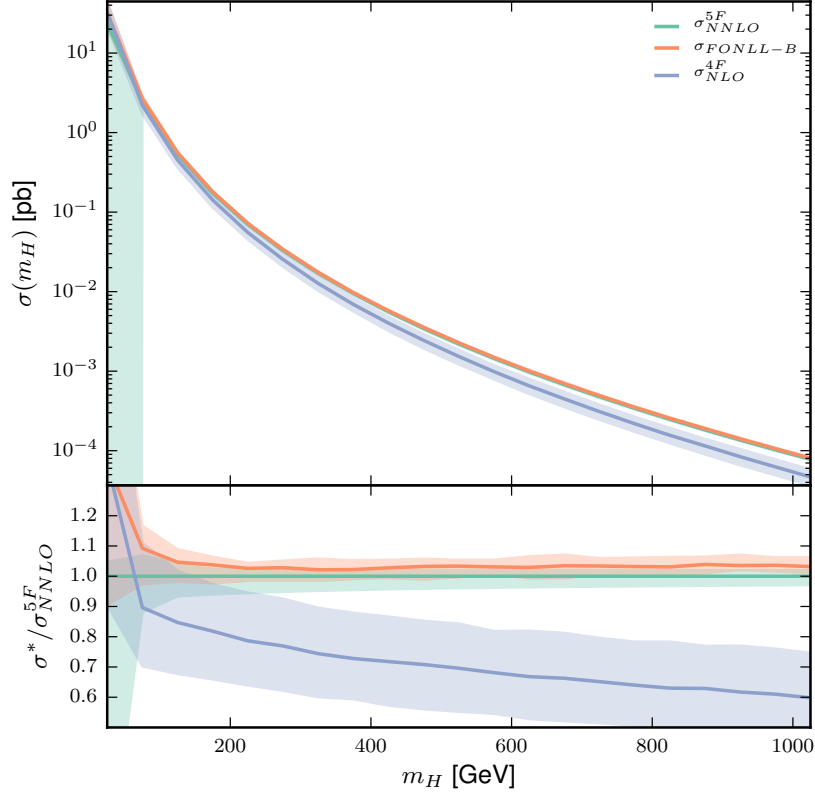
Figure 3.4: The cross-section using the most accurate results in the 4FS (NLO), 5FS (NNLO) and matched (FONLL-B) schemes, as a function of the Higgs mass, with $\mu_r = \mu_F = \frac{(m_H + 2m_b)}{4}$. The bottom panel shows the result as a ratio to the 5FS computation. The uncertainty band is obtained by standard seven-point scale variation (see text).

We conclude that the FONLL-B result is the most reliable, and a low choice of renormalisation and factorisation scheme seems to lead to a more reliable perturbative expansion. All in all mass corrections are very moderate, so the usage of the 5FS result at all scales would be adequate in most cases. This rather disfavours phenomenological combinations such as the so-called Santander matching [35] in which the 4FS and 5FS results are combined through an interpolation that gives each of them comparable weight. The difference between the FONLL-B and 5FS is almost entirely due to a constant $O(\alpha_s^3)$ mass-independent contribution which appears in the 4FS at NLO but would only enter the 5FS at N^{3}LO; the FONLL-B computation, which includes it, is accordingly more accurate, even for very high vales of the Higgs mass.

In conclusion, we find that mass corrections are very small while collinear logs are substantial, so that in practice the fully matched result is very close to the 5FS one. The fully matched result receives a small correction from mass effects and it is very stable upon renormalisation and factorisation scheme variation, suggesting that it is adequate for precision phenomenology at the LHC.

Chapter 4

Comparing the 4F and the 5F scheme: heavy boson production

4.1 Introduction

Processes involving heavy flavours at the LHC, like the production of a heavy boson $(V = W, Z, H)$ in association with bottom (b) quarks present an interesting study case of heavy flavour modeling and have recently attracted renewed interest for a number of old and new reasons [33,34,38,47–49]. Firstly, the associated production of a vector boson with b-tagged jets points to born level processes like $gb \rightarrow Vb$ which is sensitive to the b-quark Parton Distribution Function (PDF), the precise determination of which is fundamental for phenomenologically relevant processes like the production of a Higgs boson in bottom-quark fusion [1,2,39,50]. This sensitivity also helps disentangle the relative effects of resummation to fixed order mass effects.

Secondly, and complementary to this purely Standard-Model reasoning, many models for physics beyond the Standard Model come with extended Higgs sectors, quite often in the form of a second Higgs doublet. The mixing among the Higgs doublets often amplifies the couplings of the Higgs bosons to the b-quarks. As a consequence, bH and $b\bar{b}H$ production provide important search grounds for new physics. Furthermore, events with identified b-jets and a significant missing transverse momentum constitute a possible signature of Dark Matter [51–53] production. For this signal invisibly decaying Z-bosons associated with b-jets pose a severe irre-

ducible background.

In general, these processes have always been approached in either of two schemes, commonly known as the four or five-flavour scheme (4FS and 5FS). In the 4FS, bottom quarks are completely decoupled from both the running of the strong coupling constant (α_s) and the evolution of PDFs. In addition all mass effects are retained everywhere in the calculation. In the 5FS, on the other hand, mass effects are completely neglected, and b-quarks are treated on the same footing as any other light-quark. In particular, they contribute to both α_s and PDFs evolution. A more detailed description of these two approaches is carried on in Sec. (2.1).

We can make use of a simple argument to see where problems can arise. From dimensional analysis in fact, we now that mass effects must appear as ratio of scales, namely the mass of the heavy quarks (m_Q in general, m_b in particular) and some other scale (Q) in the process. When looking at inclusive observables, we typically have to deal with only one scale, like the invariant mass of the final state. In such cases, it is easy to argue if mass effects will play an important role or not.

However, experimental analyses often consider differential distributions, like the transverse-momentum (p_T) or the invariant mass of a subset of particles in the final state. This introduces additional scales that are not a fixed number, but vary event by event, making the ratio m_b/Q a number that can be both small and large in the same observable.

In the rest of this chapter, we study differences between the 4FS and the 5FS. In particular we compare the two schemes in the context of the production of heavy quarks in association with a Z boson, where we further compare with LHC data. We then use the comparison with data to extend our discussion to the case of H associated production.

4.2   Bottom-jet associated Z-boson production

The production of a Z boson in association with QCD jets provides the ideal test bed for the theoretical approaches outlined above. Through the decay of the Z boson to leptons these processes yield a rather simple and clean signature with sizeable

rates even for higher jet counts. Precise measurements of the production rates and differential distributions of both the Z-boson decay products and the accompanying jets offer discriminating power for miscellaneous theoretical approaches. In fact, measurements of Z+jets production served as key inputs for the validation of matrix-element parton-shower simulation techniques, cf. [54–56], and impressively underpin the enormous success of these calculational methods.

Here we focus on the production of Z bosons accompanied by identified b-jets. Comparison with data from both the ATLAS and CMS collaborations at 7 TeV [57, 58] provides the benchmark for the accuracy and quality of four– and five–flavour simulations with SHERPA. Similar measurements at 8 and 13 TeV LHC collision energies are under way [59].

4.2.1   Details of the simulations

Efficient routines for the required QCD matrix-element calculations and a well understood QCD parton-shower are the key ingredients to all matching and merging calculations. Within SHERPA LO matrix elements are provided by the built-in generators AMEGIC++ [60] and COMIX [61]. While virtual matrix elements contributing to QCD NLO corrections can be invoked through interfaces to a number of specialised tools, e.g. BLACKHAT [62], GOSAM [63], NJET [64], OPENLOOPS [65] or through the BLHA interface [66], we employ in this study the OPENLOOPS generator [67] in conjunction with the COLLIER library [68, 69]. Infrared divergences are treated by the Catani–Seymour dipole method [15, 16] which has been automated in SHERPA [70]. In this implementation mass effects are included for final-state splitter and spectator partons but massless initial-state particles are assumed throughout. SHERPA's default parton-shower model [71, 72] is based on Catani–Seymour factorisation [73]. In order to arrive at meaningful fragmentation functions for heavy quarks, all modern parton showers take full account of their finite masses in the final state, although in algorithmically different ways. In SHERPA, the transition from massless to massive kinematics is achieved by rescaling four-momenta at the beginning of the parton shower. In the initial-state parton shower in SHERPA, the $g \to b\bar{b}$ and $b \to bg$ splitting functions do not contain b-quark mass effects in their functional form and

account for mass effects in the kinematics only.

In the following we briefly define the methods available in SHERPA for simulating b-associated production processes, that will then be validated and applied for LHC predictions:

4F NLO (4F MC@NLO): In the *four–flavour scheme*, b-quarks are consistently treated as *massive* particles, only appearing in the final state. As a consequence, b-associated Z- and H-boson production proceeds through the parton-level processes $gg \to Z/H + b\bar{b}$, and $q\bar{q} \to Z/H + b\bar{b}$ at Born level. MC@NLO matching is obtained by consistently combining fully differential NLO QCD calculations with the parton shower, cf. [74,75]. Due to the finite b-quark mass these processes do not exhibit infrared divergences and the corresponding *inclusive* cross sections can thus be evaluated without any cuts on the b-partons.

5F LO (5F MEPS@LO): In the *five–flavour scheme* b-quarks are *massless* particles in the *hard matrix element*, while they are treated as massive particles in both the initial- and final-state *parton shower*.

In the MEPS@LO [25] samples we merge $pp \to H/Z$ plus up to three jets at leading order; this includes, for instance, the parton–level processes $b\bar{b} \to Z/H$, $gb \to Z/Hb$, $gg \to Z/Hb\bar{b}$, ... To separate the various matrix-element multiplicities, independent of the jet flavour, a jet cut of $Q_{\mathrm{cut}} = 10\,\mathrm{GeV}$ is used in the Z case while $Q_{\mathrm{cut}} = 20\,\mathrm{GeV}$ is employed in H-boson production.

5F NLO (5F MEPS@NLO): In the 5FS MEPS@NLO scheme [27,76], we account for quark masses in complete analogy to the LO case: the quarks are treated as massless in the hard matrix elements, but as massive in the initial- and final-state parton showering. Again, partonic processes of different multiplicity are merged similarly to the MEPS@LO albeit retaining their next-to-leading-order accuracy. In particular, we consider the merging of the processes $pp \to H/Z$ plus up to two jets each calculated with MC@NLO accuracy further merged with $pp \to H/Z + 3j$ calculated at MEPS@LO.

$$
\mathrm{d}\sigma^{4\mathrm{F\ Mc@Nlo}} = \mathrm{d}\Phi_3 \ \left| \ \vcenter{\hbox{}} \ + \ \mathcal{V} \ \right|^2 \ \otimes \ \Pi^{\mathrm{PS}}
$$

$$
+ \ \ \mathrm{d}\Phi_4 \ \left| \ \vcenter{\hbox{}} \ \right|^2 \ \otimes \ \Pi^{\mathrm{PS}}
$$

Figure 4.1: Pictorial representation of $V + b\bar{b}$ processes contributing to the 4F Mc@Nlo calculation. Here $V = (Z, H)$ and by $\otimes$ we just mean that it is not a simple product, and P.S. is the parton shower contribution. $\mathcal{V}$ refers to the one-loop virtual contributions to the born.

$$\mathrm{d}\sigma^{\text{5F MEPS@LO}} = \mathrm{d}\Phi_1 \; \left| \vphantom{\Bigg|} \right|^2 \otimes \Pi^{\mathrm{PS}} \; \oplus \; \mathrm{d}\Phi_2 \; \left| \vphantom{\Bigg|} \right|^2 \otimes \Pi^{\mathrm{PS}}$$

$$\oplus \; \mathrm{d}\Phi_3 \; \left| \vphantom{\Bigg|} \right|^2 \otimes \Pi^{\mathrm{PS}} \; \oplus \; \mathrm{d}\Phi_4 \; \left| \vphantom{\Bigg|} \right|^2 \otimes \Pi^{\mathrm{PS}}$$

Figure 4.2: Same as Fig. 4.1 but for the 5F MEPS@LO. The $\oplus$ symbol represents the merging, *i.e.* a sum with the overlapping part removed. Note that in the five flavour scheme the bottom contribution is included in q.

We consistently use four–flavour PDFs in the 4F scheme, i.e. the dedicated four–flavour NNPDF3.0 set [41] with the strong coupling given by $\alpha_s(m_Z) = 0.118$ and running at NLO. For the simulations in the five–flavour schemes the five-flavour NNLO PDFs from NNPDF3.0 are used, with $\alpha_s(m_Z) = 0.118$ and running at NNLO. We assume all quarks apart from the b to be massless, with a pole mass of $m_b = 4.92$ GeV which enters the hard matrix-element calculation, where appropriate, and the parton shower.

Results in the 4F and 5F schemes have been obtained with the default scale-setting prescription for parton-shower matched calculations in SHERPA [25,77]. They are calculated using a backward-clustering algorithm, and for each emission from the shower, couplings are evaluated at either the k_T of the corresponding emitted particle (in the case of gluon emission), or at the invariant mass of the emitted pair (in the case of gluon splitting into quarks). The clustering stops at a "core" $2 \rightarrow 2$ process, with all scales set to $\mu_F = \mu_R = \mu_Q = m_T(V)/2$, where $m_T(V)$ corresponds to the transverse mass of the boson. This scale is thus used to evaluate couplings in the hard matrix element and PDFs. The corresponding central values are supplemented with uncertainty bands reflecting the dependence on the unphysical scales. Renormalisation and factorisation scales are varied around their central value by a factor of two up and down, with a standard 7-point variation. The scale variations use the SHERPA internal reweighting procedure [78] and result in envelopes around the central value. Furthermore, we consider explicit variations of the parton-shower starting scale, i.e. μ_Q, by a factor of two up and down.

4.2.2 Parton shower mass corrections

When producing predictions involving heavy quarks there are a number of subleading effects that can be turned on or off. This happens in particular in the parton shower part. As we discuss in Section 2.4, in fact, the Shower evolution is determined by the exact definition of the Sudakov form factor,

$$\Delta_N(t_0, t) = \exp\left[-\int d\Phi_1 \, K_N(\Phi_1)\right] \tag{4.1}$$

with $K_N(\Phi_1)$ some splitting kernels. As we are using a dipole shower, in the context of this study, we can identify $K_N(\Phi_1)$ with Catani-Seymour dipoles splitting functions. As long as the correct limits are recovered by the splitting functions, and one knows all the phase-space mappings needed to define the projected phase space, one can use any splitting function. This imply that any non-divergent, mass proportional, addition to the splitting kernels is subleading. In the simulations we present here we do not include any additional mass effects, other than the ones that are already present and described in [71].

Another subtlety stems when looking at the definition of $K_N(\Phi_1)$,

$$K_N(\Phi_1) = \frac{\alpha_s}{2\pi} \sum_{(i,j)\neq k} \frac{\mathcal{D}_{ij,k}}{\mathcal{B}_N} = \frac{\alpha_s}{2\pi} \frac{\mathcal{S}}{\mathcal{B}_N} \,. \tag{4.2}$$

The point at which α_s should be evaluated in this formula, is the evolution variable. In dipole based shower, like the one we discuss here, this parameter is calculated as the transverse momentum of the splitting k_T. Imagine now the splitting of a gluon into a $b\bar{b}$ pair. As the b quarks, in the shower, are always treated as massive particles, it is unlikely that they are produced very collinear. On the other hand k_T can, in principle, be very small. Now α_s is a decreasing function of k_T. This means that lower k_T splitting have a higher weight, and thus a larger probability. This issue can be fixed by evaluating α_s in the context of $g \to b\bar{b}$ splittings at the invariant mass of the splitted pair, $m_{b\bar{b}}$. This setting is the default setting we use in this study.

As a last comment, let us underline how, however, the setup used here, and presented in the previous section, makes most of these effects less important, at least in the two five falvour scheme samples. The idea is that we exploit the merging scale, Q_{cut}, to reduce the influence of the parton shower in many regions of phase space. To do that we choose Q_{cut} such that

$$m_b < Q_{\text{cut}} < p_T^{\text{cut}} \,, \tag{4.3}$$

where p_T^{cut} is the cut on p_T applied to jets in the analysis. This low value makes then sure that most of the samples are populated by matrix elements, with the parton shower dominating only in the regions of very soft jets.

4.2.3 Measurements at LHC Run I – the reference data

Based on a data set of 4.6 fb^{-1} integrated luminosity the ATLAS collaboration studied the production of b-jets associated with Z/γ^* that decay to electrons or muons [57]. The dilepton invariant mass ranges between 76 GeV $< m_{\ell\ell} <$ 106 GeV. Jets are reconstructed using the anti-k_t algorithm [79] with a radius parameter of $R = 0.4$, a minimal transverse momentum of $p_{T,j} > 20$ GeV and a rapidity of $|y_j| < 2.4$. Furthermore, each jet candidate needs to be separated from the leptons by $\Delta R_{j\ell} > 0.5$. Jets containing b-hadrons are identified using a multi-variate technique. To match the outcome of the experimental analysis, simulated jets are identified as b-jets, when there is one or more weakly decaying b-hadron with $p_T > 5$ GeV within a cone of $\Delta R = 0.3$ around the jet axis. The sample of selected events is further subdivided into a class containing events with at least one b-jet (1-tag) and a class with at least two b-jets (2-tag).

A similar analysis was performed by CMS [58]. There, electrons and muons are required to have a transverse momentum of $p_{T,\ell} > 20$ GeV, a pseudorapidity $|\eta_\ell| < 2.4$, and a dilepton invariant mass within 81 GeV $< m_{\ell\ell} <$ 101 GeV. Only events with exactly two additional b-hadrons were selected. The analysis focuses on the measurement of angular correlations amongst the b-hadrons and with respect to the Z boson. This includes in particular variables sensitive to rather collinear b-hadron pairs. In addition, the total production cross section as a function of the vector boson's transverse momentum was measured.

Both analyses are implemented and publicly available in the RIVET analysis software [80] that, together with the FASTJET package [81], is employed for all particle, i.e. hadron, level analyses.

4.2.4 Comparison with LHC data

In this section the theoretical predictions from SHERPA are compared to the experimental measurements from LHC Run I. We begin the discussion with the comparison with the measurements presented by the ATLAS collaboration in Ref. [57]. The total cross sections for $Z+ \geq 1$ and $Z+ \geq 2$ b jets are collected in Fig. 4.3. Already

there we see a pattern emerging that will further establish itself in the differential cross sections: While the 5F MEPS@NLO results agree very well with data, the central values of the 5F MEPS@LO cross sections tend to be around 10-20% lower than the central values of data, but with theory uncertainties clearly overlapping them. For all the runs the uncertainty estimates include both, 7-point variations of the perturbative scales $\mu_{R/F}$, as well as μ_Q variations by a factor of two up and down. In contrast to the 5F case, the 4F MC@NLO cross sections tend to be significantly below the experimental values for the $Z+ \geq 1$ b-jets cross section, without overlap of uncertainties. In the $Z+ \geq 2$ b-jets cross section the agreement between 4F MC@NLO results and data is better, with the theoretical uncertainties including the central value of the measured cross section.

In Fig. 4.4 the differential cross sections with respect to the transverse momentum and rapidity of the b-jets, normalised to the number of b-jets, are presented for events with *at least* one b-tagged jet. The shapes of both distributions are well modelled both by the 4F and the two 5F calculations. However, clear differences in the predicted production cross sections are observed. While the 5F NLO results are in excellent agreement with data - both in shape and normalisation - the central values of the 5F LO cross sections tend to be around 10% below data, at the lower edge of the data uncertainty bands, and the 4F results are consistently outside data, about 25% too low. In the lower panels of Fig. 4.4 and all the following plots in this section we show the uncertainty bands of the theoretical predictions, corresponding to the above described $\mu_{R/F}$ and μ_Q variations. For the 5FS calculations the scale uncertainties clearly dominate, while for the 4F MC@NLO scheme the shower-resummation uncertainty dominates.

This pattern is repeated in Fig. 4.5, where we show the differential $\sigma(Zb)$ cross section with respect to the dilepton transverse momentum and, rescaled to $1/N_{b-\text{jets}}$, as a function of the azimuthal separation between the reconstructed Z boson and the b-jets. Again, both distributions are very well modelled by both 5F calculations. The 4F MC@NLO prediction again underestimates data by a largely flat 20-25%.

Lastly for the one b-jet inclusive sample, we look at the rapidity and ΔR separation between the Z boson and the leading b-jet, Fig. 4.6. In these two plots the
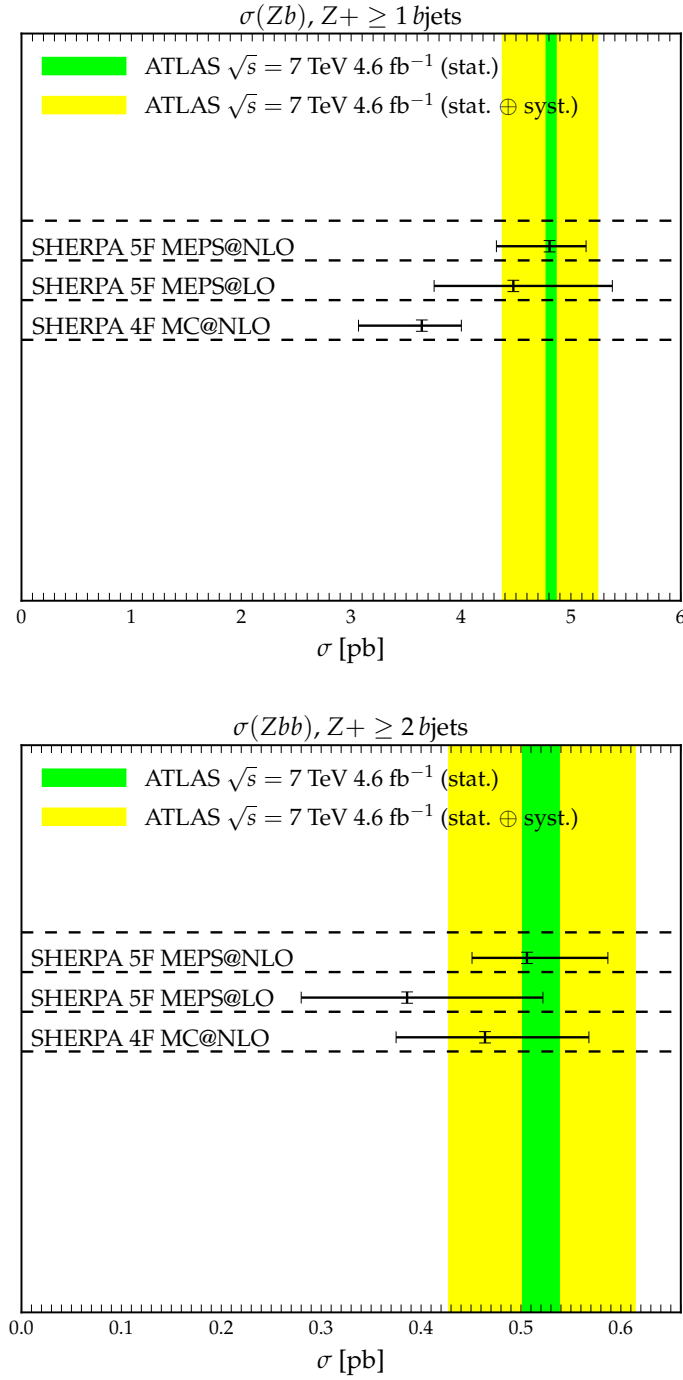
Figure 4.3: Comparison of total production cross section predictions with ATLAS data [57]. The error bars on the theoretical results are calculated from variations of the hard-process scales $\mu_{R/F}$ and the parton-shower starting scale μ_Q.

additional constraint that $p_{T,ll} > 20$ GeV is imposed. This case too highlight how the three schemes differ from one another by a constant factor. In particular the
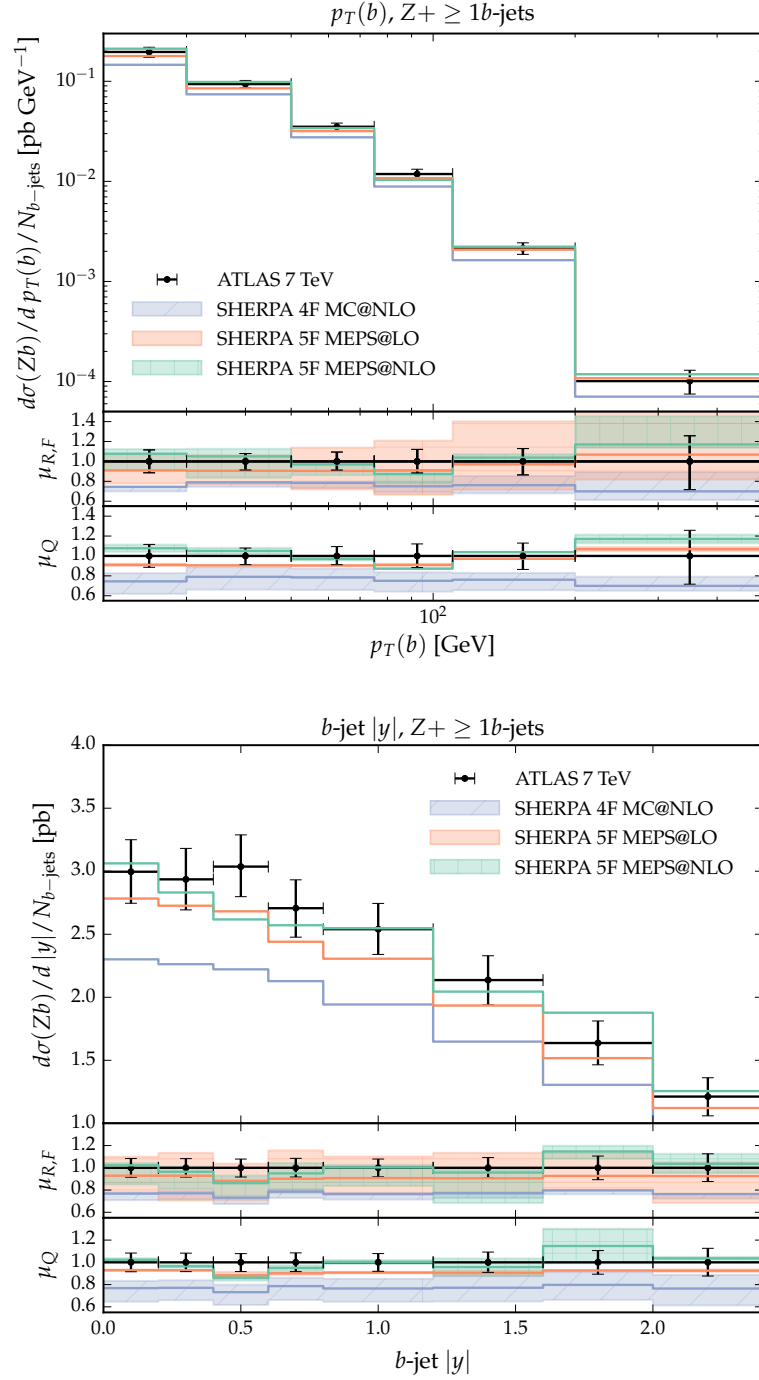
Figure 4.4: Inclusive transverse-momentum and rapidity distribution of all *b*-jets in events with at least one *b*-jet. Data taken from Ref. [57].

MEPS@NLO 5FS provide once again with the most accurate prediction, while the 4F MC@NLO undeshoot data by a roughly 20% factor. Somehow more interesting is the ΔR separation between the Z boson and the leading *b*-jet. In this case in
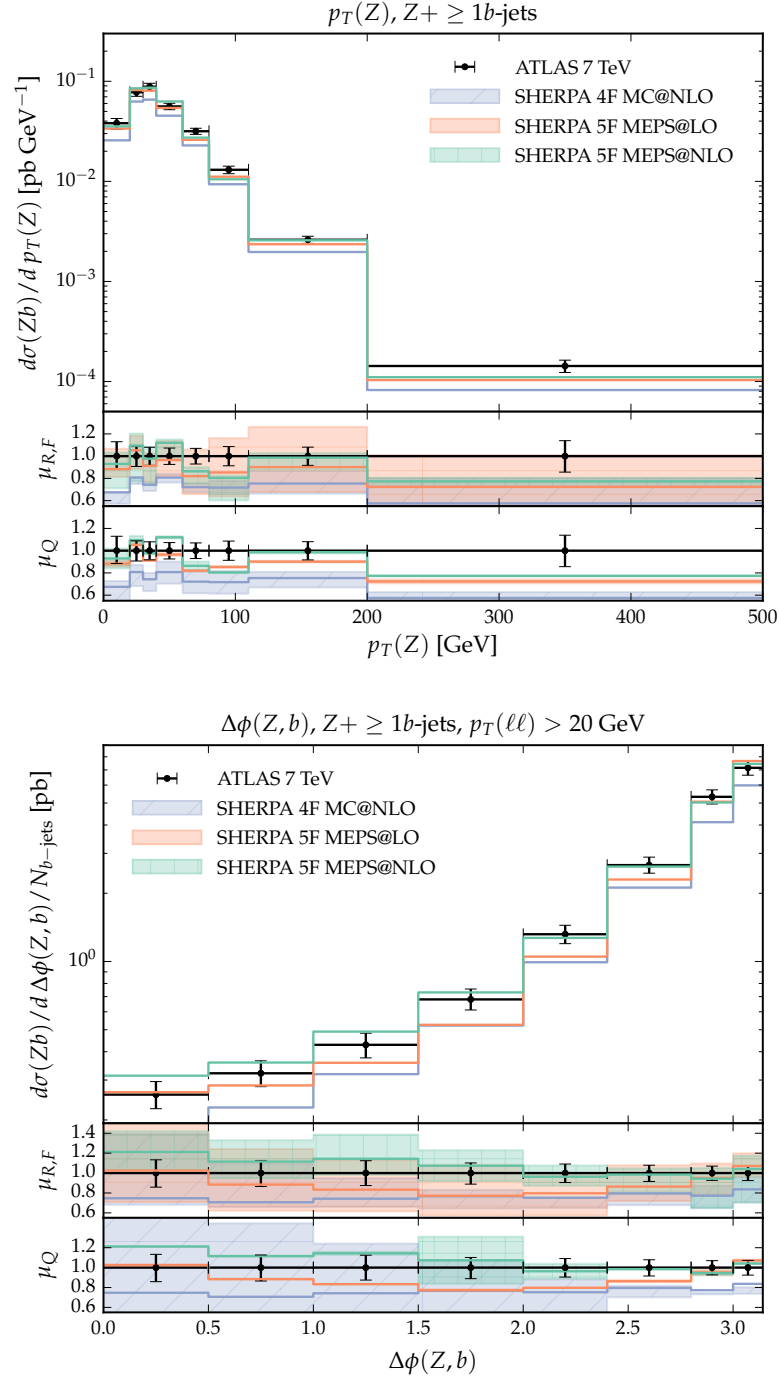
Figure 4.5: Transverse-momentum distribution of the Z boson (left) and the azimuthal separation between the Z boson and the b-jet (right) in events with at least one b-jet. For the $\Delta\phi(Z,b)$ measurement the additional constraint $p_{T,ll} > 20$ GeV is imposed. Data taken from Ref. [57].
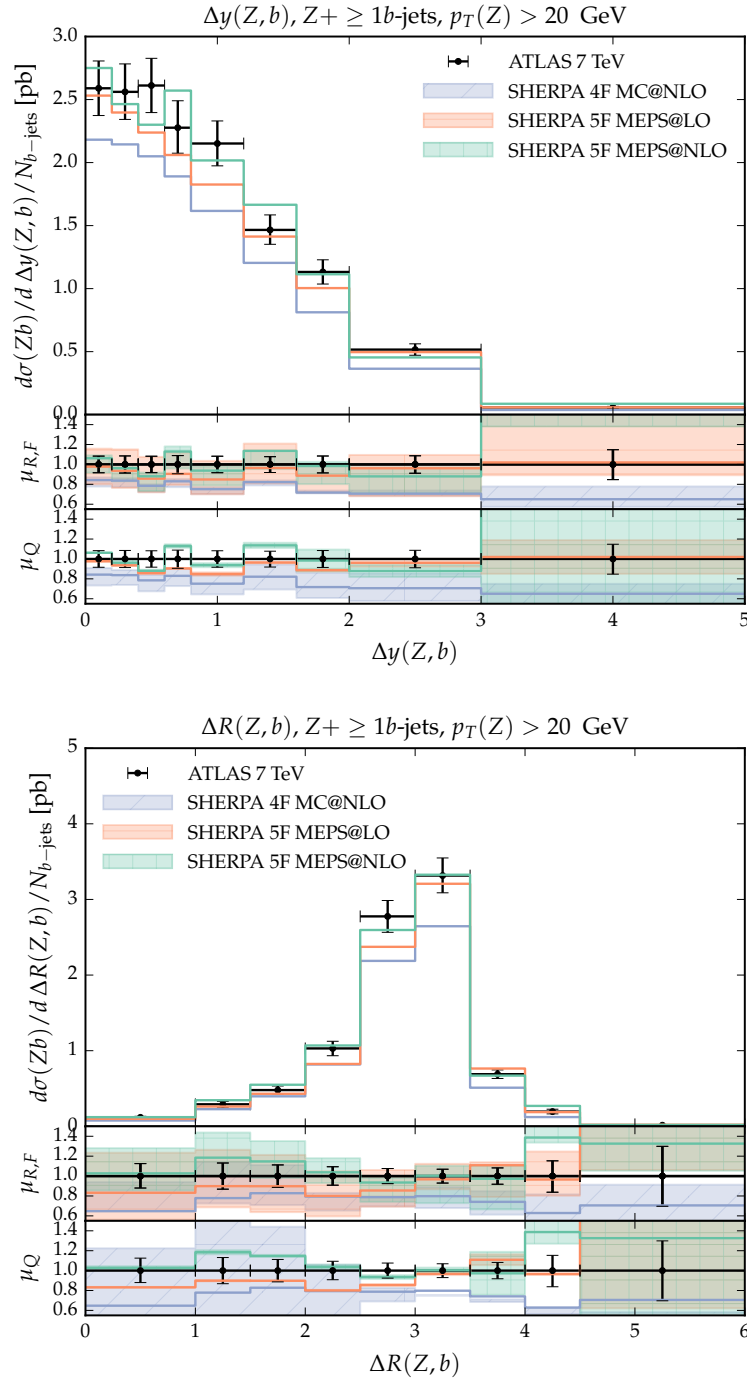
Figure 4.6: Difference in rapidity and ΔR separation between tne Z boson and the first b-jet in events with at least one b-jet, with the additional constraint $p_{T,ll} > 20$ GeV. Data taken from Ref. [57].

fact we notice some shape distortion in the $\Delta R \geq 4$ region. In this region the two 5FS predictions somehow depart from being a constant factor with respect to the

4FS MC@NLO. This is due to the low merging scale that has been used in this case, which moves the transition region to lower ΔR values, thus affecting this plot.

Moving on to final states exhibiting at least two identified b-jets, the role of the 5F LO and 4F NLO predictions are somewhat reversed: As can be inferred from Fig. 4.3, the 4F and 5F NLO samples provide good estimates for the inclusive Zbb cross section, while the 5F LO calculation undershoots data by about 20%. In Fig. 4.7 the ΔR separation of the two highest transverse-momentum b-jets along with their invariant-mass distribution is presented. Both the 4F and the 5F approaches yield a good description of the shape of the distributions. It is worth stressing that this includes the regions of low invariant mass and low ΔR, corresponding to a pair of rather collinear b-jets. This is a region that is usually riddled by potentially large logarithms, where the parton shower starts taking effect. Note that in the comparison presented in [57] this region showed some disagreement between data and other theoretical predictions based on NLO QCD (dressed with parton showers).

In Fig. 4.8 the resulting transverse-momentum distribution of the dilepton system when selecting for events with at least two associated b-jets is shown. The shape of the data is very well reproduced by the 4F MC@NLO and 5F MEPS@NLO samples. Also the 5F MEPS@LO prediction describes the data well despite of the overall rate being 20% lower than observed in data.

The measurements presented by the CMS collaboration in Ref. [58] focus on angular correlations between b-hadrons rather than b-jets. Two selections with respect to the dilepton transverse momentum have been considered, a sample requiring $p_T(Z) > 50$ GeV and an inclusive one considering the whole range of $p_T(Z)$. The ΔR and $\Delta\phi$ separation of the b-hadrons obviously prove to be most sensitive to the theoretical modelling of the b-hadron production mechanism and the interplay of the fixed-order components and the parton showers. They are presented in Figs. 4.9 and 4.10. In general, a good agreement in the shapes of simulation results and data is found, with the same pattern of total cross sections as before: the 5F MEPS@NLO sample describes data very well, while the 4F MC@NLO results tend to be a little bit, about 10%, below data, with data and theory uncertainty bands well overlapping, while the central values of the 5F MEPS@LO results undershoot data by typically
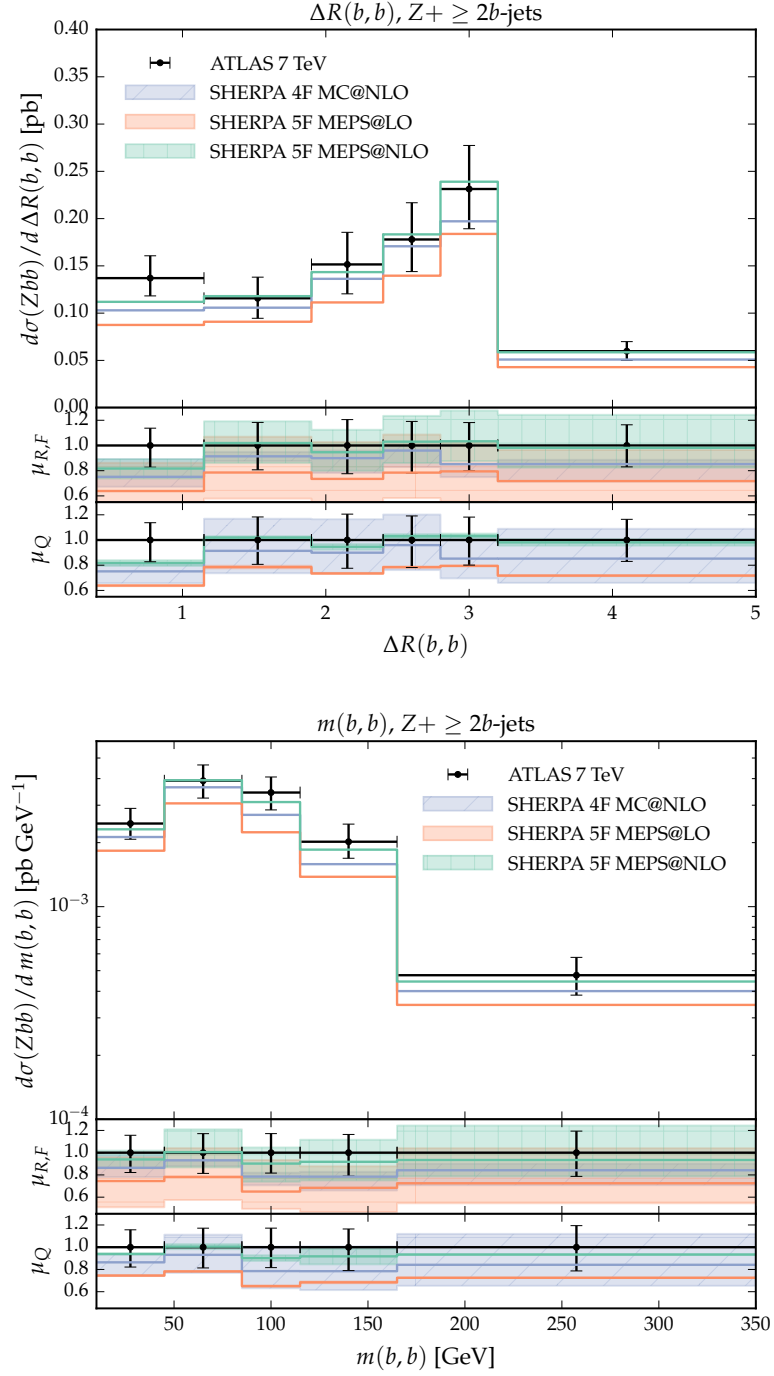
Figure 4.7: The ΔR separation (left) and invariant-mass distribution (right) for the leading two b-jets. Data taken from Ref. [57].

20-25%.

Overall it can be concluded that the 5F MEPS@NLO calculation yields the best description of the existing measurements, regarding both the production rates *and*
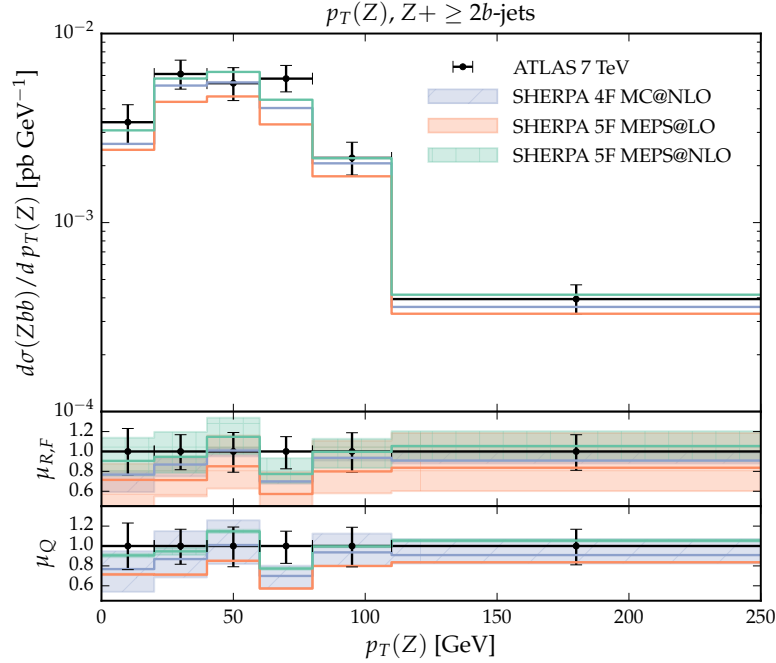
Figure 4.8: Transverse-momentum distribution of the dilepton system for events with at least two b-jets. Comparison against various calculational schemes. Data taken from Ref. [57].

shapes. The 4F MC@NLO and 5F MEPS@LO schemes succesfully model the shape of the differential distributions but consistently underestimate the production rates.

4.3 Bottom-jet associated Higgs-boson production

In this section we present predictions for b-jet(s) associated production of the Standard-Model Higgs boson in pp collisions at the 13 TeV LHC obtained in the four– and five–flavour schemes. As standard when dealing with this process, we do not include contributions from the gluon-fusion channel. However, in the 4F MC@NLO we do include terms proportional to the top-quark Yukawa coupling, contributing to order $y_b y_t$ as an interference effect at NLO QCD [3, 31, 32]. Although associated $Z+$ b-jet(s) production serves as a good proxy for the Higgs-boson case, there are important differences between both processes, mainly due to the different impact of initial-state light quarks, which couple to Z bosons but not to the Higgs boson.
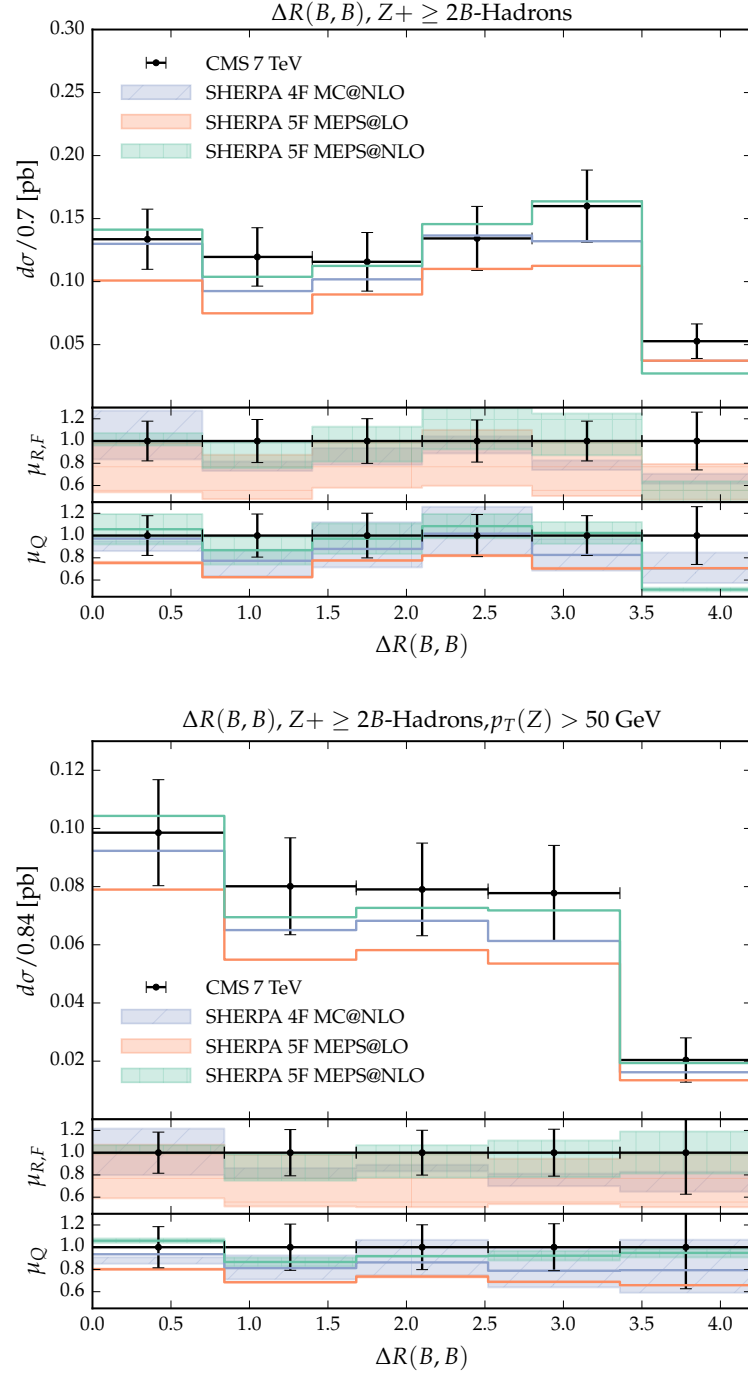
Figure 4.9: ΔR_{BB} distribution for two selections of the transverse momentum of the Z boson. Data taken from Ref. [58].

As before, QCD jets are defined through the anti-k_t algorithm using a radius parameter of $R = 0.4$, a minimal transverse momentum $p_{T,j} > 25$ GeV, and a rapidity cut of $|y_j| < 2.5$. In this case, we consider results that are at the parton
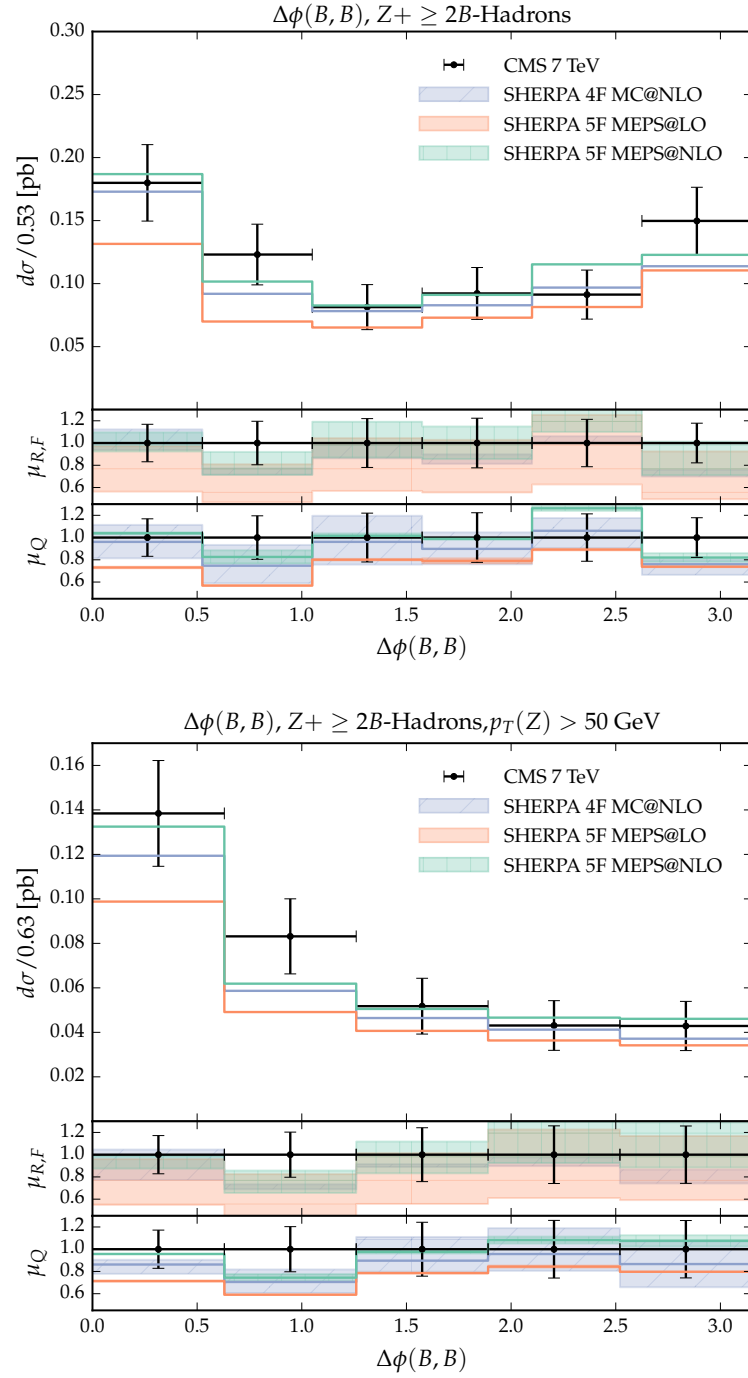
Figure 4.10: $\Delta\phi_{BB}$ distribution for two selections of the transverse momentum of the Z boson. Data taken from Ref. [58].

level only, disregarding hadronisation and underlying-event effects, which may blur the picture. We consider single b-tagged jets only, thus excluding jets with intra-jet $g \to b\bar{b}$ splittings from the parton shower which would be the same for all flavour

schemes we investigate. As for Z-boson production, we separate the event samples into categories with at least one b-jet, i.e. $H+ \geq 1b$-jet events, and at least two tagged b-jets, i.e. $H+ \geq 2b$-jets events.

LHC 13 TeV	$H+ \geq 1b$-jets [fb]	$H+ \geq 2b$-jets [fb]
$\sigma^{4F}_{\text{MC@NLO}}$	$45.2^{+15.5\%}_{-18.4\%}$	$4.5^{+25.1\%}_{-26.3\%}$
$\sigma^{5F}_{\text{MEPS@LO}}$	$79.3^{+34.0\%}_{-25.4\%}$	$3.8^{+34.3\%}_{-30.3\%}$
$\sigma^{5F}_{\text{MEPS@NLO}}$	$110.5^{+14.2\%}_{-16.0\%}$	$6.9^{+27.3\%}_{-27.1\%}$

Table 4.1: 13 TeV total cross sections and the corresponding $\mu_{F/R}$ and μ_Q uncertainties for $H+ \geq 1b$ and $H+ \geq 2b$s.

In Tab. 4.1 cross sections for the three calculations are reported. Historically, inclusive results have largely disagreed between the 4F and the 5F scheme. This feature is observed for the case at hand, too, and especially so for the case of one tagged b-jet. There the 4F MC@NLO prediction is smaller than the 5F results by factors of about 1.75 (5F LO) and of 2.44 (5F NLO). The relative differences are reduced when a second tagged b-jet is demanded. In this case we find that the 4F result lies between the two 5F results, about 20% higher than the LO predictions, and a factor of about 1.5 lower than the 5F NLO predictions. In both cases, inclusive $H + b$ and $H + bb$ production, the uncertainty bands of the two 5F predictions, corresponding to 7-point $\mu_{R/F}$ variations and μ_Q variations by a factor of two up and down, do overlap. While for the two b-jet final states this includes the 4F result, for the one b-jet case the 4F result is not compatible with the 5F predictions, taking into account the considered scale uncertainties. It is worth noting that a milder form of this relative scaling of the cross sections was already observed in the Z case.

In the case of the total inclusive cross section, this very large difference can be mitigated by including higher-order corrections, on the one hand, and a better assessment of which choice of the unphysical scales yields the better agreement [3, 34, 38, 49]. However, only a recent effort to match the two schemes [1, 2, 39, 50] has clearly assessed the relative importance of mass corrections (appearing in the 4F scheme) and large log resummation (as achieved in a 5F scheme). In particular it has been found that the difference between these two schemes is mostly given by
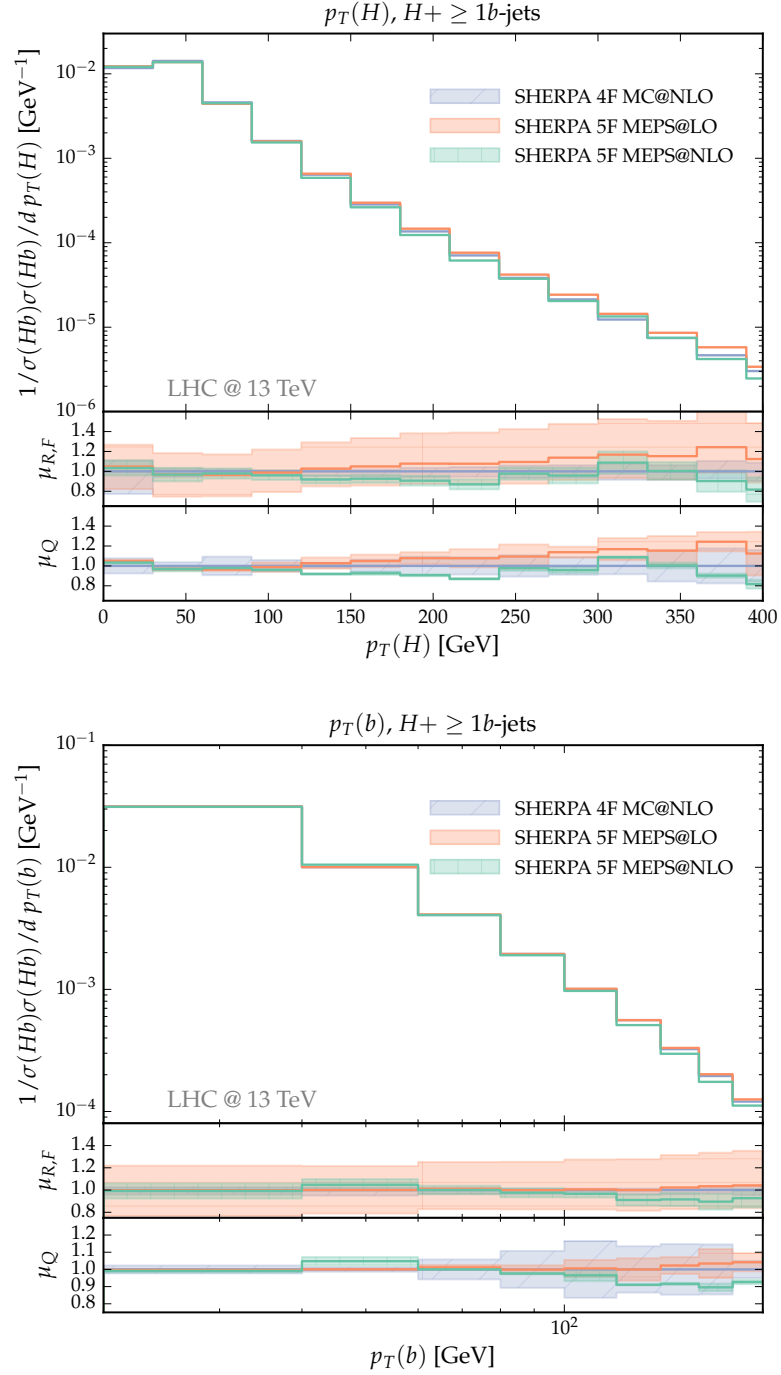
Figure 4.11: Predictions for the transverse-momentum distribution of the Higgs boson (left panel) and the leading b-jet (right panel) in inclusive $H+b$-jet production at the 13 TeV L$_{HC}$.

the resummation of large logarithms, thus suggesting that for an inclusive enough calculation either a 5F scheme or a matched scheme should be employed. This is
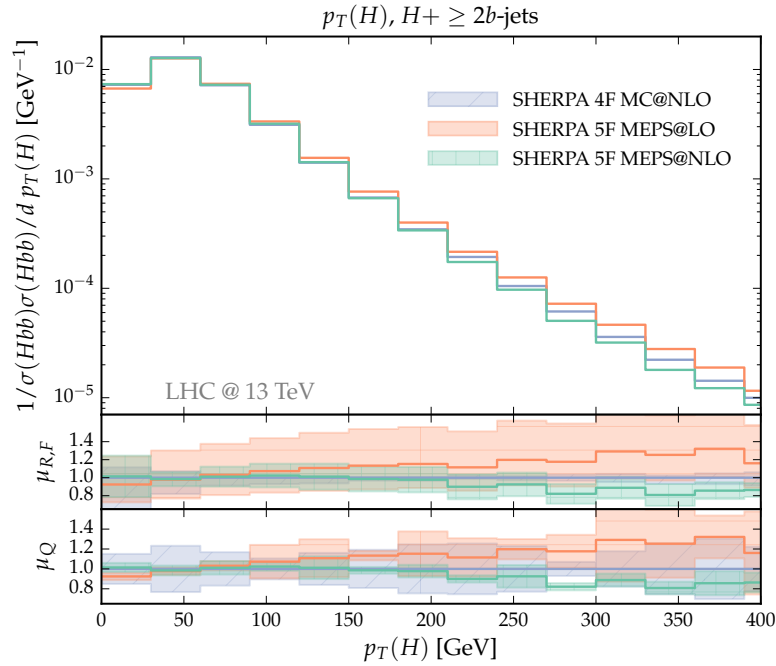
Figure 4.12: The transverse-momentum distribution of the Higgs boson in inclusive $H + 2b$-jets production at the 13 TeV LHC.

the same situation that one faces, albeit milder, in the Z case, where, in terms of normalisation the 5F scheme performed better in all cases and especially in inclusive calculations. We therefore recommend that in terms of overall normalisation, the 5F MEPS@NLO scheme should be used to obtain reliable predictions.

Let us now turn to the discussion of the relative differences in the shapes of characteristic and important distributions. To better appreciate shape differences, all differential distribution are normalised to the respective cross section, i.e. the inclusive rates $\sigma(Hb)$ and $\sigma(Hbb)$. In all cases we obtain agreement at the 15%-level or better between the 5F MEPS@NLO and 4F MC@NLO samples, the only exception, not surprisingly, being the region of phase space where the two b's come close to each other and resummation effects start playing a role. Typically, the 5F MEPS@LO predictions are also in fair agreement with the other two results, however, they exhibit a tendency for harder tails in the p_T distributions, mainly in the inclusive Higgs-boson p_T and in the transverse momentum of the second b jet.

Starting with Fig. 4.11, the transverse-momentum distributions of the Higgs
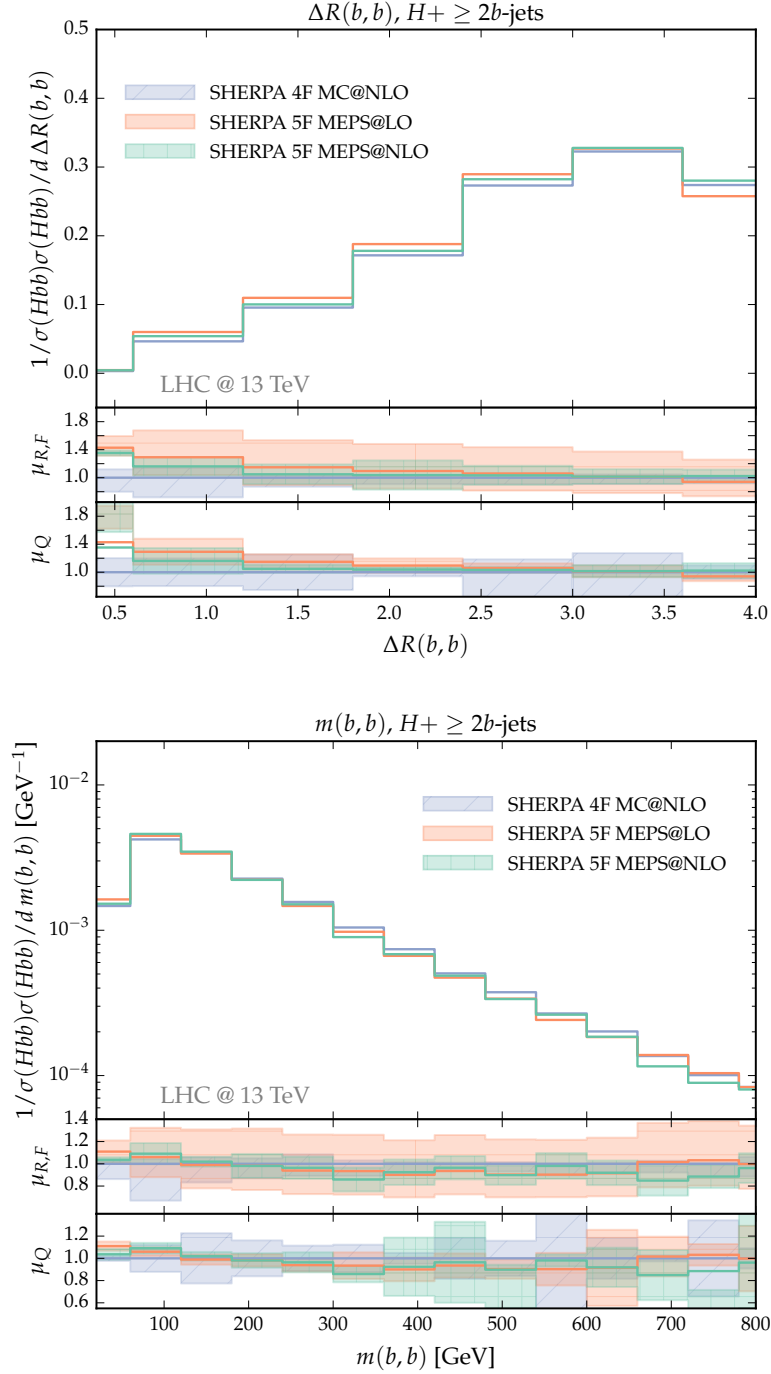
Figure 4.13: Predictions for the ΔR separation of the two leading b-jets (left panel) and their invariant-mass distribution (right panel) in inclusive $H+2b$-jets production at the 13 TeV LHC.

boson and the leading b-jet in the case of at least one b-jet tagged is displayed. Similarly to the Z example, this is the region where one would expect the 5F scheme

to perform better. However, again similarly to the Z case, the three schemes largely agree in terms of shapes, being well within scale uncertainties. Notably, this turns out to be particularly true for the low ($\sim$ 20–100 GeV) p_T region where one could have expected deviations to be the largest.

In Figs. 4.12 and 4.13 we present differential distributions for the selection of events with at least two tagged b-jets. While Fig. 4.12 shows the resulting Higgs-boson transverse-momentum distribution, Fig. 4.13 compiles results for the ΔR separation of the two leading b-jets and their invariant-mass distribution. For such two b-jets observables the 4F scheme is expected to work best, especially when the two b are well separated to suppress potentially large logarithms. However, in agreement with the Z-boson case, no significant differences between the various scheme arise when taking into account $\mu_{R/F}$ and μ_Q scale-variation uncertainties. Once again the region of low p_T in Fig. 4.12 and the region of low $m(b,b)$ in Fig. (4.13) show excellent agreement amongst the various descriptions. As anticipated, larger differences can be seen between the two 5FS and the 4F MC@NLO calculations, in the very low $\Delta R(b,b)$ and $m(b,b)$ regions, Fig. (4.13), where the two b-jets become collinear. This feature is however most likely due to the fact that we are dealing with partonic b-jets as opposed to *hadronic* ones. Taking as a reference the Z-boson case once again, in fact, where this difference is not present at all, suggests that a realistic simulation, that accounts for hadronisation effects, should largely suppress this difference.

Chapter 5

Towards a massive 5F scheme

5.1 Massive Subtraction

In previous chapters we saw how different choices in the treatment of mass effects in processes involving heavy flavours can affect theoretical predictions. While for totally inclusive predictions we can obtain matched result, for differential results we need to resort to some other methods to discriminate. In the example of a Z boson produced in association with heavy quarks, we showed how we can make use of data for this purpose. However in general this is not always possible, and to extend matching method in the context of Monte Carlo event generators is not a straightforward task.

We can start from the observation made in the two examples we studied, Z/H associated production, where we showed that the five flavour scheme generally performs better. There are, however, regions in which this might not hold true and we still need to include mass effects to properly account for those. The most natural thing to do, is to extend the 5FS to allow for massive quarks in both the initial and final state. The idea then is that this 5F Massive Scheme (5FMS), will have massive b-quarks that contribute both to the running of the coupling constant and to the evolution of PDFs.

To extend the 5F scheme to account for massive bs in the final state is conceptually easy, although practically difficult, as we would end up having two different type of b quarks, which might lead to inconsistencies. Therefore we need to extend

the methods and techniques developed for the massless five flavour scheme to allow for massive initial state particles. Further we wish to retain the current fixed order accuracy of the 5F scheme in Monte Carlo, namely the next to leading order.

In order to extend Catani-Seymour formalism to massive initial state particle, it is necessary to work out the correspondent form of $\mathbf{V}^{ak,b}(p_a, p_b, p_k)$ in the case particles a, b are both massive. This has been performed in [18] in the context of fermions in QED in four dimensions, so we can make use of results reported there and promote them to QCD and $d = 4 - 2\varepsilon$ dimensions, by performing a simple replacement:

$$e^2 Q_a \sigma_a Q_b \sigma_b \to 4\pi \alpha_S \mu^{2\varepsilon} \mathbf{T}_a \cdot \mathbf{T}_b. \tag{5.1}$$

We further have to define the phase space mapping that defines $\widetilde{p}_i$ in Eq. (2.20), and which is further needed to compute the one particle phase space, Φ_1.

5.1.1 Initial state splitter with initial state spectator

We start by reporting some useful definitions that are used throughout,

$$s = (p_a + p_b)^2; \quad s_{ab} = s - m_a^2 - m_b^2; \tag{5.2}$$

$$Q^2 = (p_a + p_b - p_k)^2 = s - 2(p_a + p_b) \cdot p_k; \tag{5.3}$$

$$x_{ab} = 1 - 2\frac{(p_a + p_b) \cdot p_k}{s_{ab}}; \tag{5.4}$$

$$y_a = 2\frac{p_a \cdot p_k}{s_{ab}}; \tag{5.5}$$

$$\lambda_{ab} = \lambda(s, m_a^2, m_b^2); \quad \lambda(a, b, c) = a^2 + b^2 + c^2 - 2(ab + bc) - 2ac. \tag{5.6}$$

We define the contribution to the subtraction term, $\mathbf{V}^{ak,b}(p_a, p_b, p_k)$:

$$\mathbf{V}^{q_a g_k, b}(p_a, p_b, p_k) = 8\pi \mu^{2\varepsilon} \alpha_s C_F \left[\frac{2}{1 - x_{ab}} - (1 + x_{ab}) - \varepsilon(1 - x_{ab}) - \frac{x_{ab} m_a^2}{p_a \cdot p_k} \right] \tag{5.7}$$

in the case where the splitting is $b \to gb$. In any other case we do not have any singular contribution, so we do not need any subtraction term[1]. The necessary

---

[1] Although strictly speaking this is true, these additional contributions will still be proportional to $\log m_b^2/Q^2$, where Q is some scale. For the example we discuss in this chapter, we checked that this contribution are stable under variations of the parameter m_b.

phase space mappings have to preserve the mass shell, and it is customary to keep the momentum p_b fixed. As a result all other momenta p_j are shifted as well as the total momentum $Q = \sum_j p_j$. The transformations are given by,

$$\widetilde{p}_a^\mu = \sqrt{\frac{\lambda\left(Q^2, m_a^2, m_b^2\right)}{\lambda_{ab}}}\left(p_a^\mu - \frac{s_{ab}}{2\,m_b^2}p_b^\mu\right) + \frac{Q^2 - m_a^2 - m_b^2}{2\,m_b^2}p_b^\mu ; \quad \widetilde{Q}^\mu = \widetilde{p}_a^\mu + p_b^\mu . \quad (5.8)$$

It is straightforward to check that these relations fulfill the mass-shell conditions, such that $\widetilde{p}_a^2 = m_a^2$ and $\widetilde{Q}^2 = Q^2$, and that they possess the right infra-red and collinear asymptotic limits. All other momenta, including those of non coloured particles, transform as $\widetilde{p}_i^\mu = \Lambda_\nu^\mu\,p_i^\nu$ where

$$\Lambda_\nu^\mu = g_\nu^\mu - \frac{(Q + \widetilde{Q})^\mu(Q + \widetilde{Q})_\nu}{Q^2 + Q \cdot \widetilde{Q}} + \frac{2\,\widetilde{Q}^\mu Q_\nu}{Q^2} \quad (5.9)$$

We further need to calculate the extra-emission phase space. In particular, we have

$$\int \mathrm{d}\Phi_{N+1}(p_k, Q; p_a + p_b) = \int_0^1 \mathrm{d}x \int \mathrm{d}\Phi_N(\widetilde{Q}(x); \widetilde{p}_a(x) + p_b) \int \left[\mathrm{d}^{d-1}p_k(s, x, y_a)\right] , \quad (5.10)$$

where x dependent momenta can be obtained from $\widetilde{p}_a$ and $\widetilde{Q}$ upon replacing $Q^2 \to s_{ab}\,x + m_a^2 + m_b^2$.

The explicit calculation of $\int \left[\mathrm{d}^{d-1}p_k(s, x, y_a)\right]$ can be found in Appendix C. the final result yields

$$\int \left[\mathrm{d}^{d-1}p_k(s, x, y_a)\right] = \frac{1}{16\,\pi^2}\frac{(4\pi)^\varepsilon}{\Gamma(1-\varepsilon)}\left(\frac{s_{ab}}{\sqrt{\lambda_{ab}}}\right)^{1-2\varepsilon}(1-x)^{1-2\varepsilon}\,s_{ab}\,s^{-\varepsilon}$$
$$\int_{v_2}^{v_1}\mathrm{d}v[(v_1 - v)\,(v - v_2)]^{-\varepsilon}, \quad (5.11)$$

where we performed a change of variable $y_a = v\,(1-x)$, and

$$v_{1,2} = \frac{s_{ab} + 2\,m_a^2 \mp \lambda_{ab}}{2\,s} . \quad (5.12)$$

We can thus define the integral of the splitting function $\mathbf{V}^{ak,b}$, which defines the x-distribution $\widetilde{\mathcal{V}}^{a,b}$. We start by expressing Eq. (5.7) in terms of the new variable v and the splitting variable x,

$$\frac{\alpha_s\,C_F}{2\,\pi}\widetilde{\mathcal{V}}^{a,b}(x; \varepsilon) = \int \left[\mathrm{d}^{d-1}p_k(s, x, y_a)\right]\frac{1}{2p_a \cdot p_k}\mathbf{V}^{ak,b} . \quad (5.13)$$

where, collecting an overall factor of $(1-x)^{-2}$ from $\mathbf{V}^{ak,b}$, and putting everything together with Eq. (C.10), we get

$$
\widetilde{\mathcal{V}}^{a,b}(x;\varepsilon) = \frac{1}{\Gamma(1-\varepsilon)} \left(\frac{4\pi\mu^2}{s}\right)^{\varepsilon} \left(\frac{s_{ab}}{\sqrt{\lambda_{ab}}}\right)^{1-2\varepsilon} (1-x)^{-1-2\varepsilon}
$$
$$
\int_{v_2}^{v_1} \frac{\mathrm{d}v}{v} \left[(v_1-v)\,(v-v_2)\right]^{-\varepsilon} \left[1+x^2-\varepsilon\,(1-x)^2 - \frac{2\,x\,m_a^2}{s_{ab}\,v}\right]. \quad (5.14)
$$

The distribution $(1-x)^{-1-2\varepsilon}$ is divergent in the double limit $x,\varepsilon \to 0$. To make it regular at this end-point, we introduce the plus prescription, such that:

$$
(1-x)^{-1-2\varepsilon} = -\frac{\delta(1-x)}{2\varepsilon} + \frac{1}{(1-x)_+} + \mathcal{O}(\varepsilon). \quad (5.15)
$$

As a consequence, we can re-express $\widetilde{\mathcal{V}}^{a,b}(x;\varepsilon)$ as

$$
\widetilde{\mathcal{V}}^{a,b}(x;\varepsilon) = \delta(1-x)\,\mathcal{V}^{a,b}(\varepsilon) + \left[K^{a,b}(x)\right]_+. \quad (5.16)
$$

The function $K^{a,b}(x)$ corresponds to the v integral, finite part, of the ε expansion of Eq. (5.14), and is given by

$$
K^{a,b}(x) = -\frac{s_{ab}}{\sqrt{\lambda_{ab}}} \left(\frac{1+x^2}{1-x}\right) \log\beta_0 - 2\,x\,; \quad (5.17)
$$

while the end-point contribution

$$
\mathcal{V}^{a,b}(\varepsilon) = \frac{1 + \frac{s_{ab}}{\sqrt{\lambda_{ab}}}\log\beta_0}{\varepsilon} + \log\left(\frac{\mu^2\,s}{s_{ab}^2}\right) + \frac{3}{2}
$$
$$
+ \frac{s_{ab}}{\sqrt{\lambda_{ab}}} \left\{ \left[\log\left(\frac{\mu^2\,\lambda_{ab}}{m_a^2 s_{ab}^2}\right) + \left(\frac{1}{2} - \frac{2\,m_a^2}{s_{ab}}\right)\right] \log\beta_0 + 2\,\mathrm{Li}_2(\beta_0) + \frac{1}{2}\log^2\beta_0 - \frac{\pi^2}{3} \right\},
$$
$$
(5.18)
$$

where

$$
\beta_0 \equiv \frac{v_1}{v_2} = \frac{s_{ab} + 2\,m_a^2 - \lambda_{ab}}{s_{ab} + 2\,m_a^2 + \lambda_{ab}}. \quad (5.19)
$$

The contribution to the partonic differential cross section is thus given by

$$
\int \mathrm{d}\Phi_1\,\mathcal{S} = \frac{\alpha_s\,C_F}{2\,\pi} \left\{ \mathcal{V}^{a,b}(\varepsilon)\,\mathrm{d}\hat{\sigma}_N(s_{ab}) \right.
$$
$$
\left. + \int_0^1 \mathrm{d}x\,K^{a,b}(x) \left[\frac{\phi(x\,s_{ab})}{x\,\phi(s_{ab})}\mathrm{d}\Phi_N\,\mathcal{B}_N(x\,s_{ab}) - \mathrm{d}\Phi_N\,\mathcal{B}_N(s_{ab})\right] \right\}, \quad (5.20)
$$

where we make explicit the dependence on the is the initial state flux, ϕ.

5.1.2 The case of initial state hadrons

So far we have only dealt with partonic observables, we now investigate the case of initial state hadrons. Firstly, in the hadronic centre of mass, the hadron's momenta are parametrised as

$$P_{1,2} = \frac{\sqrt{S}}{2} \, (1,0,0,\pm 1) \, , \tag{5.21}$$

where $\sqrt{S}$ is the hadronic centre of mass energy. While the parton's momenta in this frame are given by

$$p_{a,b} = \eta_{1,2} \, P_{1,2} + \frac{m_{a,b}^2}{\eta_{1,2} \, S} \, P_{2,1} \, ; \tag{5.22}$$

where

$$\eta_{1,2} \in \left[\frac{1}{2} \left(1 - \sqrt{1 - \frac{4 \, m_a^2 m_b^2}{S^2}} \right) , \frac{1}{2} \left(1 + \sqrt{1 - \frac{4 \, m_a^2 m_b^2}{S^2}} \right) \right] \tag{5.23}$$

The partonic centre of mass energy can be written as

$$s = (p_a + p_b)^2 = s_{ab} + m_a^2 + m_b^2; \quad s_{ab} = 2 \, \eta_1 \, \eta_2 \, S + \frac{m_a^2 m_b^2}{\eta_1 \, \eta_2 \, S} \, , \tag{5.24}$$

and the initial state flux

$$\phi(s_{ab}) = 4 \, \sqrt{\lambda(s, m_a^2, m_b^2)} \, . \tag{5.25}$$

We can thus write the hadronic correspondent of Eq. (5.20),

$$
\mathcal{I} = \frac{\alpha_s \, C_F}{2 \, \pi} \iint \mathrm{d}\eta_1 \, \mathrm{d}\eta_2 \, f_a(\eta_1) \, f_b(\eta_2) \left\{ \mathcal{V}^{a,b}(\varepsilon) \, \mathrm{d}\hat{\sigma}_N(s_{ab}) \right.
$$
$$
\left. + \int_0^1 \mathrm{d}x \, K^{a,b}(x) \left[\frac{\phi(x \, s_{ab})}{x \, \phi(s_{ab})} \mathrm{d}\Phi_N \, \mathcal{B}_N(x \, s_{ab}) - \mathrm{d}\Phi_N \, \mathcal{B}_N(s_{ab}) \right] \right\} . \tag{5.26}
$$

The problem with this formula, as it is, is that it requires to evaluate the partonic cross section with many different momenta configuration, for each value of x, as well as at $x = 1$. This is not only inconvenient but inefficient, too, and can be solved by means of a change of variable.

Consider the integral

$$\iint \mathrm{d}\eta_1 \, \mathrm{d}\eta_2 \, f_a(\eta_1) \, f_b(\eta_2) \int_0^1 \mathrm{d}x \, K^{a,b}(x) \frac{\phi(x \, s_{ab})}{x \, \phi(s_{ab})} \mathrm{d}\Phi_N \, \mathcal{B}_N(x \, s_{ab}) \, , \tag{5.27}$$

we start by defining a change of variable such that:

$$x\, s_{ab}(\eta_1, \eta_2) = s_{ab}(\eta_1'(x), \eta_2'), \tag{5.28}$$

$$\eta_2' = \eta_2\,. \tag{5.29}$$

This transformation defines a Jacobian, $\mathcal{J}(\eta_1'(x), \eta_2)$, such that

$$\mathrm{d}\eta_1 \mathrm{d}\eta_2 \mathrm{d}x = \mathrm{d}\eta_1' \mathrm{d}\eta_2 \mathrm{d}x \, \mathcal{J}(\eta_1'(x), \eta_2)\,. \tag{5.30}$$

More details on this transformation are resorted in Appendix C. After reversing the integration order, and performing the change of variable, Eq. (5.27) becomes

$$\iint \mathrm{d}\eta_1'\, \mathrm{d}\eta_2\, f_a(\eta_1')\, f_b(\eta_2) \mathrm{d}\Phi_N\, \mathcal{B}_N(s_{ab}) \int_{\eta_1}^1 \mathrm{d}x\, K^{a,b}(x) \left[\mathcal{J}(\eta_1, \eta_2) \frac{\phi(s_{ab})}{x\,\phi(s_{ab}(\eta_1))} \frac{f_a(\eta_1)}{f_a(\eta_1')} \right] \tag{5.31}$$

where $\eta_1 = \eta_1(\eta_1', x)$, is the old variable expressed in terms of the new ones. Note also the s_{ab} is now expressed in terms of the new variables, where not explicitly stated. We can now re-name $\eta_1 \leftrightarrow \eta_1'$ in Eq. (5.31) and combine it with Eq. (5.26),

$$\mathcal{I} = \frac{\alpha_s\, C_F}{2\,\pi} \iint \mathrm{d}\eta_1\, \mathrm{d}\eta_2\, f_a(\eta_1)\, f_b(\eta_2)\, \mathrm{d}\Phi_N\, \mathcal{B}_N(s_{ab}) \left\{ \mathcal{V}^{a,b}(\varepsilon) \right.$$
$$\left. + \int_{\eta_1}^1 \mathrm{d}x\, K^{a,b}(x) \left[\mathcal{J}(\eta_1', \eta_2) \frac{\phi(s_{ab})}{x\,\phi(s_{ab}(\eta_1'))} \frac{f_a(\eta_1')}{f_a(\eta_1)} - 1 \right] - \int_0^{\eta_1} \mathrm{d}x\, K^{a,b}(x) \right\}, \tag{5.32}$$

which is our final formula[2]. The main advantage of having performed this transformation is that now the whole curly bracket in Eq. (5.32) acts as a local K-factor on top of the partonic cross section, which is now evaluated only once per phase-space point.

5.2   Massive dipole formulae for other configurations

The steps presented in the previous sections can be straightforwardly applied to the case of *initial-final* configuration. Any other case is already covered by the original extension to massive particles of the Catani-Seymour method [16]. The idea is to

---

[2]In the term $\int_0^{\eta_1} \mathrm{d}x\, K^{a,b}(x)$ we use a shorthand notation. The upper integration bound, in fact, is not exactly η_1, although that is its massless limits. The correct value is that obtained by inverting Eq. (C.25) with respect to η_1' and evaluating it for $\eta_1 = 0$.

take the relevant formulae from [18] and to transform them in the same way as it is shown for *initial-initial* case. As all the relevant equations are presented there, and we do not use these cases in the examples presented in this work, we do not repeat them here.

We conclude this part presenting the modifications to [18] that are needed in order to perform the extension. As we already mentioned, the first, overall, replacement is given by

$$e^2 \, Q_a \, \sigma_a \, Q_b \, \sigma_b \to 4 \, \pi \, \alpha_S \, \mu^{2\varepsilon} \, \mathbf{T}_a \cdot \mathbf{T}_b \,. \tag{5.33}$$

The only other necessary modification to obtain the corresponding version of Eq. (5.18), is replacing, in Eq.(4.34) of [18], the mass of the photon, m_γ, with

$$\log m_\gamma^2 = \frac{1}{\varepsilon} + \log \mu_R^2 + \mathcal{O}(\varepsilon) \,. \tag{5.34}$$

With these modifications and the method described in the previous section, we obtain the relevant IF contributions in the case of massive initial state quarks.

5.3 Validation: bottom quark fusion with massive quarks

To see how the 5F massive scheme (or 5FSM) works we now present an explicit example: the production of a Higgs boson through bottom quark fusion. There are two important features about this example. Firstly, as we discuss in Chapter 3, we know how to include exact mass effects up to order α_s^3 through matching. From that calculation we get that mass corrections to the total inclusive cross section are quite small. Consequently we expect the 5FSM too to yield a marginally different total cross section. Secondly, this example has a easy enough structure that most formulae can be reported in closed analytic form.

We start by showing how the massive subtraction removes all divergences at the integrand level, and we compare results obtained in the vanilla 5FS against the fully massive 5FSM. The leading order colour summed, helicity averaged and squared matrix element for Higgs production in bottom fusion is given by

$$|\overline{\mathcal{M}}_{b\bar{b}\to H}|^2 = \frac{g_{hb\bar{b}}^2}{6} \left(m_H^2 - 4 \, m_b^2 \right) \,, \tag{5.35}$$

where $g_{hb\bar{b}}$ is the bottom Yukawa coupling, such that

$$g_{hb\bar{b}} = \frac{m_b}{v} \,, \tag{5.36}$$

and v is the electroweak vacuum expectation value.

The matrix element corresponding to the emission of an extra gluon from the initial state b has the form

$$\mathcal{R} = |\overline{\mathcal{M}}_{b\bar{b}\to Hg}|^2 = \frac{\alpha_s \, C_F \, 8\,\pi \, g_{hb\bar{b}}^2}{6}$$
$$\left\{ (m_H^2 - 4\,m_b^2) \left[\frac{2(s - 2\,m_b^2)}{(m_b^2 - t)(m_b^2 - u)} - \frac{2\,m_b^2}{(m_b^2 - t)^2} - \frac{2\,m_b^2}{(m_b^2 - u)^2} \right] \right.$$
$$\left. + (s - m_h^2) \left[\frac{1}{m_b^2 - t} + \frac{1}{m_b^2 - u} \right] \right\} . \tag{5.37}$$

We firstly show that indeed $|\overline{\mathcal{M}}_{b\bar{b}\to Hg}|^2 - \mathcal{D}^{ak,b} - \mathcal{D}^{ak,b}$ gives a finite number. Putting everything together and expressing $\mathcal{R}$ in Eq. (5.37) in terms of splitting kinematics variables x, y and Q^2 we get

$$\mathcal{R} - \mathcal{D}^{ak,b} - \mathcal{D}^{ak,b} = \frac{8\,\pi}{3} \alpha_s \, C_F \, g_{hb\bar{b}}^2 \frac{m_b^2}{s_{ab}} \frac{1 - x}{x\,y\,(1 - x - y)} \,, \tag{5.38}$$

where we make use of

$$s = \frac{m_h^2 - 2\,m_b^2(1 - x)}{x} \,,$$
$$t = -\frac{m_h^2(1 - x - y) - 2\,m_b^2(2 - x - 2\,y)}{x} \,,$$
$$u = -\frac{y\,m_h^2 - 2\,m_b^2(x + 2\,y)}{x} \,. \tag{5.39}$$

The soft limit is approached for $x \to 1$, and it is straight forward to check that, in this limit, Eq. (5.38) is not only finite, but exactly zero.

Although the collinear limit, strictly speaking, does not exist if the mass of the parton remains non zero, we can check that the quasi-collinear is finite. To phrase this slightly differently we need to check that when $p_a \cdot p_k$ (or y) approaches zero as m_b, Eq. (5.38) remains finite. Again this is quite straightforward to see, and in this limit we get exactly zero.

We now turn to the one loop contribution. At order α_s, we have that

$$\mathcal{V} = 2\,\mathrm{Re}(\delta_g)\,|\overline{\mathcal{M}}_{b\bar{b}\to H}|^2 \tag{5.40}$$

Figure 5.1: Contributions to the born phase space of $b\bar{b} \rightarrow H$.

Figure 5.2: Contributions to the real emission phase space of $b\bar{b} \to Hg$ Eq. (5.37) and $bg \to Hb$.

where

$$
\mathrm{Re}(\delta_g) = -\frac{\alpha_s\,C_F}{2\,\pi} \left\{ \frac{1 + \frac{s_{ab}}{\sqrt{\lambda_{ab}}} \log \beta_0}{\varepsilon} + 1 + \log \frac{\mu^2}{m_b^2} + \frac{1-\beta^2}{\beta^2} \log \beta_0 \right.
$$
$$
\left. - \frac{s_{ab}}{\sqrt{\lambda_{ab}}} \left[-\log \frac{\mu^2}{m_b^2} \log \beta_0 - 2\,\mathrm{Li}_2\left(1 - \beta_0\right) - \frac{1}{2}\,\log^2 \beta_0 + \pi^2 \right] \right\}, \quad (5.41)
$$

with

$$
\beta = \sqrt{1 - \frac{4\,m_b^2}{m_H^2}}\,; \quad \beta_0 = \frac{1-\beta}{1+\beta}\,. \tag{5.42}
$$

Using Eq. (5.20) it is straightforward to see that indeed

$$
\mathcal{V} + \int \mathrm{d}\Phi_1\,\mathcal{S} = \mathcal{O}(\varepsilon^0)\,, \tag{5.43}
$$

which in turn, combined with Eq. (5.38), yields that Eq. (2.14) is completely free of singularities.

5.3.1 Factorisation of collinear singularities

We now turn to how the inclusion of mass effects affects the collinear limit, and, therefore, the definition of PDFs. Our goal here is not a precise and consistent discussion about the factorisation of collinear singularities in the presence of massive initial state quarks, as this is beyond the scope of this work. Nevertheless it is interesting to highlight the structure of mass correction, especially in the presence of parton densities that have been obtained in a matched scheme.

In the standard case of massless initial state partons, Eq. (5.38) would be exactly zero. This is due to the fact the only term appearing in the real emission matrix element is also the leading log that gets factorised into the b-pdf and resummed through Altarelli-Parisi equations, Eq. (2.3). The reason is that, in the massless case, this process has only two scales m_H and some dimensional regulator that introduces a scale μ_F that separates the divergent and finite part. This means that we can symbolically write

$$
\int \mathrm{d}\Phi_2\,\mathcal{R}(m_b = 0) \propto A \log \frac{m_H^2}{\mu_F^2}\,. \tag{5.44}
$$

In the case of massive initial state particle we have an additional physical scale, m_b. This scale now regulates collinear divergences, we no longer need to introduce a

collinear regulator related to the scale μ_F. However we can in practice still introduce the scale μ_F, such that

$$\int \mathrm{d}\Phi_2 \mathcal{R}(m_b \neq 0) \propto A\left(\frac{m_b^2}{m_H^2}, \frac{m_b^2}{\mu_F^2}\right) \log \frac{m_H}{\mu_F^2} + B\left(\frac{m_b^2}{m_H^2}, \frac{m_b^2}{\mu_F^2}\right) \log \frac{m_H}{m_b^2} + \mathcal{O}\left(\frac{m_b^2}{m_H^2}, \frac{m_b^2}{\mu_F^2}\right), \tag{5.45}$$

where we define A and B, such that

$$\lim_{m_b \to 0} A\left(\frac{m_b^2}{m_H^2}, \frac{m_b^2}{\mu_F^2}\right) = A, \tag{5.46}$$

$$\lim_{m_b \to 0} B\left(\frac{m_b^2}{m_H^2}, \frac{m_b^2}{\mu_F^2}\right) = 0, \tag{5.47}$$

and by $\mathcal{O}\left(\frac{m_b^2}{m_H^2}, \frac{m_b^2}{\mu_F^2}\right)$, we mean terms that are only given by powers of the two ratios. In this way we separate terms that appears also in the massless case, and get modified by power suppressed terms in the massive case, and new terms that arise only when the massive case is considered.

As in the massless case the function A is proportional to the Altarelli-Parisi splitting function P_{qq}, by extension we can define the massive A function to be proportional to the massive P_{qq}, which in turn is proportional to $\mathbf{V}^{qg,q}$ of Eq. (5.7). This means that this term corresponds to the term that would be absorbed into the parton densities in the massive case at leading twist. However, PDFs are generally given in schemes that account for some mass effects at fixed-order by means of some matching method, like FONLL [29], ACOT [82], or TR [83,84]. Mass effects included in these schemes coincide up to higher order effects and it is easy to see that the order considered in this work they have the same functional form of the function A.

The B function appearing in Eq. (5.45) is just made up of terms that are proportional to m_b^2. These terms are clearly non divergent, and in principle it is not necessary to absorb them into an initial state radiation term. However, some of these terms might be universal and could definitely be accounted for by higher twist contributions to the QCD factorisation formulae as well as with the introduction of an intrinsic (or static) bottom-quark component in the proton. Although these terms might in principle spoil factorisation, we can make sure that they are indeed suppressed, as we expect from Eq. (2.1).

Subtracting the A part of Eq. (5.45), corresponds to Eq. (5.38)

$$\int \mathrm{d}\Phi_2 \left[\mathcal{R}(m_b \neq 0) - \mathcal{S} \right] \propto B \left(\frac{m_b^2}{m_H^2}, \frac{m_b^2}{\mu_F^2} \right) \log \frac{m_H^2}{m_b^2} + \mathcal{O}\left(\frac{m_b^2}{m_H^2}, \frac{m_b^2}{\mu_F^2} \right) , \qquad (5.48)$$

which we know from the previous section being exactly zero in the soft and collinear limit. Further, when it is not zero, it is proportional to $m_b^2/s_{ab} \sim 1 \times 10^{-3}$ which makes it very suppressed [3]. We conclude that we can safely make use of standard PDF sets that have been matched to include mass effects to obtain reliable predictions at the NLO in the five flavour massive scheme.

5.4   Simulations for $b\bar{b} \to H$ with massive quarks, fixed-order

We now show results obtained for $b\bar{b} \to H$ in the five-flavour massive scheme at next-to-leading fixed-order accuracy. Predictions with massive initial state quarks are obtained by implementing the massive subtraction as presented in Section 5.1 within the SHERPA event generator [85].

Leading order matrix elements, including those of real radiation processes, are calculated using the AMEGIC++ [60] matrix element generator. The differential subtraction follows closely that presented in [70] with the ingredients reported in Section 5.1. Integrated subtraction terms are implemented in SHERPA using Eq. (5.26), and this implementation will be made public in a future SHERPA release. Virtual corrections are obtained from the OPENLOOPS generator [67].

While no cuts at the generation level are applied, in the following results we define b-jet any jet with $p_T \geq 25$ GeV that has at least one b-flavoured parton in it. We further require any particle in the final state to have $|\eta| \leq 2.5$. We generate only fixed-order events at this stage, *i.e.* no parton shower effects are accounted.

In order to study the impact of the inclusion of mass effects, we compare the five flavour massive scheme (5FMS) with the vanilla five flavour scheme, where b are massless,

---

[3]Numerically we see that at the level of total cross section, Eq. (5.38) corresponds to roughly 0.001% of the Born cross section, which is comparable with the error from Monte Carlo integration.
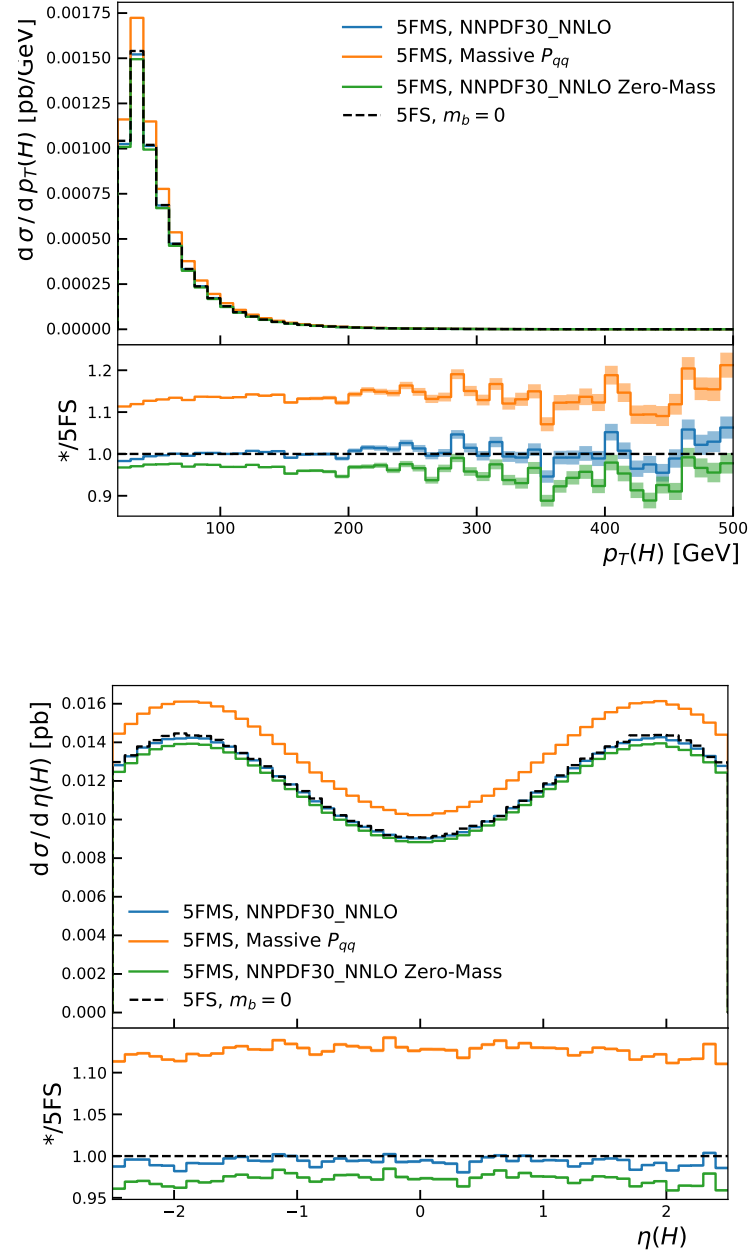
Figure 5.3: The p_T and η spectrum of the Higgs boson at NLO. We compare the vanilla 5FS, and the 5FMS matched with three different PDF sets. More details in the text.
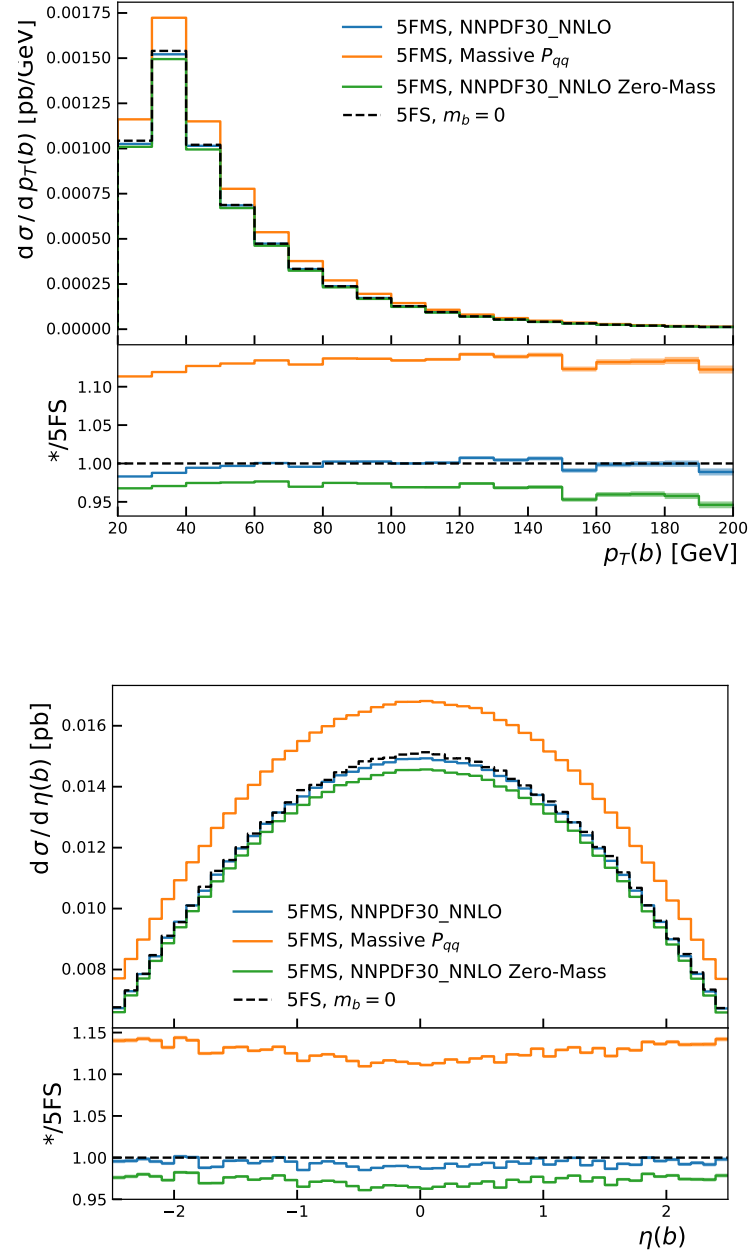
Figure 5.4: The p_T and η spectrum of the b-jet. We compare the vanilla 5FS, and the 5FMS matched with three different PDF sets. More details in the text.

We further consider matching the 5FMS partonic cross section to three different PDF sets. The first choice is, as we discuss in the previous section, to use a standard GM-VFNS evolved PDF set. As these sets include mass effects at a fixed order accuracy, higher than the one considered in this example, we claim that they provide a consistent result, up to a negligible effect. In particular, we choose the default PDF set in SHERPA, namely the NNPDF30 set evolved at NNLO with $\alpha_s(m_Z) = 0.118$ [41]. Mass corrections in this PDF set are obtained through FONLL-C [29] matching and are included up to $\mathcal{O}(\alpha_s^2)$. To show the importance of such mass effects in PDFs, we compare against the same PDF set re-evolved at NNLO, but in a ZM-VFNS. This means that no mass effects are accounted other than threshold effects, and massless splitting kernels are used to determine the evolution operator. The last set we compare against, is a PDF set where the evolution of the b PDF is obtained solving Eq. (2.3) at leading order, and replacing the standard Altarelli-Parisi splitting function, P_{qq}, with the splitting kernel of Eq. (5.7),

$$f_b^{\text{Massive } P_{qq}}(x, Q^2) = \frac{\alpha_s}{2\pi} \log \frac{Q^2}{m_b^2} \int_x^1 \frac{\mathrm{d}z}{z} \left[\frac{1+z}{1-z} - \frac{2\,z\,m_b^2}{Q^2\,(1-z)} \right]_+ f_b\left(\frac{x}{z}, Q^2\right)$$
$$+ P_{qg}^{(0)}(z)\, f_g\left(\frac{x}{z}, Q^2\right) + \mathcal{O}(\alpha_s^2)\,. \quad (5.49)$$

These PDF sets are obtained using the APFEL [86] evolution library.

We report results in Figs. 5.3, 5.4 for the p_T and η spectra of the Higgs boson and the b-jet respectively.

By definition, and by the conclusions laid out in the previous chapters, we expect mass effects to play a marginal, order $\sim 1-5\%$, effects at the level of total cross sections. Further, as they are power suppressed, we expect them to be less important at large p_T, while having the largest impact in the lower bins of the distribution. This is due to the fact that the difference in the mass treatment between the two scheme is only in the hard matrix elements. Consequently, as pictured in Fig. 5.3, for example, we see that the 5FMS obtained with the standard PDF set, blue solid line, somehow starts a few percent off of the massless 5FS, black dashed line, while they consistently overlap for $p_T(H, b) \gtrsim 50$ GeV.

We now turn to the comparison with the PDF set evolved in the zero mass variable flavour number scheme (ZM-VFNS). The difference between the 5FMS in

this set up, green solid line, and the massless 5FS, is that in the former mass effects are included in the hard matrix elements, while some are included in the PDF in the latter. Therefore, on top of the power suppressed terms there are other terms coming from the matching. These terms include constant terms, *i.e.* independent of m_b, as it can be seen in Figs. 5.3, 5.4, where the difference between the ZM-VFNS and the standard 5FMS result in a constant shift of a few percent.

Our final reference is a five flavour massive scheme obtained with a PDF set evolved with a massive splitting function at the leading order, red solid line. We firstly notice that a direct comparison with a standard parton density set is somehow bugged by the fact the mass effects are included at different orders in the two PDF sets. In addition the evolution operator is used at two different orders. As a consequence the size of mass effects is not necessarily truthful. However it is interesting to see that this scheme behaves with respect to the ZM-VFNS 5FMS, in roughly the same way as the 5FMS with standard PDFs behaves with respect to the vanilla 5FS. The only difference is that we see an overall constant factor of about 10-15%, which is due to the different evolution and mass effects accuracy.

We now briefly discuss the pseudo rapidity spectrum. In this case all schemes differ by one another by a somehow constant amount. This follows from the fact that pseudo rapidity is a dimensionless variable, and as such does not introduce any scale to make mass effects less or more important in any region. We thus naturally expect mass effects to be roughly of the same order as that seen in the case of the total cross section. This fact can be seen explicitly in Figs. 5.3, 5.4.

We conclude that fixed order mass effects for this process are generally quite small, both at the inclusive and differential level. We find that when they are important they generally do not exceed a few percent. On the other hand, this might not hold true for all processes involving heavy quarks. As such, the five flavour massive scheme provides a useful and consistent scheme to produce fully differential results including mass effects.

5.5 Massive initial state shower

In this last section we provide the necessary ingredients to promote the five flavour massive scheme we presented in previous sections to MC@NLO accuracy.

The MC@NLO matching combines the fixed order accuracy given by matrix elements, in this case the next to leading order, with the resummation performed by the parton shower. The main formula for a MC@NLO matched observable is given by

$$
d\sigma^{\text{MC@NLO}} = d\Phi_N \, \overline{\mathcal{B}}(\Phi_N) \left[\Delta_N(t_0, \mu_Q^2) + \int_{t \in [t_0, \mu_Q^2]} d\Phi_1 \, K_N(\Phi_1) \, \Delta_N(t(\Phi_1), \mu_Q^2) \right]
$$
$$
+ \, d\Phi_{N+1} \, \mathcal{H}(\Phi_{N+1}) \,. \quad (5.50)
$$

The only modifications needed in the case of the 5FMS, compared to what is described in section 2.4, are in which splitting kernels are taken in the Sudakov form factor, the extra emission phase space, and the relevant phase space mappings. All of these ingredients can be read off from section **??**, with the additional semplification that in this case we only need the $d \to 4$ limit of the expressions presented there. We start by taking the phase-space formula for one extra emission,

$$
\int \left[d^3 p_k(s, x, y_a) \right] = \frac{1}{16 \, \pi^2} \left(\frac{s_{ab}^2}{\sqrt{\lambda_{ab}}} \right) \int_{y_2(x)}^{y_1(x)} dy \,, \quad (5.51)
$$

where

$$
y_{1,2}(x) = (1 - x) \, \frac{s_{ab} \, + \, 2 \, m_a^2 \, \mp \, \lambda_{ab}}{2 \, s} \,. \quad (5.52)
$$

This would in principle be enough, however the actual variable the shower algorithm generates is the $k_\perp$ of the emission. We thus need to perform a change of variable,

$$
k_\perp^2 = \frac{2 \, y \, (1 - x - y) \, p_a \cdot p_b - (1 - x - y)^2 m_a^2 - y^2 m_b^2}{1 - \frac{m_a^2 \, m_b^2}{(p_a \cdot p_b)^2}} \quad (5.53)
$$

which yields the jacobian

$$
\frac{dk_\perp^2}{k_\perp^2} = \frac{1 - x - 2 \, y + (1 - x - y) \frac{m_a^2}{p_a \cdot p_b} - y \frac{m_b^2}{p_a \cdot p_b}}{1 - x - y - \frac{(1-x-y)^2}{2 \, y} \frac{m_a^2}{p_a \cdot p_b} - \frac{y}{2} \frac{m_b^2}{p_a \cdot p_b}} \, \frac{dy}{y} \,. \quad (5.54)
$$

The Sudakov form factor is then given by

$$
\Delta_{II}(\mathbf{k}_{\perp,max}^2, \mathbf{k}_{\perp,0}^2) = \exp \left\{ - \sum_{ak} \sum_{b \neq ak} \frac{1}{\mathcal{N}_{spec}} \int_{\mathbf{k}_{\perp,0}^2}^{\mathbf{k}_{\perp,max}} \frac{dk_\perp^2}{k_\perp^2} \int_{x_-}^{x_+} dx \, \mathcal{J}(x, y; k_\perp^2) \, \mathbf{V}^{ak,b}(p_a, p_b, p_k) \right\}
$$
$$
(5.55)
$$

where

$$\mathcal{J}(x, y; k_\perp^2) = \frac{1 - x - y - \frac{(1-x-y)^2}{2\,y}\frac{m_a^2}{p_a\cdot p_b} - \frac{y}{2}\frac{m_b^2}{p_a\cdot p_b}}{1 - x - 2\,y + (1-x-y)\frac{m_a^2}{p_a\cdot p_b} - y\frac{m_b^2}{p_a\cdot p_b}}\,\frac{s_{ab}}{\sqrt{\lambda_{ab}}}\,\frac{1}{x}\,\frac{f_a(\eta/x)}{f_a(\eta)}\,, \qquad (5.56)$$

and

$$\mathbf{V}^{ak,b}(p_a, p_b, p_k) = \frac{\alpha_s\,C_F}{2\pi}\left[\frac{2}{1 - x_{ab}} - (1 + x_{ab}) - \frac{x_{ab}\,m_a^2}{p_a\cdot p_k}\right]\,. \qquad (5.57)$$

The last things needed to perform the extension are the phase-space mappings and their inverted form. This is because we need to keep track of both the transformed phase-space, as well as the original one. The forward transformations can be read off from Eq. C.25 and read

$$\widetilde{p}_a^\mu = \sqrt{\frac{\lambda\,(Q^2, m_a^2, m_b^2)}{\lambda_{ab}}}\left(p_a^\mu - \frac{s_{ab}}{2\,m_b^2}p_b^\mu\right) + \frac{Q^2 - m_a^2 - m_b^2}{2\,m_b^2}p_b^\mu\,; \quad \widetilde{Q}^\mu = \widetilde{p}_a^\mu + p_b^\mu\,. \quad (5.58)$$

The inverted transformations are easilly obtained then,

$$p_a^\mu = \frac{1}{x}\left[\sqrt{\frac{(2\,\widetilde{p}_a\cdot\widetilde{p}_b)^2 - 4\,m_a^2\,m_b^2\,x^2}{\lambda\,((\widetilde{p}_a + \widetilde{p}_b)^2, m_a^2, m_b^2)}}\left(\widetilde{p}_a^\mu - \frac{\widetilde{p}_a\cdot\widetilde{p}_b}{m_b^2}\widetilde{p}_b^\mu\right) + \frac{\widetilde{p}_a\cdot\widetilde{p}_b}{m_b^2}\widetilde{p}_b^\mu\right]\,, \qquad (5.59)$$

$$p_b^\mu = \widetilde{p}_b^\mu\,, \qquad (5.60)$$

$$p_k^\mu = \frac{1 - x - y - y\,m_b^2}{1 - \frac{m_a^2\,m_b^2}{(p_a\cdot p_b)^2}}p_a^\mu + \frac{y - (1 - x - y)\frac{m_a^2\,x}{\widetilde{p}_a\cdot\widetilde{p}_b}}{1 - \frac{m_a^2\,m_b^2}{(p_a\cdot p_b)^2}}\widetilde{p}_b^\mu + k_\perp^\mu\,. \qquad (5.61)$$

With all the necessary formulae, we can now test this scheme on a simple example. We chose here to replicate the set-up of section 4.2 and check with data taken from ATLAS. Matrix elements are generated in SHERPA with the built-in generators AMEGIC++ [60] and COMIX [61]. While virtual matrix elements contributing to QCD NLO corrections are taken from OPENLOOPS [65].

In this case we chose only to compare against the 1 b-jet selection, this is because we can test both the matrix element corrections presented in the previous section as well as the shower. For more particles the accuracy would only be that of the shower, *i.e.* leading-log.

In Figs. 5.5,5.6 we show a multijet merged prediction based on $pp \to Z+$ up tp 3 jets. where the zero jet component of this sample is evaluated with MC@NLO accuracy, while the rest of the samples are leading order. We thus have the same fixed-order accuracy on the 5F MEPS@LO of section 4.2. Indeed this set-up, as
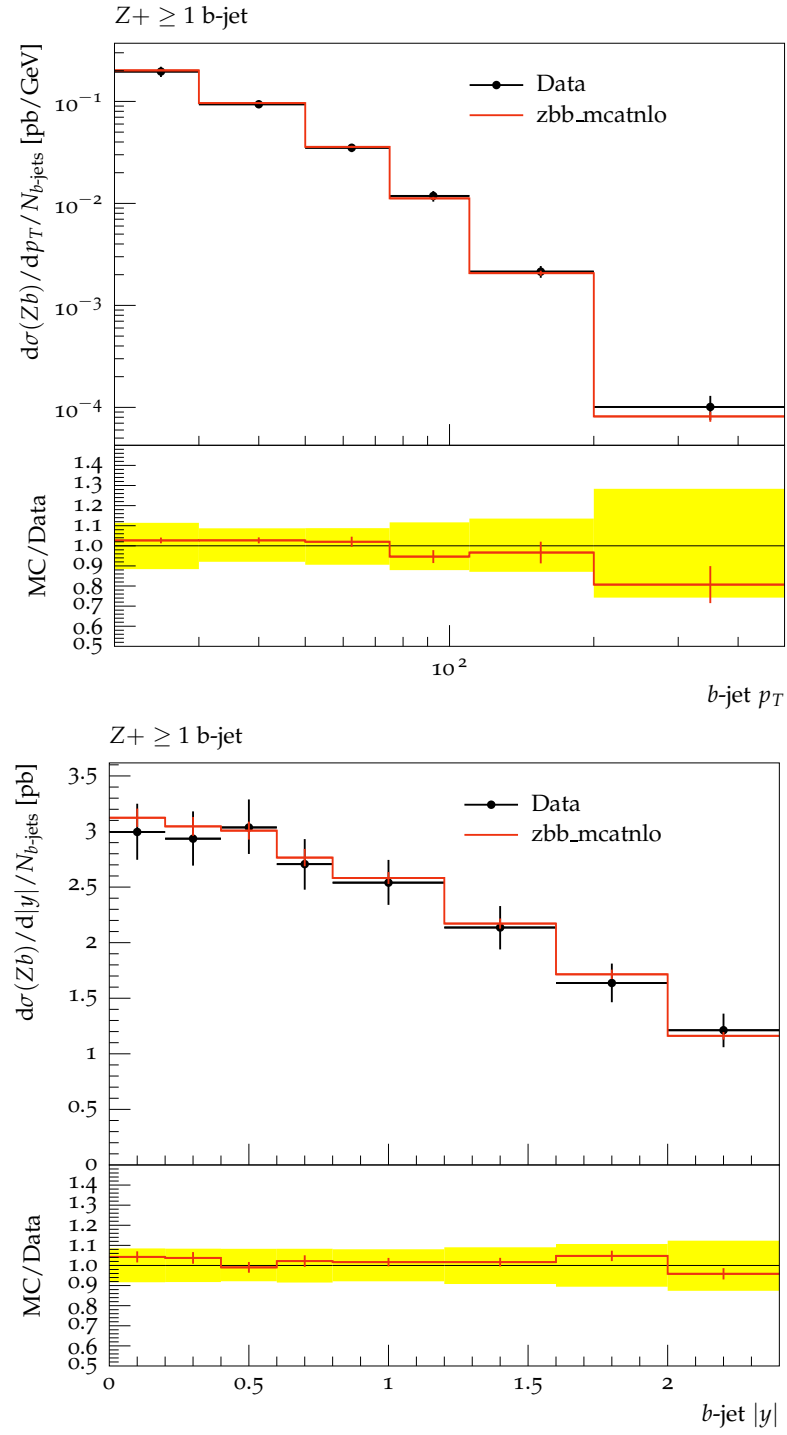
Figure 5.5: Inclusive transverse-momentum and rapidity distribution of all b-jets in events with at least one b-jet. Data taken from Ref. [57].

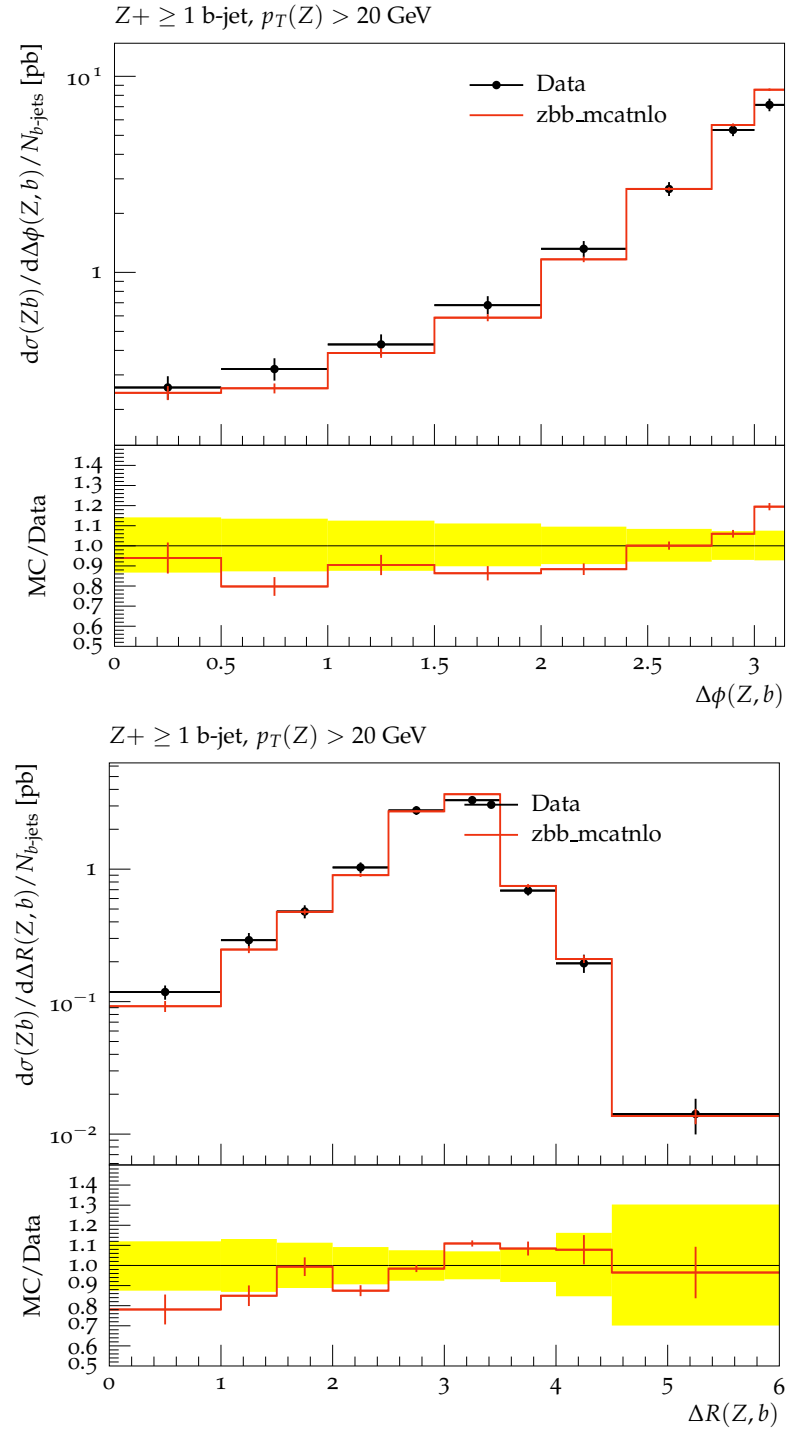Figure 5.6: Angular and ΔR separation between the reconstructed Z boson and b-jets in events with at least one b-jet. Data taken from Ref. [57].

well as the ones presented in section 4.2 show good agreement with data points for all curves, which is reassuring of the implementation. A more detailed study of processes for which this scheme is of interest is currently on going.

Chapter 6

Conclusions and outlook

In this work we present theoretically consistent methods to estimate, and include, quark mass effects in theoretical predictions in a systematic way. We show, in particular, what is the interplay, using the FONLL matching technique together with comparison with LHC data, between the resummation of collinear logarithms and power suppressed mass corrections, for the production of a heavy boson in association with bottom quarks.

As the dominant contribution stems from the resummation of collinear logarithms, that are consistently included in a completely massless picture, or *five-flavour* scheme, we provide a method to extend such scheme to accommodate for the inclusion of mass effects. This is done in the context of the SHERPA Monte Carlo event generator, at MC@NLO accuracy.

In Chapter 2, we show how to consistently match a completely massless picture for handling bottom quarks, or five-flavour scheme, with a completely massive one, or *four-flavour* scheme. This matched prediction, then includes the resummation of collinear logarithms, to the accuracy of the five-flavour scheme, and mass effects at the fixed order accuracy of the four-flavour scheme. We perform this matching in the context of the production of a Higgs boson in association with heavy quarks at the LHC at the NNLL+NLO accuracy. We find that mass corrections account for a $\sim 5\%$ effects on top of the five-flavour scheme. These contributions, however, are non negligible, as we find they are roughly of the same size of scale variations, and therefore are a non negligible source of uncertainty. An implementation for the

production of a Higgs boson in bottom quark fusion in the FONLL scheme, has been made publicly available and can be found in [87] .

In Chapter 3, we compare Monte Carlo predictions for the five-flavour and the four-flavour scheme with LHC data, gathered at the centre of mass energy of 7 TeV, for the production of a Z boson in association with at least one or at least to bottom quark jets. We find that the MEPS@LO five-flavour scheme prediction and the MC@NLO four-flavour one, disagree with data by a largely flat factor of about 10-20%. In particular the former agrees better for the one b jet inclusive sample with the latter undershooting, while their role is essentially reversed for the two b jets inclusive sample. On top of these two predictions a MEPS@NLO five-flavour scheme calculation is also provided. This sample agrees well with data for all observables provided. We find, in addition, that the three sample agree among themselves up to a, roughly constant, normalisation factor. We then test this argument in the case of Higgs boson production, where we confirm our finding in the case of the Z boson.

In Chapter 4, we start from a standard five-flavour scheme to construct five-flavour massive scheme that can be used in Monte Carlo predictions, at the *next-to-leading* order accuracy. Firstly we extend the currently used subtraction method in SHERPA, the Catani-Seymour dipole method, to include massive quarks in the initial state. We focus in particular on the *initial-initial* configuration as it is the most relevant for the examples considered in this work. We describe how to obtain the *initial-final* configuration from results present in the literature. In this chapter we show how to construct efficient subtraction terms in the presence of massive initial state quarks, in hadron-hadron collisions. These contribution have been implemented in SHERPA and will be made public in a future release. We then show how the inclusion of mass effects impact the fixed-order prediction for the production of a Higgs boson in bottom quark fusion, in this scheme. In addition we show how including, or not, mass effects in the parton densities evolution can affect the consistency of this massive scheme. We find, as expected, that mass effects play a few percent role in the low p_T region of the Higgs boson spectrum while reconciling with the standard five-flavour scheme for high p_T.

It is important to underline how the studies performed in the context of this work

help having reliable predictions for processes involving heavy quarks at the LHC, and, as such, heavily reducing their theoretical uncertainties. When feeding theory predictions in experimental analysis, in fact, the difference between the four- and the five-flavour scheme is usually taken as input of additional theory uncertainties. In addition, as these two schemes largely disagree for most processes, this extra source of uncertainty is generally quite large and definitely non negligible. This work, on the other hand, aims at showing consistent methods of including both aspects of these schemes consistently, at all energies. This eliminates the need of having the additional theory uncertainty coming from the difference between the two schemes.

There are a couple of interesting points that are worth expanding in a continuation of this work. Firstly, once the validation of the MC@NLO method is completed we plan to produce a comparison between a five-flavour massive scheme next-to-leading order, merged sample with the FONLL matched cross section in the cases where this is possible. Secondly, it is interesting to investigate to what extent higher twist corrections are suppressed as expected. In particular we are in the process of testing our newly developed scheme for more complicated processes where we can test our hypothesis. Lastly we are in the process of extending the FONLL method for other phenomenologically relevant processes, like the production of a Z boson in bottom quark fusion, single top production and the next-to-next-to-leading log resummed p_T spectrum in Drell-Yan.

Appendix A

Mathematical Tools

A.1 Colour Algebra of SU (3)

Here we report some useful relations for the colour algebra of SU (3).

For the case with two partons, using colour conservation, we have:

$$\mathbf{T}_1 \cdot \mathbf{T}_2 \, |1, 2> = -\mathbf{T}_1 \cdot \mathbf{T}_1 \, |1, 2> = -\mathbf{T}_1^2 \, |1, 2> = -\mathbf{T}_2^2 \, |1, 2> , \qquad (A.1)$$

so that all the charge operators $\{\mathbf{T}_1^2, \mathbf{T}_2^2, \ -\mathbf{T}_1 \cdot \mathbf{T}_2\}$ are factorizable in terms of the (scalar) Casimir operator $C_1 = C_2$.

Using colour conservation for the three-parton case we have:

$$
\begin{aligned}
0 &= \left(\sum_{i=1}^{3} \mathbf{T}_i\right)^2 |1, 2, 3> \\
&= \left(\mathbf{T}_1^2 + \mathbf{T}_2^2 + \mathbf{T}_3^2 + 2\,\mathbf{T}_1 \cdot \mathbf{T}_2 + 2\,\mathbf{T}_1 \cdot \mathbf{T}_3 + 2\,\mathbf{T}_2 \cdot \mathbf{T}_3\right) |1, 2, 3> , \quad (A.2)
\end{aligned}
$$

and

$$(\mathbf{T}_1 \cdot \mathbf{T}_2 + \mathbf{T}_1 \cdot \mathbf{T}_3) \, |1, 2, 3> = -\mathbf{T}_1^2 \, |1, 2, 3> . \qquad (A.3)$$

Combining these two equations we get:

$$2\,\mathbf{T}_2 \cdot \mathbf{T}_3 \, |1, 2, 3> = \left(\mathbf{T}_1^2 - \mathbf{T}_2^2 - \mathbf{T}_3^2\right) |1, 2, 3> \qquad (A.4)$$

and similarly for $\mathbf{T}_1 \cdot \mathbf{T}_3$ and $\mathbf{T}_1 \cdot \mathbf{T}_2$. Therefore, all the charge operators are factorizable in terms of linear combinations of the Casimir invariants C_1, C_2, C_3 of the three partons.

When the total number n of partons is $n \geq 4$ the colour algebra does not factorize any longer. For instance, if $n = 4$ we have four trivial relations, namely

$$\mathbf{T}_i^2 |1, 2, 3, 4> = C_i |1, 2, 3, 4> \ , \quad i = 1, ..., 4 \ . \tag{A.5}$$

As for the remaining six charge operators $\mathbf{T}_i \cdot \mathbf{T}_j (i \neq j)$, we can use the following four identities (due to charge conservation)

$$\mathbf{T}_i \cdot \sum_{j=1}^{4} \mathbf{T}_j |1, 2, 3, 4> = 0 \ , \quad i = 1, ..., 4 \ , \tag{A.6}$$

in order to single out two independent charge operators. For instance we can write:

$$
\begin{aligned}
\mathbf{T}_3 \cdot \mathbf{T}_4 |1, 2, 3, 4> &= \left[\frac{1}{2} \left(C_1 + C_2 - C_3 - C_4 \right) + \mathbf{T}_1 \cdot \mathbf{T}_2 \right] |1, 2, 3, 4> \ , \\
\mathbf{T}_2 \cdot \mathbf{T}_4 |1, 2, 3, 4> &= \left[\frac{1}{2} \left(C_1 + C_3 - C_2 - C_4 \right) + \mathbf{T}_1 \cdot \mathbf{T}_3 \right] |1, 2, 3, 4> \ , \\
\mathbf{T}_2 \cdot \mathbf{T}_3 |1, 2, 3, 4> &= \left[\frac{1}{2} \left(C_4 - C_1 - C_2 - C_3 \right) - \mathbf{T}_1 \cdot \mathbf{T}_2 - \mathbf{T}_1 \cdot \mathbf{T}_3 \right] |1, 2, 3, 4> \ , \\
\mathbf{T}_1 \cdot \mathbf{T}_4 |1, 2, 3, 4> &= - \left(C_1 + \mathbf{T}_1 \cdot \mathbf{T}_2 + \mathbf{T}_1 \cdot \mathbf{T}_3 \right) |1, 2, 3, 4> \ , \tag{A.7}
\end{aligned}
$$

and express all the charge operators in terms of Casimir invariants and $\mathbf{T}_1 \cdot \mathbf{T}_2, \mathbf{T}_1 \cdot \mathbf{T}_3$.

A.2   *d*–dimensional spherical coordinates

Leaving out the 0–th component, we have $d-1$ euclidean dimensions that we can parametrise by means of one length, ρ, and $d-2$ angles. Let us further split them in $d-3$ angles, $\theta_i \in [0, \pi]$ and $\phi \in [0, 2\pi]$.

$$
p = \begin{pmatrix}
p_1 = & \rho \cos \theta_1 \\
p_2 = & \rho \sin \theta_1 \cos \theta_2 \\
p_3 = & \rho \sin \theta_1 \sin \theta_2 \cos \theta_3 \\
p_4 = & \rho \sin \theta_1 \sin \theta_2 \sin \theta_3 \cos \theta_4 \\
& \dots \\
& \dots \\
p_{d-2} = & \rho \sin \theta_1 \sin \theta_2 \sin \theta_3 \dots \cos \phi \\
p_{d-1} = & \rho \sin \theta_1 \sin \theta_2 \sin \theta_3 \dots \sin \phi
\end{pmatrix}
\tag{A.8}
$$

The $d-1$ dimensional phase–space can thus be written as

$$
\mathrm{d}^{d-1}p = \mathrm{d}\rho\, \rho^{d-2}\mathrm{d}\theta_1\, \sin^{d-3}\theta_1 \mathrm{d}\theta_2\, \sin^{d-4}\theta_2 \dots \mathrm{d}\theta_{d-3}\, \sin\theta_{d-3}\mathrm{d}\phi\,.
\tag{A.9}
$$

A.3   Altarelli-Parisi splitting functions

Here we report the unpolarised A-P splitting functions for reference.

$$
P_{qq}(x) = C_F \left[\frac{1 + x^2}{(1 - x)_+} + \frac{3}{2}\delta(1 - x) \right],
\tag{A.10}
$$

$$
P_{qg}(x) = T_R \left[x^2 + (1 - x)^2 \right],
\tag{A.11}
$$

$$
P_{gq}(x) = C_F \left[\frac{1 + (1 - x)^2}{x} \right],
\tag{A.12}
$$

$$
P_{gg}(x) = C_A \left[\frac{x}{(1 - x)_+} + \frac{1 - x}{x} + x\,(1 - x) \right] + \beta_0\delta(1 - x),
\tag{A.13}
$$

Appendix B

Matching coefficients for massive quarks

We give for completeness the expressions of the coefficients Eq. (3.20). These were computed in Ref. [88]. There are a few differences compared to what is presented there. Firstly we separate contributions from b and $\bar{b}$. Secondly our expansion is done in powers of α_s rather than in powers of $\frac{\alpha_s}{4\pi}$. Lastly we have re-expressed the gluon and singlet PDFs in the 4FS in terms of those computed in the 5FS.

$$
\begin{aligned}
\mathcal{A}_{\Sigma b}^{(2)}(z, L) = \frac{1}{32\pi^2} C_F T_f \Bigg\{ & \left[-8(1+z)\ln z - \frac{16}{3z} - 4 + 4z + \frac{16}{3}z^2 \right] L^2 \\
& - \left[8(1+z)\ln^2 z - \left(8 + 40z + \frac{64}{3}z^2\right)\ln z - \frac{160}{9z} + 16 - 48z + \frac{448}{9}z^2 \right] L \\
& + (1+z)\left[32\mathrm{S}_{1,2}(1-z) + 16\ln z\mathrm{Li}_2(1-z) - 16\zeta(2)\ln z - \frac{4}{3}\ln^3 z \right] \\
& + \left(\frac{32}{3z} + 8 - 8z - \frac{32}{3}z^2\right)\mathrm{Li}_2(1-z) + \left(-\frac{32}{3z} - 8 + 8z + \frac{32}{3}z^2\right)\zeta(2) \\
+ \left(2 + 10z + \frac{16}{3}z^2\right)\ln^2 z - & \left(\frac{56}{3} + \frac{88}{3}z + \frac{448}{9}z^2\right)\ln z - \frac{448}{27z} - \frac{4}{3} - \frac{124}{3}z + \frac{1600}{27}z^2 \Bigg\},
\end{aligned}
$$

$$
\tag{B.1}
$$

$$
\mathcal{A}_{gb}^{(1)}(z, L) = \frac{T_f}{2\pi}\left[(z^2 + (1-z)^2)L \right], \tag{B.2}
$$

and

$$\mathcal{A}_{bg}^{(2)}(z,L) = \frac{1}{32\pi^2}\Biggl\{\biggl\{C_F T_f[(8-16z+16z^2)\ln(1-z)-(4-8z+16z^2)\ln z-(2-8z)]$$

$$+ C_A T_f\biggl[-(8-16z+16z^2)\ln(1-z)-(8+32z)\ln z-\frac{16}{3z}-4-32z+\frac{124}{3}z^2\biggr]$$

$$+ T_f^2\biggl[-\frac{16}{3}(z^2+(1-z)^2)\biggr]+T_f\biggl[\frac{2}{3}(z^2+(1-z)^2)\biggr]\biggr\}L^2$$

$$-\biggl\{C_F T_f\biggl[(8-16z+16z^2)[2\ln z\ln(1-z)-\ln^2(1-z)+2\zeta(2)]$$

$$-(4-8z+16z^2)\ln^2 z-32z(1-z)\ln(1-z)-(12-16z+32z^2)\ln z-56+116z-80z^2\biggr]$$

$$+ C_A T_f\biggl[(16+32z+32z^2)[\text{Li}_2(-z)+\ln z\ln(1+z)]+(8-16z+16z^2)\ln^2(1-z)$$

$$+ (8+16z)\ln^2 z+32z\zeta(2)+32z(1-z)\ln(1-z)-\left(8+64z+\frac{352}{3}z^2\right)\ln z$$

$$-\frac{160}{9z}+16-200z+\frac{1744}{9}z^2\biggr]\biggr\}L$$

$$+ C_F T_f\biggl\{(1-2z+2z^2)[8\zeta(3)+\frac{4}{3}\ln^3(1-z)-8\ln(1-z)\text{Li}_2(1-z)+8\zeta(2)\ln z$$

$$-4\ln z\ln^2(1-z)+\frac{2}{3}\ln^3 z-8\ln z\text{Li}_2(1-z)+8\text{Li}_3(1-z)-24\text{S}_{1,2}(1-z)]$$

$$+ z^2\biggl[-16\zeta(2)\ln z+\frac{4}{3}\ln^3 z+16\ln z\text{Li}_2(1-z)+32\text{S}_{1,2}(1-z)\biggr]$$

$$-(4+96z-64z^2)\text{Li}_2(1-z)-(4-48z+40z^2)\zeta(2)$$

$$-(8+48z-24z^2)\ln z\ln(1-z)+(4+8z-12z^2)\ln^2(1-z)$$

$$-(1+12z-20z^2)\ln^2 z-(52z-48z^2)\ln(1-z)-(16+18z+48z^2)\ln z+26-82z+80z^2\biggr\}$$

$$+ C_A T_f\biggl\{(1-2z+2z^2)[-\frac{4}{3}\ln^3(1-z)+8\ln(1-z)\text{Li}_2(1-z)-8\text{Li}_3(1-z)]+(1+2z+2z^2)$$

$$\times[-8\zeta(2)\ln(1+z)-16\ln(1+z)\text{Li}_2(-z)-8\ln z\ln^2(1+z)$$

$$+ 4\ln^2 z\ln(1+z)+8\ln z\text{Li}_2(-z)-8\text{Li}_3(-z)-16\text{S}_{1,2}(-z)]$$

$$+ (16+64z)[2\text{S}_{1,2}(1-z)+\ln z\text{Li}_2(1-z)]-\left(\frac{4}{3}+\frac{8}{3}z\right)\ln^3 z$$

$$+ (8-32z+16z^2)\zeta(3)-(16+64z)\zeta(2)\ln z+(16+16z^2)$$

$$\times \left[\text{Li}_2(-z) + \ln z \ln(1+z)\right] + \left(\frac{32}{3z} + 12 + 64z - \frac{272}{3}z^2\right)\text{Li}_2(1-z)$$

$$- \left(12 + 48z - \frac{260}{3}z^2 + \frac{32}{3z}\right)\zeta(2) - 4z^2 \ln z \ln(1-z)$$

$$- (2 + 8z - 10z^2)\ln^2(1-z) + \left(2 + 8z + \frac{46}{3}z^2\right)\ln^2 z$$

$$+ (4 + 16z - 16z^2)\ln(1-z) - \left(\frac{56}{3} + \frac{172}{3}z + \frac{1600}{9}z^2\right)\ln z$$

$$\left.\left.- \frac{448}{27z} - \frac{4}{3} - \frac{628}{3}z + \frac{6352}{27}z^2\right\}\right\} . \quad \text{(B.3)}$$

Appendix C

Initial state massive subtraction

C.1 Initial massive quarks kinematics

Initial quarks momenta are parametrised, in the partonic centre of mass frame as

$$x = \frac{1}{2} + \frac{m_a^2 - m_b^2}{2\,s}\,, \tag{C.1}$$

$$p_a = \left(x\,\sqrt{s}, 0, 0, \frac{\sqrt{\lambda(s, m_a^2, m_b^2)}}{2\,\sqrt{s}} \right)\,, \tag{C.2}$$

$$p_b = \left((1-x)\,\sqrt{s}, 0, 0, -\frac{\sqrt{\lambda(s, m_a^2, m_b^2)}}{2\,\sqrt{s}} \right)\,. \tag{C.3}$$

In the hadronic centre of mass we get instead

$$p_{a,b} = \eta_{1,2}\,P_{1,2} + \frac{m_{a,b}^2}{\eta_{1,2}\,S}\,P_{2,1}\,; \quad \eta_{1,2} \in (0, 1]\,, \tag{C.4}$$

where $P_{1,2}$ are the hadronic momenta and are given by

$$P_{1,2} = \frac{\sqrt{S}}{2}\,(1, 0, 0, \pm 1)\,. \tag{C.5}$$

C.2 Initial-Initial massive subtraction integral

In this appendix we present the explicit ingredients used to derive the massive subtraction integrated terms.

The integrated subtraction term, $\mathcal{I}$, is given by the d-dimensional phase space integral of the unpolarised splitting function Eq.(5.7). The phase space can be

obtained from

$$\int d\Phi_{N+1}(p_k, Q; p_a + p_b) = \int_0^1 dx \int d\Phi_N(\widetilde{Q}(x); \widetilde{p}_a(x) + p_b) \int \left[d^{d-1}p_k(s, x, y_a)\right] , \tag{C.6}$$

expanding both sides,

$$\frac{((1-x)\, s_{ab})^{d-3}}{(2\,\pi)^{d-2}\, 2^{d-1}\, s^{\frac{d-2}{2}}} d\,\Omega_{d-3}\, \Theta\,(x-\alpha) = \frac{2\,\pi}{s_{ab}} \delta(x - x_{ab})\left[d\,k(s, x, y_{ab})\right] , \tag{C.7}$$

with

$$d\,\Omega_{d-3} = -\frac{4\,\pi^{1-\epsilon}}{\Gamma(1-\epsilon)}\, \frac{s}{\sqrt{\lambda_{ab}}\,(1-x)}\,(\sin\theta)^{-\epsilon}\Big|_{\theta\to y}\, \Theta\left[(y_1 - y_{ab})\,(y_{ab} - y_2)\right]\, d\,y_{ab} , \tag{C.8}$$

and

$$y_{1,2}(x) = \frac{(1-x)}{2\,s}\left(s_{ab} + 2\,m_a^2 \pm \sqrt{\lambda_{ab}}\right). \tag{C.9}$$

Finally we get

$$\int \left[d^{d-1}p_k(s, x, y_a)\right] = \frac{1}{16\,\pi^2}\, \frac{(4\pi)^\varepsilon}{\Gamma(1-\varepsilon)}\, \left(\frac{s_{ab}}{\sqrt{\lambda_{ab}}}\right)^{1-2\varepsilon}\, (1-x)^{1-2\varepsilon}\, s_{ab}\, s^{-\varepsilon}$$
$$\int_{v_2}^{v_1} dv\left[(v_1 - v)\,(v - v_2)\right]^{-\varepsilon} , \tag{C.10}$$

where, to further simplify the expression, we perform the change of variable $y_{ab} \to v_{ab}\,(1-x)$,

C.2.1   The integral in v

We start by re-writing the dipole function in terms of the splitting variables x, v, s,

$$\mathbf{V}^{q_a g_k, b}(x, v; s) = \frac{1}{s_{ab}\,(1-x)\,v\,x}\left[\frac{2}{1-x} - 1 - x - \epsilon\,(1-x) - \frac{2\,x\,m_a^2}{s_{ab}\,v\,(1-x)}\right]. \tag{C.11}$$

In order to simplify the following expressions we take for any function f:

$$f(x, \epsilon) = \sum_{i=-\infty}^{\infty} \epsilon^i f^{(i)}(x); \tag{C.12}$$

further, we write

$$\mathbf{V}^{q_a g_k, b}(x, v; s) = \frac{1}{x\, s_{ab}}\left[\frac{h_1(x, \epsilon)}{v} + \frac{h_2(x; s)}{v^2}\right] \tag{C.13}$$

with

$$h_1(x, \epsilon) = \frac{1 + x^2}{(1 - x)^2} - \epsilon, \quad h_2(x; s) = -\frac{2 \, x \, m_a^2}{s_{ab} \, (1 - x)^2} \tag{C.14}$$

further, calling $h = h_1 + h_2$ we have:

$$h^{(0)}(x; s) = \frac{1 + x^2 - \frac{2 \, x \, m_a^2}{s_{ab}}}{(1 - x)^2}; \quad \text{and} \quad h^{(1)} = -1. \tag{C.15}$$

The result of the first integral can be written as follows

$$\mathcal{V}(x) = x \, s_{ab} \int_{v_1}^{v_2} \mathrm{d} \, v_{ab} \, [(v_1 - v_{ab}) \, (v_{ab} - v_2)]^{-\epsilon} \, \mathbf{V}^{q_a g_k, b}(x, v; s) =$$

$$\frac{1}{(1 - x)^2} \left[(a + \epsilon \, b) \, (1 + x^2) - \frac{2 \, x \, m_a^2}{s_{ab}} (c + \epsilon \, d) \right]. \tag{C.16}$$

When plugging in the full phase space we get a term like

$$(1 - x)^{1 - 2\epsilon} \, \mathcal{V}(x) = (1 - x)^{-1 - 2\epsilon} \left[(a + \epsilon \, b) \, (1 + x^2) - \frac{2 \, x \, m_a^2}{s_{ab}} (c + \epsilon \, d) \right], \tag{C.17}$$

which diverges in the limit $x \to 1$ when $\epsilon \to 0$. To solve this problem we introduce a plus distribution

$$\widetilde{\mathcal{V}}^{a,b}(x; \varepsilon) = \delta(1 - x) \, \mathcal{V}^{a,b}(\varepsilon; \alpha) + \left[K^{a,b}(x) \right]_+. \tag{C.18}$$

with

$$\left[\int_0^1 \mathrm{d}x \, K^{a,b}(x) \right] = -\frac{1}{\epsilon} \left(a + \frac{2 \, c \, m_a^2}{s_{ab}} \right) - \left[\frac{3 \, a + 2 \, b}{2} + \frac{m_a^2}{s_{ab}} (2 \, c + d) \right] + \mathcal{O}(\epsilon). \tag{C.19}$$

The term $\mathcal{V}^{a,b}(\varepsilon; \alpha)$ is then given by

$$\mathcal{V}^{a,b}(\varepsilon; \alpha) = \int_0^1 \mathrm{d}x \, K^{a,b}(x) - \Theta(1 - \alpha) \, \Theta(\alpha) \int_0^\alpha \mathrm{d}x \, K^{a,b}(x) \tag{C.20}$$

which yield

$$\mathcal{V}^{a,b}(\varepsilon; \alpha) = \frac{1 + \frac{s_{ab}}{\sqrt{\lambda_{ab}}} \log \beta_0}{\varepsilon} + \log \left(\frac{\mu^2 \, s}{s_{ab}^2} \right) + \frac{3}{2}$$

$$+ \frac{s_{ab}}{\sqrt{\lambda_{ab}}} \left\{ \left[\log \left(\frac{\mu^2 \, \lambda_{ab}}{m_a^2 s_{ab}^2} \right) + \left(\frac{1}{2} - \frac{2 \, m_a^2}{s_{ab}} \right) \right] \log \beta_0 + 2 \operatorname{Li}_2(\beta_0) + \frac{1}{2} \log^2 \beta_0 - \frac{\pi^2}{3} \right\}$$

$$+ \frac{s_{ab}}{\sqrt{\lambda_{ab}}} \log \beta_0 \left(\frac{\alpha^2}{2} + \alpha + 2 \log (1 - \alpha) \right) - 2 \, (\alpha + \log (1 - \alpha)), \tag{C.21}$$

which corresponds to Eq. (5.18) for $\alpha = 0$.

C.2.2 The integral in x

In order to compute the integrated subtraction term for hadron-hadron collisions we need to convolve the K functions with partonic matrix elements. As we discuss in the chapter, this is far from being efficient and it is customary perform a change of variable that allows to evaluate matrix elements only for one momentum configuration per event. We start from Eq. (5.26)

$$
\mathcal{I} = \frac{\alpha_s\, C_F}{2\,\pi} \iint \mathrm{d}\eta_1\,\mathrm{d}\eta_2\, f_a(\eta_1)\, f_b(\eta_2) \Bigg\{ \mathcal{V}^{a,b}(\varepsilon)\, \mathrm{d}\hat\sigma_N(s_{ab})
$$
$$
+ \int_0^1 \mathrm{d}x\, K^{a,b}(x) \left[\frac{\phi(x\, s_{ab})}{x\, \phi(s_{ab})} \mathrm{d}\hat\sigma_N(x\, s_{ab}) - \mathrm{d}\hat\sigma_N(s_{ab}) \right] \Bigg\}. \quad \text{(C.22)}
$$

The idea is, then, to find a variable transformation such that

$$
x\, s_{ab}(\eta_1, \eta_2) = s_{ab}(\eta_1'(x), \eta_2'), \quad \text{(C.23)}
$$

$$
\eta_2' = \eta_2\,. \quad \text{(C.24)}
$$

We find that this is achieved by defining

$$
\eta(x, \eta_2; \eta_1') = \frac{\left(\frac{m_a^2\, m_b^2}{S^2\, \eta_2} + \eta_1'^2 \right) \left(\sqrt{1 - \frac{4 \frac{m_a^2\, m_b^2}{S^2\, \eta_2} \eta_1'^2 x^2}{\left(\frac{m_a^2\, m_b^2}{S^2\, \eta_2} + \eta_1'^2 \right)^2}} + 1 \right)}{2\, \eta_1'\, x}\,, \quad \text{(C.25)}
$$

which yields the Jacobian

$$
\mathcal{J}(\eta_1', \eta_2, x) = \frac{\left(\eta_1'^2 - \frac{m_a^2\, m_b^2}{S^2\, \eta_2} \right)}{\eta_1'^2 \left(\eta_1'^2 + \frac{m_a^2\, m_b^2}{S^2\, \eta_2} \right) \sqrt{1 - \frac{4 \frac{m_a^2\, m_b^2}{S^2\, \eta_2} \eta_1'^2 x^2}{\left(\frac{m_a^2\, m_b^2}{S^2\, \eta_2} + \eta_1'^2 \right)^2}}}\, \eta(x, \eta_2; \eta_1')\,. \quad \text{(C.26)}
$$

With this definitions and Eq. (5.31) the integral in Eq. (5.32) is completely defined.

Bibliography

[1] Stefano Forte, Davide Napoletano, and Maria Ubiali. Higgs production in bottom-quark fusion in a matched scheme. *Phys. Lett.*, B751:331–337, 2015.

[2] Stefano Forte, Davide Napoletano, and Maria Ubiali. Higgs production in bottom-quark fusion: matching beyond leading order. *Phys. Lett.*, B763:190–196, 2016.

[3] D. de Florian et al. Handbook of LHC Higgs Cross Sections: 4. Deciphering the Nature of the Higgs Sector. 2016.

[4] Frank Krauss, Davide Napoletano, and Steffen Schumann. Simulating b-associated production of Z and Higgs bosons with the SHERPA event generator. *Phys. Rev.*, D95(3):036012, 2017.

[5] J. R. Andersen et al. Les Houches 2015: Physics at TeV Colliders Standard Model Working Group Report. In *9th Les Houches Workshop on Physics at TeV Colliders (PhysTeV 2015) Les Houches, France, June 1-19, 2015*, 2016.

[6] Georges Aad et al. Observation of a new particle in the search for the Standard Model Higgs boson with the ATLAS detector at the LHC. *Phys.Lett.*, B716:1–29, 2012.

[7] Serguei Chatrchyan et al. Observation of a new boson at a mass of 125 GeV with the CMS experiment at the LHC. *Phys.Lett.*, B716:30–61, 2012.

[8] John C. Collins, Davison E. Soper, and George F. Sterman. Factorization for short–distance hadron–hadron scattering. *Nucl.Phys.*, B261:104, 1985.

[9] John C. Collins, Davison E. Soper, and George Sterman. Factorization of hard processes in QCD. *Adv. Ser. Direct. High Energy Phys.*, 5:1–91, 1988.

[10] Guido Altarelli and G. Parisi. Asymptotic freedom in parton language. *Nucl. Phys.*, B126:298–318, 1977.

[11] V. N. Gribov and L. N. Lipatov. Deep–inelastic *e-p* scattering in perturbation theory. *Sov. J. Nucl. Phys.*, 15:438–450, 1972.

[12] Y. L. Dokshitzer. Calculation of the structure functions for deep–inelastic scattering and e^+e^- annihilation by perturbation theory in quantum chromodynamics. *Sov. Phys. JETP*, 46:641–653, 1977.

[13] T. Kinoshita. Mass singularities of Feynman amplitudes. *J.Math.Phys.*, 3:650–677, 1962.

[14] T.D. Lee and M. Nauenberg. Degenerate systems and mass singularities. *Phys.Rev.*, 133:B1549–B1562, 1964.

[15] S. Catani and M. H. Seymour. A general algorithm for calculating jet cross sections in NLO QCD. *Nucl. Phys.*, B485:291–419, 1997.

[16] Stefano Catani, Stefan Dittmaier, Michael H. Seymour, and Zoltan Trocsanyi. The dipole formalism for next–to–leading order QCD calculations with massive partons. *Nucl. Phys.*, B627:189–265, 2002.

[17] S. Frixione, Z. Kunszt, and A. Signer. Three-jet cross-sections to next–to–leading order. *Nucl. Phys.*, B467:399–442, 1996.

[18] Stefan Dittmaier. A general approach to photon radiation off fermions. *Nucl. Phys.*, B565:69–122, 2000.

[19] W. T. Giele and E. W. Nigel Glover. Higher-order corrections to jet cross sections in e^+e^- annihilation. *Phys. Rev.*, D46:1980–2010, 1992.

[20] W.T. Giele, E.W. Nigel Glover, and David A. Kosower. Higher order corrections to jet cross-sections in hadron colliders. *Nucl.Phys.*, B403:633–670, 1993.

[21] S. Catani, B. R. Webber, and G. Marchesini. QCD coherent branching and semiinclusive processes at large x. *Nucl. Phys.*, B349:635–654, 1991.

[22] R. Keith Ellis, Howard Georgi, Marie Machacek, H. David Politzer, and Graham G. Ross. Factorization and the Parton Model in QCD. *Phys.Lett.*, B78:281, 1978.

[23] D. Amati, R. Petronzio, and G. Veneziano. Relating hard QCD processes through universality of mass singularities. 2. *Nucl. Phys.*, B146:29–49, 1978.

[24] Stefano Catani, Frank Krauss, Ralf Kuhn, and Brian R. Webber. QCD matrix elements + parton showers. *JHEP*, 11:063, 2001.

[25] Stefan Höche, Frank Krauss, Steffen Schumann, and Frank Siegert. QCD matrix elements and truncated showers. *JHEP*, 05:053, 2009.

[26] Stefan Höche, Frank Krauss, Marek Schönherr, and Frank Siegert. NLO matrix elements and truncated showers. *JHEP*, 1108:123, 2011.

[27] Thomas Gehrmann, Stefan Höche, Frank Krauss, Marek Schönherr, and Frank Siegert. NLO QCD matrix elements + parton showers in $e^+e^- \rightarrow$ hadrons. 2012.

[28] Matteo Cacciari, Mario Greco, and Paolo Nason. The P(T) spectrum in heavy flavor hadroproduction. *JHEP*, 9805:007, 1998.

[29] Stefano Forte, Eric Laenen, Paolo Nason, and Juan Rojo. Heavy quarks in deep-inelastic scattering. *Nucl.Phys.*, B834:116–162, 2010.

[30] Robert V. Harlander and William B. Kilgore. Higgs boson production in bottom quark fusion at next-to-next-to leading order. *Phys. Rev.*, D68:013001, 2003.

[31] Stefan Dittmaier, Michael Kramer, 1, and Michael Spira. Higgs radiation off bottom quarks at the Tevatron and the CERN LHC. *Phys. Rev.*, D70:074010, 2004.

[32] S. Dawson, C. B. Jackson, L. Reina, and D. Wackeroth. Exclusive Higgs boson production with bottom quarks at hadron colliders. *Phys. Rev.*, D69:074027, 2004.

[33] Fabio Maltoni, Giovanni Ridolfi, and Maria Ubiali. b-initiated processes at the LHC: a reappraisal. *JHEP*, 07:022, 2012. [Erratum: JHEP04,095(2013)].

[34] Matthew Lim, Fabio Maltoni, Giovanni Ridolfi, and Maria Ubiali. Anatomy of double heavy-quark initiated processes. *JHEP*, 09:132, 2016.

[35] Robert Harlander, Michael Krämer, and Markus Schumacher. Bottom-quark associated Higgs-boson production: reconciling the four- and five-flavour scheme approach. 2011.

[36] S. J. Brodsky, P. Hoyer, C. Peterson, and N. Sakai. The Intrinsic Charm of the Proton. *Phys. Lett.*, 93B:451–455, 1980.

[37] J. Alwall, R. Frederix, S. Frixione, V. Hirschi, F. Maltoni, O. Mattelaer, H.-S. Shao, T. Stelzer, P. Torrielli, and M. Zaro. The automated computation of tree-level and next-to-leading order differential cross sections, and their matching to parton shower simulations. *JHEP*, 1407:079, 2014.

[38] M. Wiesemann, R. Frederix, S. Frixione, V. Hirschi, F. Maltoni, and P. Torrielli. Higgs production in association with bottom quarks. *JHEP*, 02:132, 2015.

[39] Marco Bonvini, Andrew S. Papanastasiou, and Frank J. Tackmann. Matched predictions for the $b\bar{b}H$ cross section at the 13 TeV LHC. *JHEP*, 10:053, 2016.

[40] Jon Butterworth et al. PDF4LHC recommendations for LHC Run II. *J. Phys.*, G43:023001, 2016.

[41] Richard D. Ball et al. Parton distributions for the LHC Run II. 2014.

[42] L.A. Harland-Lang, A.D. Martin, P. Motylinski, and R.S. Thorne. Parton distributions in the LHC era: MMHT 2014 PDFs. 2014.

[43] Sayipjamal Dulat, Tie Jiun Hou, Jun Gao, Marco Guzzi, Joey Huston, et al. The CT14 Global Analysis of Quantum Chromodynamics. 2015.

[44] Stefano Carrazza, Stefano Forte, Zahari Kassabov, Jose Ignacio Latorre, and Juan Rojo. An Unbiased Hessian Representation for Monte Carlo PDFs. 2015.

[45] Jun Gao and Pavel Nadolsky. A meta-analysis of parton distribution functions. *JHEP*, 07:035, 2014.

[46] G. Watt and R. S. Thorne. Study of Monte Carlo approach to experimental uncertainty propagation with MSTW 2008 PDFs. *JHEP*, 08:052, 2012.

[47] F. Febres Cordero, L. Reina, and D. Wackeroth. NLO QCD corrections to W boson production with a massive b-quark jet pair at the Tevatron $p\bar{p}$ collider. *Phys.Rev.*, D74:034007, 2006.

[48] Fernando Febres Cordero, L. Reina, and D. Wackeroth. W- and Z-boson production with a massive bottom-quark pair at the Large Hadron Collider. *Phys. Rev.*, D80:034015, 2009.

[49] Rikkert Frederix, Stefano Frixione, Valentin Hirschi, Fabio Maltoni, Roberto Pittau, and Paolo Torrielli. W and $Z/\gamma*$ boson production in association with a bottom-antibottom pair. *JHEP*, 09:061, 2011.

[50] Marco Bonvini, Andrew S. Papanastasiou, and Frank J. Tackmann. Resummation and matching of b-quark mass effects in $b\bar{b}H$ production. *JHEP*, 11:196, 2015.

[51] Tongyan Lin, Edward W. Kolb, and Lian-Tao Wang. Probing dark matter couplings to top and bottom quarks at the LHC. *Phys. Rev.*, D88(6):063510, 2013.

[52] Georges Aad et al. Search for dark matter in events with heavy quarks and missing transverse momentum in pp collisions with the ATLAS detector. *Eur. Phys. J.*, C75(2):92, 2015.

[53] Ning Chen, Zhaofeng Kang, and Jinmian Li. Missing particle associated with two bottom quarks at the LHC: Mono-b versus 2b with razor variables. 2016.

[54] Georges Aad et al. Measurement of the production cross section of jets in association with a Z boson in pp collisions at $\sqrt{s} = 7$ TeV with the ATLAS detector. *JHEP*, 1307:032, 2013.

[55] V. Khachatryan et al. Measurements of jet multiplicity and differential production cross sections of $Z+$ jets events in proton-proton collisions at $\sqrt{s} = 7$ TeV. *Phys. Rev.*, D91(5):052008, 2015.

[56] Vardan Khachatryan et al. Measurements of the differential production cross sections for a Z boson in association with jets in pp collisions at sqrt(s) = 8 TeV. 2016.

[57] Georges Aad et al. Measurement of differential production cross-sections for a Z boson in association with b-jets in 7 TeV proton-proton collisions with the ATLAS detector. *JHEP*, 1410:141, 2014.

[58] Serguei Chatrchyan et al. Measurement of the cross section and angular correlations for associated production of a Z boson with b hadrons in pp collisions at $\sqrt{s} = 7$ TeV. *JHEP*, 1312:039, 2013.

[59] Vardan Khachatryan et al. Measurements of the associated production of a Z boson and b jets in pp collisions at sqrt(s) = 8 TeV. 2016.

[60] Frank Krauss, Ralf Kuhn, and Gerhard Soff. AMEGIC++ 1.0: A Matrix Element Generator In C++. *JHEP*, 02:044, 2002.

[61] Tanju Gleisberg and Stefan Höche. Comix, a new matrix element generator. *JHEP*, 12:039, 2008.

[62] C. F. Berger et al. Automated implementation of on-shell methods for one-loop amplitudes. *Phys.Rev.*, D78:036003, 2008.

[63] Gavin Cullen et al. G*OSAM*-2.0: a tool for automated one-loop calculations within the Standard Model and beyond. *Eur. Phys. J.*, C74(8):3001, 2014.

[64] Simon Badger, Benedikt Biedermann, Peter Uwer, and Valery Yundin. Numerical evaluation of virtual corrections to multi-jet production in massless QCD. 2012.

[65] Fabio Cascioli, Philipp Maierhöfer, and Stefano Pozzorini. Scattering Amplitudes with Open Loops. *Phys.Rev.Lett.*, 108:111601, 2012.

[66] T. Binoth et al. A proposal for a standard interface between Monte Carlo tools and one-loop programs. *Comput. Phys. Commun.*, 181:1612–1622, 2010.

[67] The OPENLOOPS one-loop generator by F. Cascioli, J. Lindert, P. Maierhöfer and S. Pozzorini is publicly available at http://openloops.hepforge.org.

[68] Ansgar Denner, Stefan Dittmaier, and Lars Hofer. Collier: a fortran-based Complex One-Loop LIbrary in Extended Regularizations. 2016.

[69] Ansgar Denner, Stefan Dittmaier, and Lars Hofer. COLLIER - A fortran-library for one-loop integrals. *PoS*, LL2014:071, 2014.

[70] Tanju Gleisberg and Frank Krauss. Automating dipole subtraction for QCD NLO calculations. *Eur. Phys. J.*, C53:501–523, 2008.

[71] Steffen Schumann and Frank Krauss. A parton shower algorithm based on Catani-Seymour dipole factorisation. *JHEP*, 03:038, 2008.

[72] Stefan Höche, Steffen Schumann, and Frank Siegert. Hard photon production and matrix-element parton-shower merging. *Phys. Rev.*, D81:034026, 2010.

[73] Zoltan Nagy and Davison E. Soper. A new parton shower algorithm: Shower evolution, matching at leading and next–to–leading order level.

[74] Stefano Frixione and Bryan R. Webber. Matching NLO QCD computations and parton shower simulations. *JHEP*, 06:029, 2002.

[75] Stefan Höche, Frank Krauss, Marek Schönherr, and Frank Siegert. A critical appraisal of NLO+PS matching methods. *JHEP*, 09:049, 2012.

[76] Stefan Höche, Frank Krauss, Marek Schönherr, and Frank Siegert. QCD matrix elements + parton showers: The NLO case. *JHEP*, 1304:027, 2013.

[77] Stefan Höche, Frank Krauss, Marek Schönherr, and Frank Siegert. Next-to-leading order matrix elements and truncated showers. 2010.

[78] Enrico Bothmann, Marek Schönherr, and Steffen Schumann. Reweighting QCD matrix-element and parton-shower calculations. *Eur. Phys. J.*, C76:590, 2016.

[79] Matteo Cacciari, Gavin P. Salam, and Gregory Soyez. The Anti-k(t) jet clustering algorithm. *JHEP*, 0804:063, 2008.

[80] Andy Buckley, Jonathan Butterworth, Leif Lönnblad, David Grellscheid, Hendrik Hoeth, James Monk, Holger Schulz, and Frank Siegert. Rivet user manual. *Comput. Phys. Commun.*, 184:2803–2819, 2013.

[81] Matteo Cacciari, Gavin P. Salam, and Gregory Soyez. FastJet user manual. *Eur.Phys.J.*, C72:1896, 2012.

[82] M. A. G. Aivazis, John C. Collins, Fredrick I. Olness, and Wu-Ki Tung. Leptoproduction of heavy quarks. II. A unified QCD formulation of charged and neutral current processes from fixed-target to collider energies. *Phys. Rev.*, D50:3102–3118, 1994.

[83] R.S. Thorne and R.G. Roberts. An Ordered analysis of heavy flavor production in deep inelastic scattering. *Phys.Rev.*, D57:6871–6898, 1998.

[84] R.S. Thorne and R.G. Roberts. A Practical procedure for evolving heavy flavor structure functions. *Phys.Lett.*, B421:303–311, 1998.

[85] T. Gleisberg, S. Höche, F. Krauss, M. Schönherr, S. Schumann, F Siegert, and J. Winter. Event generation with SHERPA 1.1. *JHEP*, 02:007, 2009.

[86] Valerio Bertone, Stefano Carrazza, and Juan Rojo. APFEL: A PDF Evolution Library with QED corrections. *Comput. Phys. Commun.*, 185:1647–1668, 2014.

[87] The bbHFONLL code by S. Forte, D. Napoletano and M. Ubiali is publicly available at http://bbhfonll.hepforge.org.

[88] M. Buza, Y. Matiounine, J. Smith, and W. L. van Neerven. Charm electroproduction viewed in the variable flavor number scheme versus fixed order perturbation theory. *Eur. Phys. J.*, C1:301–320, 1998.